UNIVERSITAT POLITÈCNICA DE CATALUNYA
BARCELONATECH
Escola d'Enginyeria de Barcelona Est

EEIGM

Final Master Project:

Materials engineering degree

3D-PRINTING OF 8Y-TZP SOLID OXIDE FUEL CELL ELECTROLYTES

Report and Annexes

Author: Paulo Claude

Director: Joan Josep Roa Rovira

Call for proposal: February 2019

Abstract

In this Master's thesis were printed electrolytes for Solid Oxide Fuel Cell (SOFC) in yttria stabilized zirconia by additive manufacturing robocasting method and then characterized from the microstructural and mechanical points of view. In order to enhanced the density of the material with this manufacturing process, it was necessary to determine the optimum composition of the paste, composed of 8Y-TZP powder and hydrogel, and the optimal printing temperature to manufacture the samples. The hydrogel used was made with 25 wt.% of pluronic F-127® and 75 wt.% of distilled water. The optimal composition found was of 67,5 wt.% of ceramic powder and 32,5 wt.% of hydrogel, allowing the obtention of a relative density value close to 100% for the printed material after the realization of a sintering process at a temperature of 1450°C. Diverse injection heads were tested regarding the particle and agglomerate sizes of the ceramic powder, also in order to maximize the density of the final parts. The injection nozzle which showed the best results was made of plastic (smoothflow tapered tip) and with an injection diameter of 580 µm. Once these parameters fixed, two different geometries were printed: cylindric and tubular. Then, two different printing patterns, rectilinear and concentric, were tested in order to obtain the best appearance for the printed samples. The rectilinear one was chosen for the cylindrical geometry while the concentric one was chosen for the tubular geometry. The shrinkage of the material during the sintering process was measured and estimated equal to 57 $\pm$ 1.4 % of volume reduction for the optimal composition chosen previously. Were characterized for both geometries, along with samples manufactured by Cold Isostatic Pressing (CIP) (reference), the microstructure (phases composition, external porosity, grain size) as well as the mechanical properties (hardness, fracture toughness, elastic modulus). In a first time, the samples manufactured with AM and CIP were analyzed along with the initial 8Y-TZP powder with X-Ray Diffraction (XRD) in order to see if the manufacturing process could affect the phase composition of the material, which is not the case. With a Field Emission Scanning Electron Microscope (FESEM) were measured the external porosities of the different samples and the grain sizes of the material after the realization of a thermal attack at 1200°C. It was found that the amount of porosity for the samples printed was clearly higher than the one found for samples manufactured with CIP. The average value of grain area found was 3.07 μm^2. Concerning the mechanical properties, Vickers indentation allowed the obtention of the average hardness values of 10.9 ± 0.7 GPa (HV10) and 10.9 ± 0.8 GPa (HV5) as well as average fracture toughness values of 2.37 ± 0.73 $MPa.m^{-0.5}$ (HV10) and 3.63 ± 1.03 $MPa.m^{-0.5}$ (HV5). On the other hand, the Berkovich nanoindentation realized allowed the obtention of a range of hardness value comprise between 15.7 and 17.0 GPa as well as a range of young modulus comprise between 252 and 276 GPa for the samples manufactured with the optimum composition of materials.

Resumen

En este Trabajo de Fin de Master (TFM) fueron imprimidos electrolitos para "Solid Oxide Fuel Cell" (SOFC) con circona estabilizada con itría por robocasting y fueron caracterizados de unos puntos de vista microestructural y mecánico. De manera a maximizar la densidad del material con el proceso de manufacturación elegido, fue necesario determinar la composición óptima de la pasta de cerámica, compuesta de polvo de 8Y-TZP con un hidrogel, así como la temperatura óptima para imprimir las muestras. La composición elegida para la fabricación del hidrogel fue: 25 wt.% de pluronic F-127® con 75 wt.% de agua destilada. La composición optima encontrada para la pasta de cerámica fue de 67.5 wt.% de polvo de cerámica con 32.5 wt.% de hidrogel, la cual permitió obtener una densidad relativa cerca de 100% para las muestras, una vez sinterizadas a una temperatura de 1450°C. Distintas boquillas de inyección fueron utilizadas tomando en cuenta los tamaños de partícula y de aglomerado del polvo, de manera a maximizar la densidad final. La boquilla de inyección que permitió obtener el mejor resultado está hecha de plástico ("smoothflow tapered tip") y tiene un diámetro de inyección igual a 580 µm. Una vez estos parámetros elegidos, dos geometrías fueron imprimidas: una con forma cilíndrica y otra tubular. Fueron también probados dos patrones de impresión, uno rectilíneo y otro concéntrico para obtener el mejor acabado posible. El patrón rectilíneo fue elegido para la geometría cilíndrica mientras que el concéntrico fue elegido para la geometría tubular. Las contracciones del material fueron medidas y estimadas iguales a 57 $\pm$ 1.4 % de reducción en volumen total durante el proceso de sinterización para la composición optima elegida. Las dos geometrías fueron caracterizadas así como muestras manufacturadas por "Cold Isostatic Pressing" (CIP) que servirán de referencias. En un primer tiempo, las muestras fueron analizadas así como el polvo de 8Y-TZP utilizado en este TFM, con difracción de rayos X (XRD) de manera a determinar si el proceso de manufacturación afecta o no la composición de fase del material. Los espectros obtenidos permiten ver que no es el caso. Con un "Field Emission Scanning Electron Microscope" (FESEM) fueron determinadas las cantidades de porosidad externas para los diferentes tipos de muestras así como el tamaño de grano del material después de efectuar un ataque térmico a 1200°C. Se pudo observar que la cantidad de porosidad externa de las muestras imprimidas eran claramente superiores a la de las muestras manufacturadas por CIP. Se pudo también calcular el tamaño medio de las áreas de los granos, lo cual es igual a 3.07 μm^2. Respecto a las propiedades mecánicas, la técnica de indentación Vickers permitió obtener valores medias de 10.9 ± 0.7 GPa (HV10) y 10.9 ± 0.8 GPa (HV5) para la dureza del material así como valores medias de resistencia a la fractura de 2.37 ± 0.73 $MPa.m^{-0.5}$ (HV10) y 3.63 ± 1.03 $MPa.m^{-0.5}$ (HV5). Por otro lado, se pudo obtener con Berkovich nano-indentación una gama de valores de dureza contenidas entre 15.7 y 17.0 GPa al mismo tiempo que una gama de valores de módulos elásticos contenidas entre 252 y 276 GPa.

Résumé

L'objectif de ce travail de fin de Master fut d'imprimer des électrolytes de « Solid Oxide Fuel Cell » (SOFC) en oxyde de zirconium stabilisé avec de l'oxyde d'yttrium par fabrication additive (robocasting) et de caractériser ces électrolytes du point de vue microstructurale et mécanique. De manière à maximiser la densité du matériel avec ce procédé de fabrication, il a été nécessaire de déterminer la composition optimale de la pâte céramique, fabriquée à partir de poudre d'8Y-TZP et d'hydrogel, ainsi que la température d'impression optimale pour concevoir les échantillons. L'hydrogel utilisé fut fabriqué avec 25 wt.% de pluronic F-127® mélangé dans 75 wt.% d'eau distillée. La composition optimale déterminée fut de 67.5 wt.% de poudre de céramique et de 32.5 wt.% d'hydrogel, permettant l'obtention d'une densité relative proche de 100% du matériel sintérisé à une température de 1450°C. Plusieurs têtes d'injection furent aussi testées de façon à maximiser la densité finale en prenant en compte la taille des particules et des agglomérats de la poudre de céramique. La tête d'injection permettant d'obtenir les meilleurs résultats possède un diamètre d'injection de 580 µm et est composée de plastique (« smoothless tapered tip »). Un fois ces paramètres choisis, deux types de géométrie furent imprimées : l'une cylindrique et l'autre tubulaire. Deux patrons d'impression furent aussi testés, rectilinéaire et concentrique, afin d'obtenir la meilleure finition possible. Pour cette raison, le patron rectilinéaire fut utilisé pour la géométrie cylindrique tandis que le patron concentrique fut choisi pour la géométrie tubulaire. Les contractions du matériel, pour la composition optimale choisie, furent mesurées et estimées égales à 57 $\pm$ 1.4 % de réduction totale lors de la sintérisation. Des pièces de dimensions égales à celle des électrolytes imprimés furent fabriquées avec la méthode de « Cold Isostatic Pressing » (CIP) afin de servir de référence lors des diverses caractérisations. Dans un premier temps, les échantillons et la poudre d'oxyde de zirconium initialement utilisée furent analysées par diffraction des rayons X (XRD) afin de déterminer si le procédé de fabrication pourrait affecter la composition en phases du matériau. Les spectres de diffractions obtenus ont permis de vérifier que ce n'est pas le cas. Avec un « Field Emission Scanning Electron Microscope" (FESEM) furent déterminées les quantités de porosité externe ainsi que la taille des grains d'oxyde de zirconium, après avoir effectué une attaque thermique à 1200°C sur le matériau. La quantité de porosité externe des pièces créées par fabrication additive fut déterminée comme clairement supérieure à celle des pièces manufacturées par CIP. La taille moyenne de l'aire des grains fut déterminée comme étant égales à 3.07 μm^2. Concernant les propriétés mécaniques, la technique d'indentation Vickers permit l'obtention de valeurs moyennes de dureté égales à 10.9 ± 0.7 GPa (HV10) et 10.9 ± 0.8 GPa (HV5) ainsi que les valeurs moyennes de résistance à la fracture de 2.37 ± 0.73 $MPa.m^{-0.5}$ (HV10) et 3.63 ± 1.03 $MPa.m^{-0.5}$ (HV5). A l'échelle nanométrique, grâce au test de nano-indentation de Berkovich, une gamme de valeur de dureté comprises entre 15.7 et 17.0 GPa ainsi qu'une gamme de modules d'Young compris entre 252 et 276 GPa purent être déterminées.

Acknowledgements

I would like to express my heartfelt thanks to my thesis supervisor Joan Josep Roa for his countless advices and his help during the entire project. I also thank him for the trust he showed me since the beginning for every aspects of this work.

In the same way, I would like to express my gratitude to the PhD students Joaquim Minguela, Daniela Tovar and Ludmila Hodasova for their disinterested predisposition to give their assistance in any aspect or difficulty faced during my work.

Finally, thanks to my familly and my friends for their support and faith in me.

Glossary of terms

AC: Alternating Current

AFM: Atomic Force Microscope

AM: Additive Manufacturing

APU: Auxiliary Power Unit

CAD: Computer-Aided Design

CHP: Combined Heat and Power

CIP: Cold Isostatic Pressing

CN: Coordination Number

CVD: Chemical Vapor Deposition

DC: Direct Current

DZC: Dispersed Zirconia Ceramic

EVD: Electrochemical Vapor Deposition

FDM: Fused Deposited Modeling

FESEM: Field Emission Scanning Electron Microscope

FFF: Fused Filament Fabrication

FIB: Focused Ion Beam

LED: Light-Emitting Diode

LSCM: Laser Scanning Confocal Microscopy

LTD: Low Temperature Degradation

PEM: Polymer Electrolyte Membrane

PEO: PolyEthylene Oxide

PPO: PolyPropylene Oxide

PSZ: Partially Stabilized Zirconia

RH: Relative Humidity

SD: Secure Digital

SEM: Scanning Electron Microscope

SEVNB: Single-Edge V-Notched Beam

SLA: Stereo Lithography Apparatus

SLS: Selective Laser Sintering

SOFC: Solid Oxide Fuel Cell

TZP: Tetragonal Zirconia Polycristals

UHTC: Ultra High Temperature Ceramic

***x*Y-TZP**: Tetragonal zirconia partial stabilized with x molar percent of yttria

YSZ: Yttria-Stabilized Zirconia

ZTA: Zirconia Toughened Aluminia

Contents

Motivation

Nowadays, our society inevitably relies on energy production and consumption, from domestic to industrial uses, including entertainment and transportation. The average annual electricity consumed by a Spain's inhabitant was 5 000 kWh in 2015 **[1]**, while the global oil production is 92.6 million barrels a day, where a barrel represents 159 liters of petrol and is worth around $115.92 in 2018 **[2] [3]**. Among major challenges like global warming or the destruction of ecosystems, the production of clean energy is paramount to deal with those current issues and power the planet in the near future. One of these solutions lies in the use of fuel cells, which is a device that produces electrical energy directly and continuously from the chemical energy of a fuel and an oxidant **[4]**. More precisely, the aim of this Master's thesis relays to develop the correct protocol to process electrolyte for Solid Oxide Fuel Cells (SOFC) by using the Additive Manufacturing (AM) technology to manufacture them. In order to give an overview of the work realized, the first part of this Master's thesis will focus on briefly presenting the state of the art of the different AM techniques and fuel cells operating modes, types and materials as well as at the end a brief introduction explaining the main material employed to develop one of the most important part of this device, zirconia and its phase stabilization with yttria. Then, the following part will cover more precisely the methods and materials used along this investigation work. In a third part, the different experimental tests used to characterize the manufactured products will be presented, and in a final part, the different results, discussion and the main conclusions obtained.

1. Introduction

In this first section, the major lines of the different concepts used during this investigation will be drawn. In a first place, the general concept of additive manufacturing (AM) along with different existing processes will be given as well as some of the most important current applications. Then, the second part will focus on the operating mode of fuel cells and the different types of existing fuel cells. Finally, in this section a brief description of the state of the art on AM technique employed to develop fuel cells devices will be covered.

1.1. Concept of additive manufacturing's technique

Additive manufacturing (AM) methods are relatively recent techniques of production which evolved quickly and diversified since their apparition in the 1980s. Those methods tend to use a wide range of materials, from polymer to ceramic, from metals to natural tissues, in order to create items and parts with complex geometries and reduce the loss of material as well as the overall cost of manufacturing. They all allow to obtain a final part from a virtual 3D-model made by CAD (Computer-Aided Design) software in order to export it as a .STL file, or by using a scanner in order to obtain an 3D-image from a physical object **[5]**. Said image will then be treated through a post-processor software, then used to define the different layers to be deposited and to create the final .GCODE read by the 3D-printing machine. Therefore, it is possible to obtain the desired part with AM technologies by creating successive material layers by layer until the final desired geometry is reached.

1.1.1. Different aspects of AM's techniques

What made the AM methods considered as a 21st century breakthrough is essentially the fact that they allow modifying the geometry of any printed part without altering the process, which is a huge advantage comparing to processes like injection molding or extrusion. It also gives the opportunity to anyone to share their CAD fabrication drawings with the rest of the world using the internet, especially since the price range of low-cost polymer 3D-printers starts at 200€ **[6]**.

The other main advantages of the AM techniques compared to the traditional processes can be summarized as follow **[7]**:

- As AM techniques allow parts to be manufactured layer by layer, material efficiency is increased. Moreover, leftover material can sometimes be reused with minimum processing.
- Auxiliary resources such as cutting tools or cooling systems are not required in addition to the main printing system. Nevertheless, post treatments may be needed for ceramic or metallic parts while a filament heater can be required to "melt" and print thermoplastic.

- The use of an AM process does not require to appeal to a machinist or any qualified technician in most cases. Thorough knowledge of the machine is not needed to print from a CAD model and a great amount of information can be found in open sources.
- Unlike other processes, empty geometries, such as cores or cavities can be manufactured, which is really useful in order to build molds or casting dies.
- It is possible to regulate the porosity of the part, or to create parts with complex inner patterns such as honeycomb structures in order to reduce the density of a piece while conserving the mechanical properties.
- It is easily feasible to create parts using different materials at the same time.
- AM techniques can be used to produce final parts as well as intermediate parts in order to be assembled after their printing.

On the other hand, AM technique are not fully competitive for now because of certain limitations and drawbacks, which can be summarized as follows:

- One of the first limitations is the panel of materials available, which is clearly restricted. If it can be easy to print thermoplastic materials because of their thermal behavior, it is much more difficult and costlier to print metals, whereas ceramics require mixing with other materials such as polymers and a post treatment of sintering, which can therefore cause weakening of the final properties.
- If AM processes allow a huge flexibility in the process, which can sometimes allow a gain of time when changes in the part's geometry are needed, its use in a continue process for a big scale production clearly does not compete with other processes such as casting or extrusion.
- The size limitations due to the printing time can also be a problem as well as imperfections that can be caused by inhomogeneity in the initial preparation **[8]**.
- Another challenge for AM techniques concerns the mechanical properties that are often lower to those obtain with traditional methods.
- It can also be noticed that layer by layer appearance of the printed part can turn out to be a problem of importance in certain applications such as toys or building where the pieces are visible **[7][9]**.

1.1.2. Different clasification of AM

Due to their low melting temperature, polymeric materials were the first ones to be printed, and a huge amount of progress has been made in their manufacturing through AM technologies. The first technique invented was the stereo-lithography (see **Fig.1.1**), which was developed in 1983 by Charles Hull **[10]**. It consists in the use of a photosensitive resin in liquid state which will be cured and solidified by means of UV-radiation. A mobile substrate is used to get the bath down and enable the creation of the successive layers until the part is completed. Afterward, various techniques have been

developed, such as directed energy deposition, ultrasonic AM or fused material deposing. Besides, the latter is the nowadays most employed methodology and includes techniques like fused deposited modeling (FDM) or fused filament fabrication (FFF) (see **Fig.1.2**). These techniques consist in the use of a polymeric filament which melts while passing through a heated head. The melted material is then extruded and deposited on a platform where it cools and solidifies **[11]**.

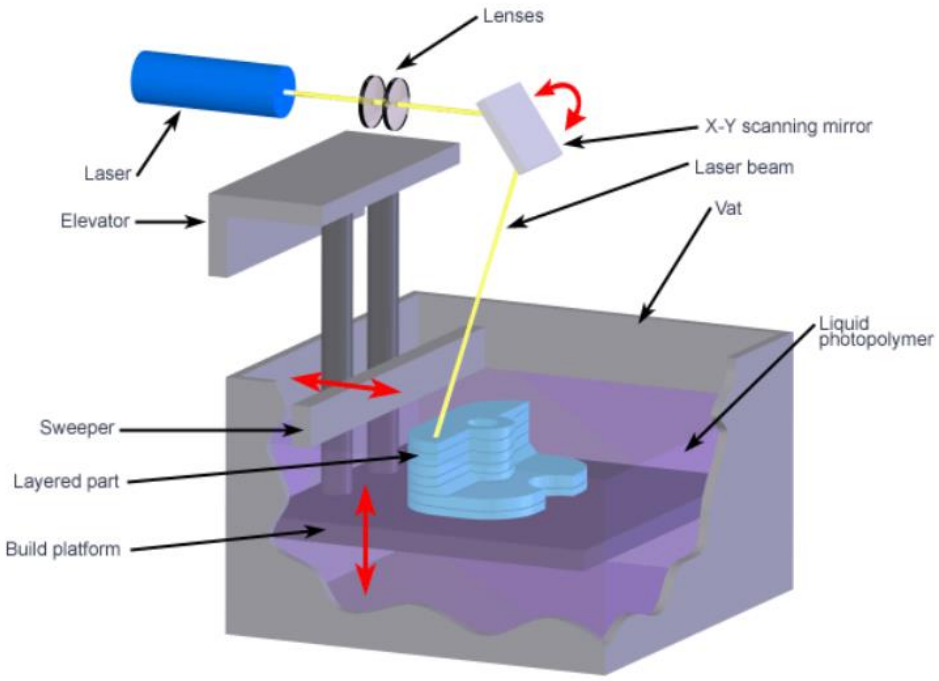

Fig.1.1 *Schematic representation of the stereolithography process* **[12]**.

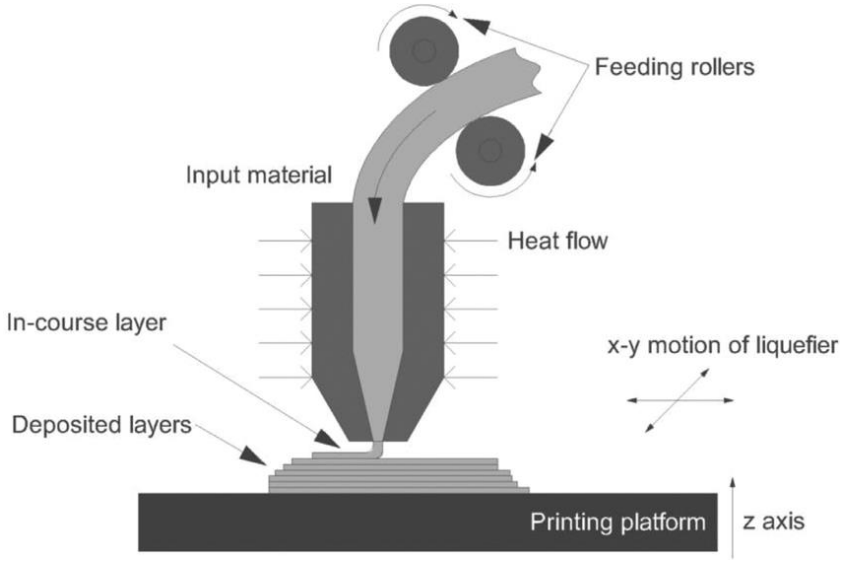

Fig.1.2 *Schematic representation of the Fused Filament Fabrication process* **[13]**.

Among the different existing techniques, focusing on the use of ceramic materials, various types of AM methods can be pointed out. Depending on the application or the part's final geometry and morphology, it can be useful to look into these different possibilities before starting production. From a general point of view, they can be classified in ***three main groups*** based on the nature of the fabrication process:

- **Negative additive manufacturing**

Those specific methods are based on the manufacturing of a sacrificial polymeric mold by means of AM in which the ceramic paste is then added and takes the space around the polymeric material. This first step is followed by a thermal treatment which will decompose the plastic core and sinter the ceramic piece **[14]**. Unique-use molds can then be created from polymer and used to obtain complex parts in ceramics, but also in metals or alloys.

- **Indirect additive manufacturing:**

These techniques allow to obtain directly the final ceramic part by creating it layer by layer. In order to do this, the ceramic material, which is usually present under the form of powder, is mixed with a vehicle or a binder in order to give to the pre-printed material a certain viscosity. The created piece will require a post-treatment to develop a dense structure. Different methods of indirect additive manufacturing can be classified as follow:

- Powder-based 3D-printing: This method consists in impregnating a binder, aqueous or polymeric, on each deposited layer of ceramics powder. Then follows the thermal treatment to obtain the ceramic piece. This specific method is used to obtain part with high residual porosities, such as scaffolds. It is also possible to obtain higher density by modifying chemically or physically the ceramic material before the sintering process.

- Powder-based Selective Laser Sintering (SLS): The only difference between this method and the latter is that the sintering process is realized with a CO_2 laser beam applied directly on the powder layer. It can be pointed out that in this case, the use of a binder is not always necessary, but preferable because the direct sintering of ceramic powder gives poorer mechanical properties. Like the powder-based 3D-printing, the parts obtained contain a high porosity (near to 30%). The main advantage of this technique is that it offers a greater precision, due to the fact that the printed material does not need a structural sustain, which results in optimized and durable structures. Moreover, leftover powder can be reemployed in the subsequent printing process. This methodology is widely used, for example, in the field of tissue engineering **[9]**.

- Stereo-lithography Apparatus (SLA): In this technique the ceramic part is printed via the use of a ceramic suspension on a liquid polymer resin. It also requires a light-curing treatment of the photo-polymeric matrix and a final thermal treatment to sinter the part. It is the built platform that moves in

the *z*-direction in order to lower the part for each printed layer and to allow the creation of the next one. The resulting density is then higher than with the other indirect additive manufacturing because it uses a higher concentration of ceramic material. Nevertheless, SLA can only produce parts of limited size and the price of the material used is often higher than other AM techniques that does not require photo-polymers. **[9]**.

- **Direct additive manufacturing**

This family of techniques includes all the processes that allow to obtain directly the final geometry from the printed ceramic with a single stage of sintering. They can be separated in two different groups:

- Direct inkjet printing: One of the main techniques for ceramics. It is based on the spray deposition of a liquid suspension with very high ceramic content (> 33 vol %). Additives are used in the suspensions to regulate parameters such as viscosity, surface tension and suspension power capacity. Moreover, the minimum droplet size allows a great control over the distribution of the composition of the piece, which can lead to the fabrication of multi-material structures. Currently, due to the limited mechanical properties obtained, this technique is more often used for 2D part than for 3D-geometries **[7]**.

It can be cited that a similar method exists and is called contour crafting. It is capable of extruding concrete paste or soil. This method has been prototyped to be used for future construction on the moon as it is presented in Ref. **[7]**.

- 3D-printing by filament extrusion or robocasting method: Robocasting techniques are based on the extrusion of a viscous ceramic paste through one or more heads. This ceramic paste is composed of the ceramic powder mixed with a suspension medium such as hydrogels. For this kind of AM technology, the control of the rheological parameters is a key point to prevent issues such as the deformation of the geometry before the application of the sintering process. In order to control those parameters, several methods are used:

i) Control of the flocculation,
ii) suspensions to obtain gels (modifying the pH or the solvent's ionic strength), and
iii) addition of gelling additives.

This method offers a high particle packing density which leads to greater mechanical properties for parts with the same geometry than other AM techniques. The versatility of this method makes it a broadly-used technique in various fields, like the domain of energy with the creation of parts for optic fibers or for SOFCs **[15]**.

1.1.3. Fields of application

As it has been made clear in the previous sections, the numerous positives aspects of AM technologies trigger interest in many different fields of application. Within this context, the most concerned range of application can be depicted as follows **[7, 9]**:

- **Automotive industry:** New technologies such as AM techniques represent a key asset for the automotive industry. The reduction of the production's cost and its cycle time while reducing the weight and conserving or improving the mechanical properties of the different components of a vehicle are the main goals of this industry. Structural and functional parts such as engine exhausts, drive shafts, gear boxes or breaking systems have been created, especially for luxury or racing vehicles, because they require light-weight materials to build complex structures while representing low production volumes.

- **Aerospace:** In the same spirit that the automotive industry, AM technologies represent a critical tool for building highly complex geometries with specific technique alloys and Ultra High Temperature Ceramics (UHTC). The low volume production and the huge investment allow those technologies in this field to manufacture complex parts such as fan blade edges, nozzles or functional electronics.

- **Biomedical:** Implants, scaffolds or stems can be easily manufactured with AM processes, especially since biocompatible materials can be easier to process than technical materials due to their lower mechanical properties.

- **Building**: In 2014, the first residential structures were manufactured with AM technologies and present a real potential, especially for astronauts, but also for third world countries. It now represents 3% of the AM market **[7]**. In this field, geopolymers are relevant material. They are often made of fly ash and slag collected from industrial wastes. The synthesis of this material consists in the reaction of aluminosilicate materials with alkaline reagents (sodium or potassium silicates), which make them green construction materials. One of the drawbacks of this kind of large-scale process is the necessity to realize a continuous, high temperature control of the material during the entire printing. Moreover, in order to print large pieces such as dome or arch, an additional structure can be required to sustain the printed material. **[16]**

- **Energy**: As it is used in this investigation to create fuel cells, AM technologies also permit to manufacture components for catalytic applications **[9]**.

Another important field of application for the AM technology that can be pointed out is the one for daily life, toys and arts **[17]**. Indeed, the low price for basic 3D-printer and the simplicity of CAD modeling and sharing imply huge possibilities of use for anybody. Therefore, it is also possible to buy models on the internet and especially in the deep web where big communities work together in order

to improve the modeling of part. On the other side, model of products such as handguns are also produced. For these reasons, new regulations and laws have been proposed in order to forbid the printing of weapons. The question of intellectual properties also has to be considered, because of the simplicity of copying and printing **[18, 19, 20]**.

1.2. Functioning and type of fuel cells

In order to apprehend and understand the importance of the use of ceramic in this Master's thesis, it can be useful to recall in this section what are the main components of a fuel cell and how they work together. A fuel cell consists of two electrodes; called anode and cathode, which are separated by an electrolyte. Once these components in place, a fuel is fed to the anode, which undergoes a reaction of oxidation which releases electrons to the external circuit. In the meantime, the oxidant undergoes a reduction reaction when entering in contact with the cathode by accepting electrons from the external circuit. The electrons flow from the anode to the cathode and produce direct-current electricity (see **Fig.1.3**).

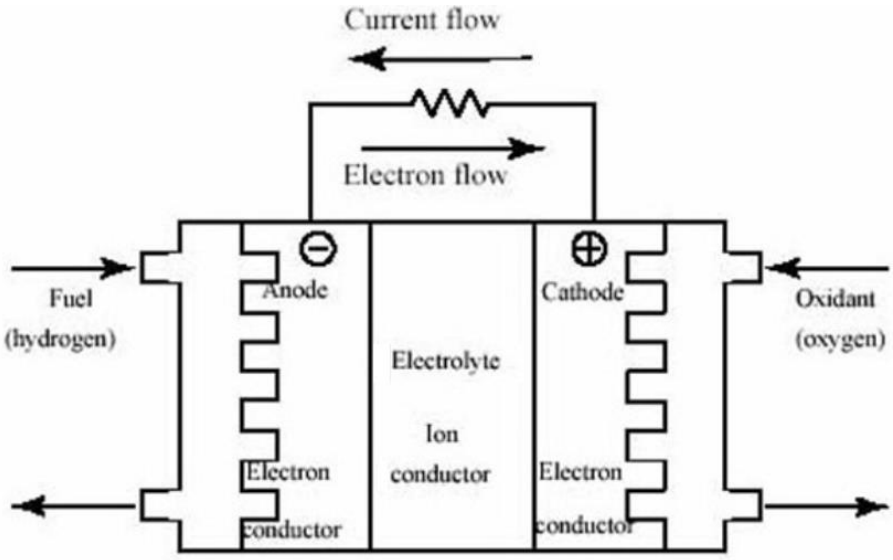

Fig.1.3 *Schematic representation of the internal functioning of a fuel cell* **[21]**.

1.2.1. Different functioning's types of fuel cells

The main characteristic used to classify fuel cells is the kind of electrolyte employed. Consequently, an important number of parameters are defined by this component, such as the electro-chemical reactions that take place in the cell, the temperature range of operation or the fuel required. These properties as well as the pros and cons of each type of fuel cells determine the application for

which they are most suitable. In **Table 1.1** are pointed out the main types of fuel cell among the different kind of cells that have been developed since the apparition of hydrogen fuel cells **[22]**:

Table 1.1. *Main types of fuel cells along with their properties* **[23]**.

Fuel cell type	Polymer electrolyte membrane, PEM	Alkaline	Phosphoric acid	Molten carbonate	Solid oxide
Electrolyte	Perfluorosulfonic acid	Aqueous potassium hydroxide soaked in a porous matrix, or alkaline polymer membrane	Phosphoric acid soaked in a porous matrix or imbibed in a polymer membrane	Molten lithium, sodium, and/or potassium carbonates, soaked in a porous matrix	Yttria stabilized zirconia
Operating temperature	< 120°C	< 100°C	150 - 200°C	600 - 700°C	500 - 1000°C
Applications	Backup power, Portable power, Transportation, Distributed energy	Military, Space, Backup power, Transportation	Distributed energy	Electrical utility, Distributed energy	Auxiliary power, Electrical utility, Distributed energy
Advantages	Solid electrolyte reduces corrosion and electrolyte management problems Low temperature Quick start-up and load following	Wider range of stable materials allows lower cost components Low temperature Quick start-up	Suitable for CHP Increased tolerance to fuel impurities	High efficiency Fuel flexibility Suitable for CHP Hybrid/gas turbine cycle	High efficiency Fuel flexibility Solid electrolyte Suitable for CHP Hybrid/gas Turbine cycle

Table 1.1. *Main types of fuel cells along with their properties* (continuation) **[23]**.

Drawbacks	Expensive catalysts Sensitive to fuel impurities	Sensitive to CO_2 in fuel and air Electrolyte management (aqueous) Electrolyte conductivity (polymer	Expensive catalysts Long start-up time Sulfur sensitivity	High temperature corrosion and breakdown of cell components Long start-up time Low power density	Corrosion and breakdown at High temperature Long start-up time Limited number of shutdowns

In this Master's thesis, will be manufactured SOFC electrolytes due to their various advantages comparing with the other types of fuel cell, and because the AM process chosen gives the ability to manufacture ceramic parts with rapidity and flexibility.

It can be observed that regarding the operating temperatures of the different fuel cells, SOFCs are the ones which can reach the higher temperature without suffering degradation.

From a general point of view, the different redox reactions occurring inside the fuel cell devices can be presented as follows:

Reduction reaction at the cathode-electrolyte interface $\frac{1}{2}O_2(g) + 2e^- \rightarrow O^{2-}$ **(eq.1.1)**

Oxidation reaction at the anode-electrolyte interface $\frac{1}{2}H_2(g) \rightarrow H^+ + e^-$ **(eq.1.2)**

Overall reaction in the cell $H_2(g) + \frac{1}{2}O_2(g) \rightarrow H_2O(l)$ **(eq.1.3)**

Considering the global reaction that takes place at the cathode-electrolyte interface **(eq.1.1)**, three possible reaction paths for the oxygen reduction can be considered depending on the type of SOFC. All three paths are depicted in **Fig.1.4**.

- **Electrode surface path:** In this reduction mode, the oxygen diffuses towards the cathode where it is adsorbed and diffuses to the interface electrode-electrolyte-gas phase, also known as three-phase boundary (3PB or TPB). Then, a complete ionization of the oxygen takes place, followed by the ionic transfer into the electrolyte.

- **Bulk path:** In this reaction path, the atom of oxygen also diffuses towards the cathode where it is adsorbed, but it is then directly dissociated and ionized by the cathode material (2PB). O^{2-} is then transported through the cathode to the electrolyte and is then transfer to this last part.
- **Electrolyte surface path:** In this last way, the oxygen gas diffuses directly towards the electrolyte where it is adsorbed (2PB), dissociated and ionized. However, due to the low electronic conductivity of most electrolytes used such as zirconia **[24]**, the active zone is restricted to a region close to the 3PB.

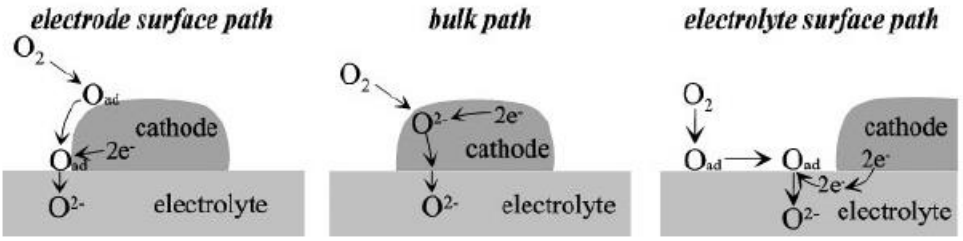

Fig.1.4 *Schematic representation of the three oxygen-reduction paths* **[24]**.

For metallic electrodes in SOFCs, the reaction of reduction generally occurs at the 3PB because these materials possess an electronic conductivity higher than their ionic conductivity **[25].**

1.2.2. Domains of fuel cells applications:

Concerning the applications made of fuel cells, they can be grouped in four main branches of application:

- **Transportation:** Fuel cells have already demonstrated their efficiency in this field in numerous ways. While the Maritime Hydrogen Fuel Cell project has shown the feasibility of replacing diesel generators by fuel cells for a coastal research vessel in 2015 **[26]**, Alstom presents the Coradia iLint (see **Fig.1.5**) in 2018, the first train powered by hydrogen fuel cells **[27]**. For other more specific vehicles such as forklifts, the use of fuel cells is a great alternative to traditional lead-acid batteries because they can be refueled quicker which allow an increase in production **[28]**.
- **Portable power:** This field covers military applications as well as Auxiliary Power Unit (APU) (see **Fig.1.5**) or small and large personal electronics such as mp3 players or laptops. Fuel cell are already available for these applications ranging from less than 5W (micro fuel cells) and up to 500KW **[29]**.
- **Stationary:** This group comprises all fuel cells units which are not designed to be moved. These can be primary power units, system of combined heat and power or uninterruptible systems.
- **Backup power:** These applications typically use hydrogen as fuel, and their goal is to provide power when the primary source is disrupted **[30]**.

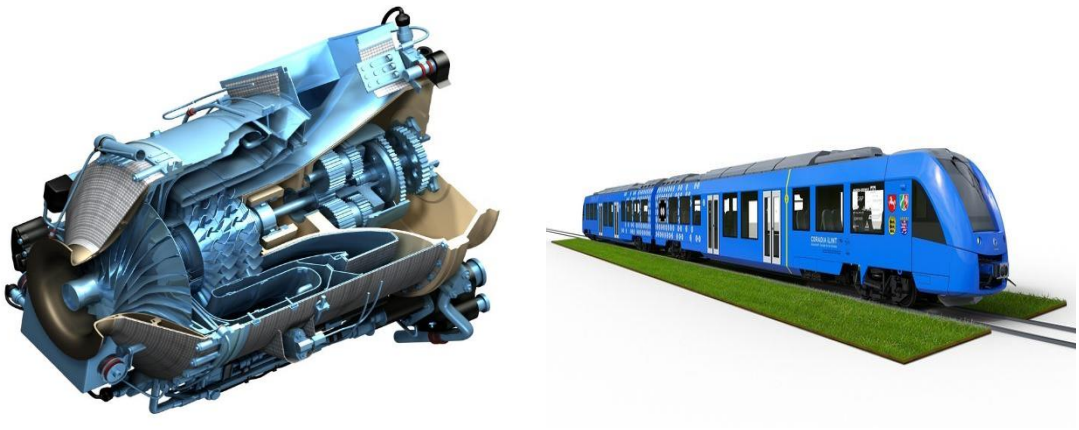

Fig.1.5 *Artistic representation of an APU (left hand side)* **[31]** *and of the Coradia iLint* **[32]**.

1.2.3. Requirements of the main components:

From a general point of view, the most fundamental requirements for fuel cells can be depicted as follows **[33]**:

- The adherence between the different pairs of components (electrolyte-anode and electrolyte-cathode) must be high enough under working conditions.
- The chemical interaction or inter-diffusion between adjoining components must not jeopardy the cell's integrity.
- The coefficient of dilatation must be similar between the different materials used in order to reduce the residual stresses generated during thermal shock.

More precisely, each part requires specific characteristics in order to give the fuel cell the highest conversion efficiency and productivity.

Electrolyte: This component conducts the ions from the anode to the cathode and must present a negligible electronic conductivity to avoid energy loss. It must also present stability in oxidant environments on a chemical, morphological and dimensional level to maximize the life-time of the cell. Also, the material used has to exhibit a high catalytic activity for the chemical and electrochemical reactions that take places inside the dispositive and displays numerous active reactions sites **[34].**

Moreover, it is required to be fully dense, with a relative density near 100%. Indeed, flaws, pinholes or other defects will reduce the performance of the cell by provoking leakage of the fuel/oxidant gases or by reducing the oxygen ion diffusion in the electrolyte **[35]**.

Cathode: This electrode requires a high electronic conductivity to allow the reduction reaction to happen on its surface. Therefore, it needs to be porous so as to enable the transport of electrons and gaseous reactants, and to present stability in oxidant environments from a chemical, morphological and dimensional point of view **[34]**.

Anode: In this electrode flows the fuel which undergoes an oxidation reaction on the anode's surface. That's why the material used to build this component requires a good stability in fuel environments, in addition to presenting a high electronic conductivity. Like for the other electrode, the material used must be porous **[34]**.

Interconnect or bipolar separator: This last part is used to connect the anode from one cell to the cathode from another and therefore ensures the proper functioning of the overall system. In order to last and undergo minimal degradation, the material used needs to present a good stability in both oxidant and fuel environments. In addition, it has to present a high ionic conductivity and to exhibit excellent electrical conductivity. Ideally, the ohmic loss due to the introduction of interconnects in the system should be negligible. Besides, the material used needs to present a low density **[36]**.

These four main components compose the fuel cells, but a single cell produces less than 1V. For this reason, fuel cells are combined in series into what is called a **stack** (see **Fig.1.6**). In order to ensure the functioning of this stack, other parts are required:

- A **fuel processor**, which converts the fuel into a usable form for the cell. In a system powered by a hydrogen fuel (methanol, diesel…), the processor is a reformer that converts hydrocarbons into a gas mixture containing hydrogen. For SOFCs, the high operating temperature ensures the reforming is happening by itself. This process is called internal reforming. Impurities created during the process of reforming need to be removed from the cell **[37]**.
- **Power conditioners**, which allow to control the electrical properties and to condition the current, especially since fuel cells produce electricity in direct current (DC) and that some equipment requires alternating current (AC) **[37]**.
- **Air compressors**, which ensures a high pressure of the reactant gases in order to increase the efficiency of the cell.
- **Humidifiers**, which especially used for Polymer Electrolyte Membrane (PEM) to avoid this last one to dry and to cause a malfunctioning of the cell.

Fig.1.6 *Photography of a fuel cell stack* **[38]**.

1.2.4. Solid Oxide Fuel Cell

Solid Oxide Fuel Cells (SOFCs) use a hard, non-porous metal oxide (in solid state) as electrolyte. It allows the fuel cells to present rapid kinetics reactions in a range of temperature between 500 and 1000°C which enhance the performance and remove the need for precious-metal catalyst, which reduces subsequently the associated production cost. Oxides also proved to be resistant to aggressive systems and oxidation. As an example, SOFCs can tolerate up to several orders of magnitude in sulfur concentration, which is more than every other kind of fuel cell **[22]**. However, high-temperature operations imply to take some precautions concerning the staff protection and the durability of the overall system while ensuring the stability of the temperature inside the cells.

The different SOFCs are electrically connected in series or parallel and are denominated by the term “stack”. The connection between the anode and cathode of different cells is ensured with components named interconnects.

As it has been seen above, each component of the fuel cell has specific requirements, which explain the necessity of different materials for each part. The main materials for each component are briefly described:

- **Electrolyte:**

Stabilized zirconia is one of the most known materials for electrolyte in SOFCs. Because of its high level of oxygen-ion conductivity and its stability in both oxidizing and reducing atmospheres, it is

a really interesting candidate for this role. In order to improve its mechanical properties, zirconia is stabilized with different oxides such as yttria Y_2O_3 which is the best-known and most used. Tetragonal polycrystalline zirconia (TZP) based materials is the main material used as an electrolyte, being the 3Y-TZP and 8Y-TZP the most common compositions, where 3 and 8 represent the molar percent of yttria in the composition. The effect and phenomenon linked to the stabilization of zirconia with yttria are detailed in the ***section 1.3.2***. as well as the microstructural properties of the zirconia in Ref. **[34]**.

Lanthanum gallate (LSGM) based electrolytes $(La,Sr)(Ga,Mg)O_3$ presents a higher ionic conductivity but exhibit a bad response in reducing environments due to the evaporation of gallium (Ga). The high cost of Ga represents a second problem for this material use **[34]**.

Pure cerium oxide, CeO_2, is the only stable oxide form and presents only one stable phase structure below its melting point, which is a cubic fluorite structure as it is depicted in **Fig.1.8 (a)**. For this reason, unlike ZrO_2 which possesses different structural states depending on temperature and pressure, CeO_2 does not require any stabilization doping agent in order to serve as electrolyte. Depending on the system's temperature and oxygen partial pressure (pO_2), the coefficient δ of the material - which true formula is $CeO_{2-\delta}$ - vary from 0 to 0.28. For this reason, the oxygen deficiency concentration changes and affects the ionic properties of the material. This non-stoichiometric form exhibits both ionic and electronic conduction, and it has been demonstrated that in order to obtain the most significant ionic conduction, CeO_2 needed to be exposed to working temperatures higher than 500°C **[39]**.

Other **Ce-based oxide ion conductor** such as Gd doped CeO_2 (GCO) can be used as a material for the SOFC electrode due to their high ionic conductivity, even though they can quickly cause internal short circuits of the cell by becoming mixing conductors in contact with the anode environment **[34]**.

Stabilized bismuthsesquioxide Bi_2O_3 material possesses five different crystallographic phases depending on the temperature and the cooling rate. For the studied application, are only relevant the defective fluorite-type crystal where two of the eight oxygen sites are vacant. This specific phase is called the δ-phase, which presents a face cubic centered structure as it is shown in **Fig.1.7 (b)** and is always stable for temperatures between 729°C and 824°C this last being the melting point of this oxide. This phase presents a high ionic conductivity as it is summarized in Ref. **[40]**.

In order to increase the range of the operating temperature, it is possible to stabilize the phase δ at lower temperature, the same way it was possible to stabilize the tetragonal (***t***) and cubic (***c***) phase of the zirconia. The dopants that can be used are metal oxide such as Fe_2O_3, Nb_2O_5 or Ta_2O_5 **[41]**.

Stabilized δ-phase Bi_2O_3 presents a high ionic conductivity, which allows it to be used as electrolyte in SOFCs at reduced temperature. However, this oxide is easily reduced under low

critical oxygen partial pressures, and can be decomposed into bismuth metal. This last characteristic implies the use of protection for the material from direct exposure to reducing atmospheres **[41]**.

More complex ceramic materials used as electrolyte for SOFCs are called **protonic conductors**. Those materials are considered as perovskite materials, of general formula ABO_3, which means that they possess the same crystallographic structure that calcium titanium oxide $CaTiO_3$ (see **Fig.1.8 (b)**) **[42]**. These conductors exhibit a protonic conduction in hydrogen or wet atmospheres at temperatures above 1000°C. When exposed to high temperatures, interactions between oxygen-ion vacancies and oxygen atom produce electron holes, which represent the lack of an electron at a position where one could exist. Since in a normal atom or crystal lattice, the negative charge is balanced by a positive one, the absence of an electron leaves a net positive charge at the hole's position **[43]**. The type of protons produced can be interstitial or vacancies depending on the production's place. It is possible to classify the protonic conductors into two subgroups:

- **Doped $BaCeO_3$:** Material with high proton conduction at high temperature, it can also present a protonic conduction due to the fact that the compound absorbs water vapor from the atmosphere during its preparation and acquires a concentration of mobile protons.
- **Doped $SrCeO_3$:** Also a protonic conductor, this doped material shows a high efficiency in hydrogen atmosphere. Its protonic conductivity increases with its content of oxygen-ion vacancies while it is not dependent on the dopant concentration.

- **Cathode:**

The main materials used to manufacture cathodes in SOFCs are:

Lanthanum manganite $LaMnO_3$: One of the main materials used to build cathodes for SOFCs, for it presents a high electrical conductivity in oxidizing atmospheres along with an adequate compatibility with yttrium stabilized zirconia (YSZ) electrolyte. Moreover, its thermal expansion is close enough to the other cell components'. This material belongs to the perovskite oxides. This material presents an orthorhombic structure **Fig.1.7 (c)** at room temperature and exhibit a phase transformation at 600°C from orthorhombic to rhombohedral **Fig.1.7 (a)**. This transformation is due to the oxidation of some of the Mn^{3+} to Mn^{4+} ions. Depending on the preparation conditions, this material can show an excess, a deficiency or a perfect stoichiometry of oxygen ions which affect the ionic and electronic conductivity. In order to be efficient as a cathode and allow the reaction to take place, the perovskite material needs to present an oxygen deficiency.

Lanthanum cobaltite $LaCoO_3$: Also a perovskite material, it possesses a rhombohedral structure from room temperature to 1000°C (this transition temperature can vary according to the dopant addition) and then undergoes a phase transition to a cubic phase. This material shows a large

oxygen deficiency at temperature superior to 1000°C, especially when doped with a lower valence cation such as strontium (valence of 2 against 3 for lanthanum) **[44]**.

Doped oxides can be used even though they present a thermal expansion coefficient that does not match with YSZ's, and also present a lack of conductivity.

- Indium oxide In_2O_3, which presents a high electrical conductivity and can be deposited by chemical vapor deposition (CVD), enabling the production of thin film. The drawbacks of this limitation are its elevated cost as well as its thermodynamic instability.
- $LaFeO_3$ – $LaCoO_3$ based materials, which possesses mixed conducting properties.
- Strontium doped $PrMnO_3$, which present a good efficiency for reduced temperature application
- RuO_2/YSZ materials

- **Anode:**

The main materials used as anode electrode are:

Nickel/Yttria stabilized zirconia cermet: The advantage of NiSZ, almost exclusively used as SOFC's anode, is the low price of the metal compared to others such as palladium or platinum. As it has been explained in the previous part, anodes need to contain porosity in order to ensure their role. To maintain the required porous structure of the nickel during long periods of time and at high temperatures, YSZ is incorporated. It helps maintaining and supporting the nickel-metal particles, inhibiting their coarsening with the temperature (melting point of nickel is 1453°C), but also regulating the expansion coefficient in order to make it closer to those of the other cell components.

Cobalt/calcium doped with zirconia: Cobalt is widely used for this application, although it has a higher cost than Nickel. It presents a high tolerance to sulfur exposition along with a great oxidation potential. Therefore, it requires less complete fuel combustion to achieve great efficiency.

Ruthenium/YSZ cermet: The high melting point of ruthenium (2310°C) gives the material a good resistance to particle coarsening. Moreover, ruthenium-based supported catalysts show a high effectiveness for partial oxidation of CH_4 (synthesis gas used in some case). The major drawback of this material is its transformation at high temperature (above 800°C) in presence of oxygen into volatile oxides **[45]**.

Mixed conducting oxides: By mixing different conductor oxides in which both oxygen ions and electrons are mobile, electrochemical reactions occur over the entire interfacial area. An example of this kind is ZrO_2 – Y_2O_3 – TiO_2 solid solutions which present a real interest for SOFCs because of their compatibility with the YSZ electrolyte. Up to 15 mol% of TiO_2 can be dissolved in ZrO_2 stabilized with 12 mol% of Y_2O_3 to form a mixed conducting fluorite structure phase.

- **Interconnect:**

Metallic materials are considered to replace ceramics as interconnects in SOFCs, because their electrical conductivity is often several orders of magnitude larger and their ohmic loss is negligible. Moreover, the electrical conductivity of metal interconnect is independent from the oxygen partial pressure unlike ceramic interconnects. The main problem of their use resides in the fact that metallic materials inevitably produce oxides under oxidizing environment. Then, in order to be used as interconnect, the metal must display a really slow oxide's growth considering the service lifetime of the cell. In addition, the formed oxide scale must exhibit sufficiently high electronic conductivity to avoid excessive ohmic losses. It also has to be stable, dense and strongly adhere to the metal on the interface. Among them, have been investigated:

- **Chromium based alloys**, which present a thermal expansion behavior close to the ceramics' used in fuel cells and a relatively good oxidation and corrosion resistance provided by the formation of Cr_2O_3. This oxide presents a large electronic conductivity, but also a rapid formation which ends by forming volatile species. This last point constitutes the main drawback of this material for an application as interconnect.
- **Iron based alloys** are easier to manufacture than the chromium-based ones and therefore present a lower cost. Some of them are investigated such as Fe-Cr-Mn and Fe-Cr-W, but still present the problem of chromium volatilization explained for the previous alloys.
- **Nickel based alloys** present resistance to higher temperature than the previous two. They consist in alloying nickel with metals such as chromium, iron or manganese and present lower oxidation kinetics. Nickel base superalloys are investigated for this application due to its low coefficient of thermal expansion **[46]**.

Concerning ceramic materials, **Lanthanum chromite ($LaCrO_3$)** is nowadays the most common candidate due to its high electronic conductivity in both fuel and oxidant conditions. It also exhibits a good compatibility in terms of phase, microstructure and thermal expansion with the other components of the cell. In order to improve the electrical conductivity, lanthanum chromite can be doped with lanthanum or chromium. Its efficiency will be higher in oxidizing environment that in reducing one due to the difference in pO_2 **[36]**.

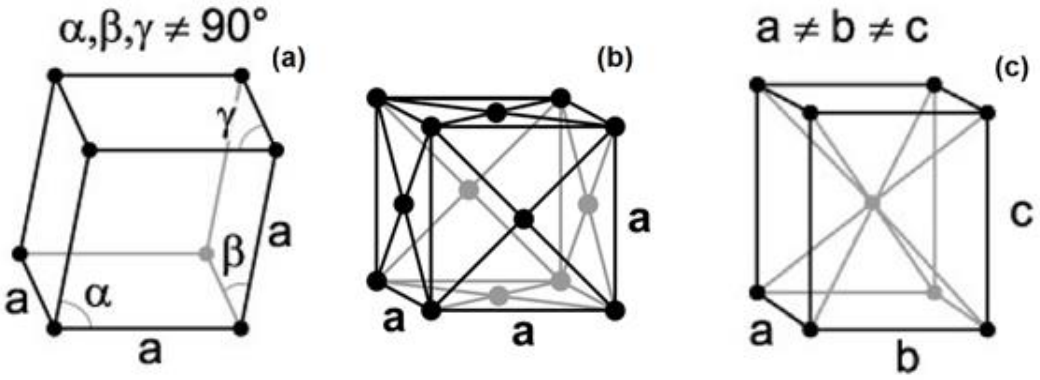

Fig.1.7 *Schematic representation of the **(a)** rhombohedral, **(b)** faces centered cubic and **(c)** orthorhombic lattices* **[47, 48]**.

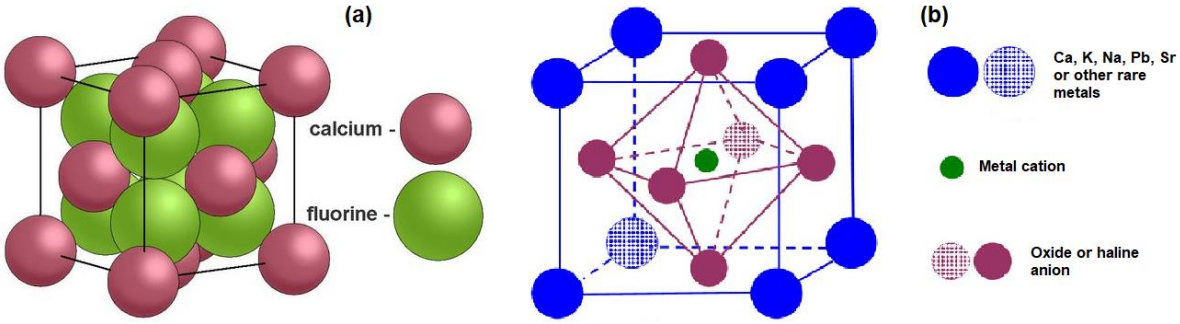

Fig.1.8 *Schematics representation of the **(a)** Cubic fluorite and **(b)** Perovskite structures* **[49, 50]**.

Beside the type of material used for the SOFC's fabrication, the following aspects need to be taken into consideration:

- **Geometry of the electrolyte:** It can be of different natures, relying on the application and the specific stack design **[51]**. The main geometry used can be planar, tubular, flat-plane, banded or corrugated. Each specific geometry has its own contact area and therefore, its own efficiency and adherence between the different parts.
- **Configuration in SOFC single cell**: Beside the geometry, there is two different broad ways to ensure the support of the cell. A fuel cell can either be considered as self-supporting or relying on external supporting. In the first case, one of the components (electrolyte, cathode or anode) acts as the cell structural support, which will generally be thicker than the other parts. In the other configuration, the interconnect or another porous substrate will ensure the structural properties of the SOFC.
- **Current in the stack:** This parameter depends on the design of the cells and stack.

1.2.5. Production of SOFCs

From a general point of view, the various existing processes used to manufacture the different components can be regrouped in two main categories. The first one is the particulate approach and consists in consolidating different ceramic powders into cell components and then applied a sintering treatment to the overall fuel cell. One example of this category of process is the tape calendaring and can be resumed with the **Fig.1.9 (a)**. It consists in subsequently extrudate the material, calendaring it between to rotative cylinders in order to form fine tape of material, and finally pressing different tapes of different materials to obtain the final multilayer product.

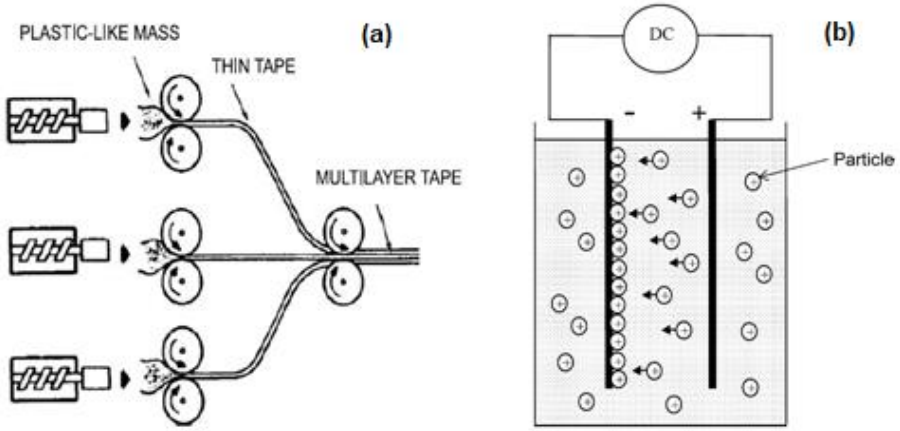

Fig.1.9 *Schematic representations of the **(a)** tape calendaring process and **(b)** electrophoretic deposition process* **[52]**.

The second category consists in depositing the cell component on a substrate by a chemical or physical way. The process of electrophoretic deposition is shown in the **Fig.1.9 (b)**. Other deposition methods such as EVD, plasma spraying and spin coating can be cited **[52]**.

1.3. Zirconium oxide

Zirconia, or zirconium oxide, which chemical formula is ZrO_2 is a material classified as an advanced ceramic as it is composed of metallic (Zr) and non-metallic (O) elements bonded by ionic and covalent bonding. ZrO_2 was discovered in 1789 by the German scientist Martin Heinrich Klaproth. The main methods used nowadays to obtain the material are refining processes of sands and gravels containing zircon ($ZrO_2 \cdot SiO_2$, the most common mineral from which zirconia can be extracted) and baddeleyite (ZrO_2 with impurities). Depending on the application, zirconia is often combined with other oxides in order to modify and enhance its properties. It represents a huge asset from an engineering

perspective because this ceramic combines high hardness, fracture toughness, chemical stability and mechanical resistance among others.

1.3.1. Microstructures and phase transformations mechanisms of zirconia

ZrO_2 materials present three different crystalline structures depending on the temperature below its melting point which is 2715 °C. Those different crystallographic structures characterize a property known as polymorphism. From the higher point with solid state to room temperature, the first structure appearing is a fluorite type, with a cubic phase (*c*) which is present at high temperature, between 2715°C and 2377°C. It then undergoes a phase transformation to a BCC tetragonal phase (*t*), with a body cubic centered structure, thermodynamically stable at intermediate temperature, between 2377 and 1170°C. Then, for lower temperature, the stable phase is a monoclinic phase (*m*). This phenomenon occurring during the cooling process of zirconia as it is illustrated in **Fig.1.10**.

Monoclinic: This phase is the natural one of zirconia, also known as baddeleyite. This structure can contain approximately 2% of HfO_2 which is very similar to zirconia from a structural and chemical point of view. Zr^{4+} ions have a coordination number (CN) of seven and the oxygen ions occupy tetrahedral interstices. For this reason, the average distance Zr^{4+} - O^{2-} of three oxygen ions on seven is equal to 2.07 Å, while the other will possess an average distance of 2.21 Å. This implied that, in the structure, one of the (134.3°) angles will differ significantly from the original tetrahedral value (109.5°C). Therefore, the oxygen ion will not possess a planar structure, a curve will occur in the plane of the four oxygen ions while the plane for the three others will be completely erratic **[53].**

Tetragonal: Zr^{4+} ions possess a CN of eight, which causes the shape to appear unequal and distorted. Indeed, four of the oxygen ions will form a tetrahedron plan with a distance of 2.065 Å from the zircon ion, while the four others will be at a distance of 2.455 Å and form an elongated and rotated at 90° second tetrahedron **[53].**

Cubic: Zr^{4+} ions also have a CN of eight, therefore the crystallographic structure can be represented by a simple cubic lattice with eight oxygen ions located in the tetrahedral interstices surrounded by another cubic arrangement (CFC) of cations. This structure is also known as fluorite structure **[53].**

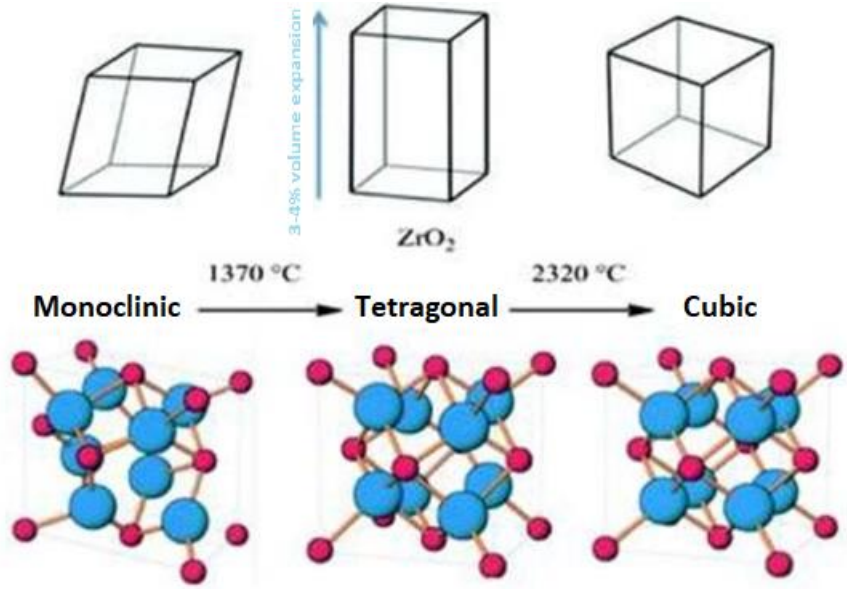

Fig.1.10 *Zirconia phases transformations* **[54]**.

The most problematic effect of this material is due to the contraction that undergoes the material during the phase transformation, mainly from the tetragonal to monoclinic phase (this transformation also known as martensitic transformation), which occur by shear without diffusion, i.e. the atomic position changing abruptly at a speed close to the speed of sound propagation in the solid **[53]**) of the *t*- to the *m*-phase will happen between 850 and 1000°C (depending on the cooling process) causing a large shear strain as well as volume expansion within a range of 3 to 4% inducing high internal stresses, embrittlement and cracking. For these reasons, if the sintering temperature used exceeds those of phase transformation, the sample can become more brittle and has reduced mechanical properties. To avoid this problematic, one alternative is to use a sintering treatment below 1200°C to avoid any of this phase transitions, but the properties of the final material will be affected and will present low strength and toughness. The second option is to alloy zirconia with an oxide such as calcium, cerium, yttrium or magnesium oxides, in order to retain and stabilize the *t*- and *c*-phase at room temperature. In this way, the nucleation and propagation of cracks will be reduced during the application of the thermal treatment. In order to compare the three zirconia phases, the value of some of their mechanical properties can be seen in **Table.1.2**.

Table.1.2 *Theorical properties of the three phases of zirconia* **[55, 56]**.

Phase	Monoclinic	Tetragonal	Cubic
Density (g.cm^{-3})	5.83	6.10	6.09
Elastic modulus (GPa)	215.1-235.9	78.6-245.5	276.5-302.3
Hardness (GPa)	9.2	/	/

1.3.2. Stabilization effects on zirconia

Depending on the type of stabilization, three different families of stabilized zirconia can be depicted as follow:

- **Dispersed Zirconia Ceramics (DZC):** A composite material formed by a dispersion of tetragonal zirconia in a proportion ranging from 5 to 30% in a ceramic matrix. The most used is zirconia toughened alumina or ZTA.
- **Fully Stabilized Zirconia (FSZ):** Through the use of a high quantity of stabilizers such as magnesia (16 mol%), calcium oxide (16 mol%) or yttria (8-10 mol%), along with a sintering treatment at high temperatures (1600°C), it is possible to obtain a material with *c*-phase matrix in which precipitate tetragonal or monoclinic particles **[53]**.
- **Partially Stabilized Zirconia (PSZ) or Tetragonal Zirconia Polycrystals (TZP):** To obtain this material, 2 to 3 mol% of yttria are often used in order to stabilize the *t*-phase which is present under the form of "monolith". A multiphase structure is then created, which usually contains a majority of *t*- and *c*-phases with *m*-phase precipitated in small amounts. Regarding the mechanical properties of TZP, it presents lower fracture toughness than FSZ, but a higher mechanical resistance **[53]**.

Therefore, the *t*- and *c*-phase are maintained in a metastable state at room temperature, and various parameters influence their stability besides the temperature. They can be resumed as follow:

- **Grain/particle size:** This parameter is relevant because the transition from *t*- to *m*-phase occurs in the grain boundaries. Indeed, below a critical value of particle size, the surface energy in the interface is no longer able to withstand the energy associated with the volume change of the grain during the phase transition. For compositions ranging from 2-3% mol of yttria, said value is 0.2 µm, and below this size, the transformation to *m*-phase cannot occur as reported in Ref. **[53]**.
- **Oxide/dopant content and distribution:** By increasing the quantity of dopant, the stability of the *t*- and *c*-phase will increase. Therefore, heterogeneity in the dispersion of dopant will lead to zones with higher concentration of *m*-phase.

- **Porosity and humidity:** Because the *m*-phase nucleation is enhanced by water, superficial porosity will increase the surface area of contact with it, especially on surface area, and reduce the stability of the *t*-phase.
- **Residual stresses:** While compressive stresses will stabilize the *t*-phase by preventing swelling, shear and tensile stresses will promote transformation towards the *m*-phase.

Stabilized *t*- zirconia can undergo two possible mechanisms which would trigger the t- to m-phase transformation. The first of these two mechanisms presents a positive aspect and is also known as phase transformation toughening. It can occur for example during a phenomenon of crack propagation in the material, as seen in **Fig.1.11**. Thus, the energy liberated will be sufficient to start the phase transition and generate an increase of 3-4% of the material's volume in this specific zone, leading to compressive tensions that will stop and prevent further propagation of the crack. This mechanism is responsible for the high facture toughness associated with metastable *t*- zirconia.

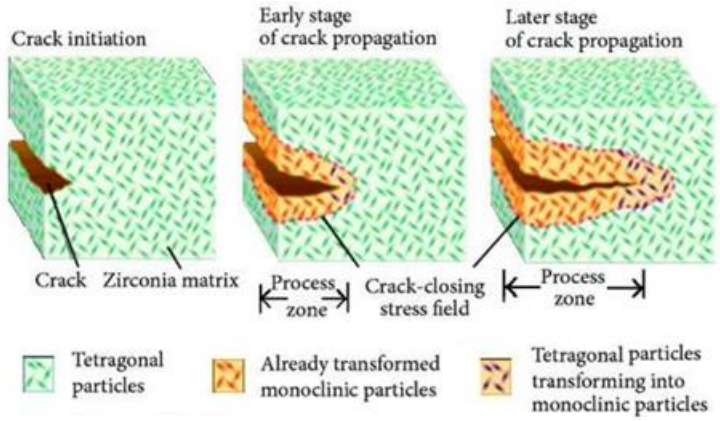

Fig.1.11 *Zirconia transformation toughening mechanisms* **[54]**.

The second mechanism has a negative impact on the material and its properties. Indeed, the low temperature degradation or hydrothermal degradation (LTD) is the mechanism responsible for most failures and breaking after a lifetime of 1 to 2 years of service in a component with *t*- zirconia. This phenomenon occurs for low temperatures within a range of 65 to 500°C and is affected by the humidity of the environment, which enhances the mechanism even for lower temperatures. Metastable *t*-phase then slowly transforms to m-phase due to its thermodynamic instability. The effect will first happen on the surface of the material which is exposed to the exterior and will then propagate inside the material, leading to micro cracking and roughening **[53]** as shown in **Fig.1.12**.

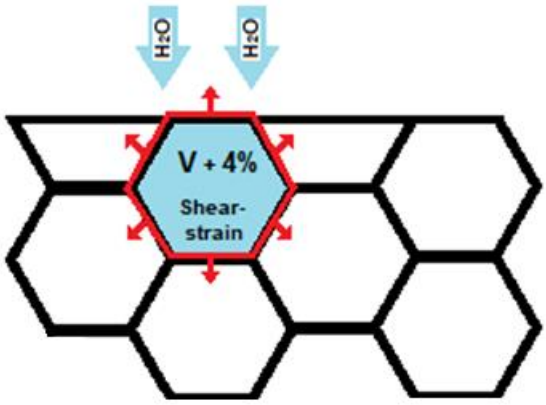

Fig.1.12 *Schematic representation of Ageing in zirconia* **[53]**.

In order to understand how the stabilization mechanism works, it is necessary to look at both involved materials from an atomistic point of view. In a range of temperatures adequate for the monoclinic structure to be the predominantly stable phase, in other words below 1200°C, the CN of Zr^{4+} is 7, meaning that this phase will be favored by the covalent nature of Zr-O bonds. For the other phases, *t*- and *c*-, Zr^{4+} will present a CN of 8, which explains their stabilities for higher temperatures where the oxygen vacancies concentration is increased. By doping ZrO_2 with Y_2O_3, Zr^{4+}will be substituted by Y^{3+}, which is a trivalent cation and presents a bigger radius than Zr^{4+}, resulting in the structure presented in **Fig.1.13** This way, oxygen vacancies are introduced and can stabilize the *t*-phase, and for higher oxygen vacancies concentration, the *c*-phase as well.

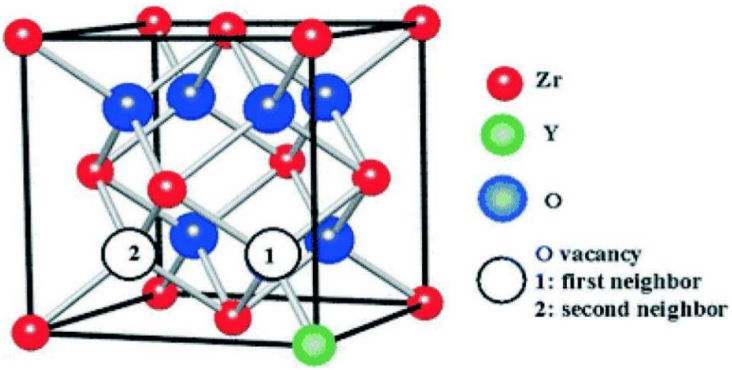

Fig.1.13 *Lattice of zirconia stabilized with yttria (c-phase)* **[54]**.

1.3.3. Applications of zirconia

As explained in the previous section, due to its polymorphism and more precisely its martensitic transformation from *t*- to *m*- phase, the manufacturing of components of pure zirconia is not possible due to spontaneous failures. As a consequence, it is necessary to use additional oxides in order to stabilize the *t*-phase form at room temperature **[53]**.

One of the most interesting properties of zirconia is its biocompatibility in both hard and soft tissues, but also not being cytotoxic and not promoting bacterial adhesion. Moreover, it presents a good chemical and dimensional stability as well as good mechanical properties, such as wear resistance, strength and Young modulus. For this reason, zirconia is an ideal option for biomedical applications, and is notably used to produce dental frameworks for dental substructures such as crowns or bridges, shown in **Fig.1.14 [53]**.

Other fields of application make common use of zirconia, by producing tools such as cutting blades such as the ones presented in **Fig.1.14**, radio frequency heating subsectors and metrology components. The automotive industry also uses it in order to produce valves and impellors, pump seals or gears for luxury vehicles or race cars **[57]**.

Fig.1.14 *Photography of crowns (left hand side) and cutting blades (right hand side) made of zirconia* **[58, 59]**.

2. State of the art

In this Master's thesis, the main covered subjects are the SOFCs, the AM of ceramic parts, the various aspects of zirconia and the mechanical characterization of the ceramic material. Among these different materials, those which should be used for and with the electrolyte produced in this Master's thesis are exhibited in **Table 2.1**.

Table 2.1. *Lists of material selected for the different parts of the fuel cells.*

Roles	*Electrolyte*	*Cathode*	*Anode*
Material	Stabilized zirconia with yttria $8Y - ZrO_2$ (YSZ)	Lanthanum gallate strontium and magnesium doped (LSM) La0.8Sr0.2Ga0.8Mg0.2O3	Nickel oxide NiO

Since the creation of SOFCs with robocasting method is a relatively new field of investigation, only a few articles are available on the subject. Nevertheless, investigations concerning the different aspects of the current study taken separately can be found more easily. Among the ones concerning the manufacture of **SOFCs** and their different functioning ways, can be cited and found in the literature the following articles:

Ellen Ivers-Tiffée, André Weber, Dirk Herbstritt (2001). ***Materials and technologies for SOFC-components.*** **Journal of the European Society, 21, pp.1805-1811.**

On this article are detailed the functioning of SOFCs as well as the main materials used for each part of the entire fuel cell. The different areas of application, material requirements and operating temperatures are detailed for the various types of SOFCs. The YSZ and TZP are cited as possible candidates to be used as electrolytes since they present many advantages compared to the other possible materials, such as an excellent mechanical stability and stability in oxidizing and reducing environment.

Minh, N. (2004). ***Solid oxide fuel cell technology-features and applications.*** **Solid State Ionics, 174(1-4), pp.271-277.**

This second article highlights the different technology features related to the building of SOFCs, such as the cell configuration, the stack design and the cell manufacturing process. Furthermore, are

explained the different features related to the high-temperature operations and finally, the diverse applications of SOFCs in the last part. Nevertheless, it can be noted that AM techniques are not mentioned as a production way for SOFC electrolyte, probably due to the relatively recent use of these techniques in this topic.

Fleig, J. (2003). ***Solid Oxide Fuel Cell Cathodes: Polarization Mechanisms and Modeling of the Electrochemical Performance.*** **Annual Review of Materials Research, 33(1), pp.361-382.**

This paper gives an overview of the electrochemical performance of the SOFCs cathodes by analyzing the various existing polarization mechanisms and modeling. The main goal of this article is to evaluate the relationships between the diverse parameters and the cathodic polarization resistance, which is a relevant factor of the fuel cell efficiency. In this study were investigated LSM cathodes. It is shown that it exists a correlation between external parameters, materials properties and geometrical factors with the polarization resistance.

Concerning the **AM techniques**, the following article gives an overview of the currently existing methods as well as the different printable materials and their applications. Are also explained the main challenges for 3D-printing for the next decades.

Ngo, T., Kashani, A., Imbalzano, G., Nguyen, K. and Hui, D. (2018). ***Additive manufacturing (3D-printing): A review of materials, methods, applications and challenges.*** **Composites Part B: Engineering, 143, pp.172-196.**

Studies on **zirconia** are numerous, concerning both its properties and its use in SOFCs. The next ones can be seen as examples to illustrate this field of science.

Din, S. and Kaleem, A. (1998). ***Vickers hardness study of zirconia partially stabilized with lanthanide group oxides.*** **Materials Chemistry and Physics, 53(1), pp.48-54.**

This article deals with the study of the Vickers hardness in zirconia partially stabilized with lanthanide group oxides, thus different oxides than yttria. Value for different compositions are exposed with their quantity in monoclinic, tetragonal and cubic phase of the sintered materials. The monoclinic phase of ZrO_2 (without oxide), the Vickers hardness is around 6.1GPa, while the maximum hardness obtain is of 8.76 for ZrO_2 stabilized with 12.5 mol% of CeO_2 which is composed of 98% of tetragonal phase. It can be noted that the tetragonal and cubic phases possess a higher hardness than the monoclinic one. X-rays diffraction of the different manufactured materials are used to obtain the percentage of the three phases.

Chevalier, J., Gremillard, L., Virkar, A. and Clarke, D. (2009). ***The Tetragonal-Monoclinic Transformation in Zirconia: Lessons Learned and Future Trends.*** **Journal of the American Ceramic Society, 92(9), pp.1901-1920.**

This article offers a focus on the tetragonal-monoclinic phase transformation of zirconia as well as on the influence of yttria in stabilizing the tetragonal phase. Even though the material used in this investigation is zirconia stabilized with 3mol% of yttria, the binary diagram of zirconia with yttria with a mole fraction between 0 and 0.2 can be found. Are also explained various mechanisms such as transformation toughening as well as the crystallographic features of the martensitic transformation of zirconia.

Kelly, J. and Denry, I. (2008). ***Stabilized zirconia as a structural ceramic: An overview.*** **Dental Materials, 24(3), pp.289-298.**

In this article are explained the different zirconia ceramics used in engineering depending on the stabilization process and the content of metastable phase. Dispersion-toughened ceramics consist of a dispersion of zirconia particles in another matrix such as alumina or mullite. Partially stabilized zirconia uses oxides as dopants to stabilize *t*- or *c*-phases, depending on the dopant content. Finally, single-phase polycrystalline *t*- ZrO_2 are obtained with fine grains of zirconia mixed with low quantities of dopant. Are also studied for 3Y-TZP the evolution of strength versus toughness as well as its temperature degradation.

Ni, C., Cassidy, M. and Irvine, J. (2018). ***Image analysis of the porous yttria-stabilized zirconia (YSZ) structure for a lanthanum ferrite-impregnated solid oxide fuel cell (SOFC) electrode.*** **Journal of the European Ceramic Society, 38(16), pp.5463-5470.**

In this study, two yttria-stabilized zirconia (8mol% of yttria) materials are used in order to manufacture porous electrolytes for SOFCs. The manufacturing process used during this investigation was to applied a uniaxial pressure of 149MPa on both powders followed by a sintering treatment. The cathode used to study the impregnation and carry out the electrochemical tests was made of lanthanum ferrite. The results show that for smaller particles of powder, the grain growth and the decrease in surface area are higher during the sintering process than with particles with higher volume. Thus, in this case, resistance and polarization increase when the particle size decreases (due to a decrease of the surface area of the porous scaffold in yttria-stabilized zirconia).

Now considering both AM methods and use of zirconia for SOFCs electrolyte, the following articles give an extensive overview of the current knowledge on the topic and some of the distinct existing methods.

Masciandaro, S., Torrell, M., Leone, P. and Tarancón, A. (2018). ***Three-dimensional printed yttria-stabilized zirconia self-supported electrolytes for solid oxide fuel cell applications.*** **Journal of the European Ceramic Society, 39(1), pp.9-16.**

In this study, a 3D stereo-lithographic printer has been used to create self-supported electrolytes of yttria-stabilized zirconia (3YSZ). The method allowed the obtention of thin layers up to 25 µm. A thermal treatment of 70 h was carried out before sintering in order to remove all organic compounds so as to avoid crack formations. Flat membranes with a thickness of 340 µm and an active area of 1.54cm^2 as well as honeycomb cell of 260 µm -thick hexagonal cells were created. Once the electrolyte was sintered, they were painted with NiO-YSZ (anode) and LSM-YSZ (cathode) pastes in order to form the electrode. The cells were then characterized from a microstructural and electrochemical point of view.

Tomov, R., Krauz, M., Jewulski, J., Hopkins, S., Kluczowski, J., Glowacka, D. and Glowacki, B. (2010). ***Direct ceramic inkjet printing of yttria-stabilized zirconia electrolyte layers for anode-supported solid oxide fuel cells.*** **Journal of Power Sources, 195(21), pp.7160-7167.**

In order to manufacture the dense yttria-stabilized zirconia electrolyte during this investigation, direct ceramic inkjet printing was employed. The materials used to manufacture both the anode and the cathode were the same than in the precedent article, but where fabricated through a tape casting technique. The goal of this study is also to optimize the printing parameters in order to increase the efficiency of the final cell, such as the pressure applied or the opening time from the suspension. The overlapping parameter is also investigated.

Esposito, V., Gadea, C., Hjelm, J., Marani, D., Hu, Q., Agersted, K., Ramousse, S. and Jensen, S. (2015). ***Fabrication of thin yttria-stabilized-zirconia dense electrolyte layers by inkjet printing for high performing solid oxide fuel cells*****. 273, pp.89-95.**

Finally, in this article are presented the results of 1.2 µm-thick, 16cm^2, dense and gas tight electrolyte layers made of yttria-stabilized zirconia by inkjet printing. The ink was composed of highly diluted (<4 vol%) nanometric 8YSZ powders (50nm) in an aqueous medium made of 80wt% water and 20wt% ethanol. The anode layer was composed of NiO/YSZ, which was deposited by screen printing onto the electrolyte. The cathode was also made of LSM/YSZ. This paper focuses on the characterization of the inks used as well as the efficiency of the overall cell. A total of 5 layers was necessary to obtain a gas tight electrolyte.

It can be relevant to say that, despite the numerous investigations in the fields concerned by the present investigation, only a few articles are related to the use of robocasting method for the manufacture of SOFCs electrolyte with yttria-stabilized electrolyte. For this reason, this study is one of the first on the subject and can be seen as a continuation of the new research line of the CIEFMA's group.

3. Goal

The principal goal of this investigation is to reach the optimum properties for SOFCs with printed fully dense 8Y-TZP electrolytes, by using a robocasting AM technique, in order to develop a systematic protocol for printing fuel cell electrolytes.

In order to obtain the most efficient device, various aspects will be characterized:

- Firstly, different compositions for the ceramic paste (8Y-TZP/hydrogel), printing temperatures, and injection tip diameters will be investigated in order to optimize the microstructure, specimen with the lowest porosity, for the printed electrolyte part.
- The flowing rate of the printed material as well as the shrinkage caused by the sintering process will be investigated in order to predict the behavior of the material.
- Two different geometries, cylindrical and tubular will be used in order to print the electrolyte part and will then be compared from different mechanical points of view.
- The mechanical properties (hardness, fracture toughness and the elastic modulus) and the microstructure (density, superficial porosity and grain size) of the electrolyte will be characterized in order to assess the optimal composition and to ensure the functionality of the final electrolyte.

Broadly speaking, the **main goal** of this study is to establish a permanent mode of production of SOFCs electrolyte with AM robocasting methods in order to normalize the overall process and to enhance the mechanical and electrical properties of the cell.

4. Experimental process

4.1. Materials

In this section will be detailled the different materials used during the realization of this Master's thesis. These materials were used in order to produce the ceramic paste to print the electrolyte.

4.1.1. Pluronic F-127®

Pluronic F-127® is a poloxamer, which is a family of non-ionic triblock co-polymers. It is composed of two different chain units. The repeat unit of this copolymer consists of two external blocks of polyethylene oxide (PEO) which is hydrophilic and a central block of hydrophobic polypropylene oxide (PPO) as it is depicted in **Fig.4.1**. Therefore, this polymer presents amphiphilic and temperature-responsive behaviors.

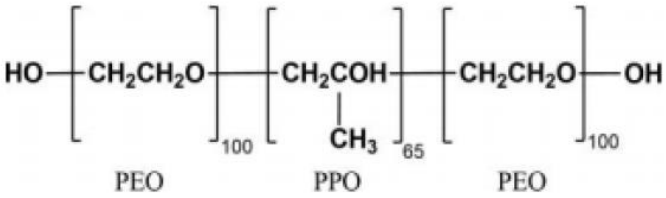

Fig.4.1 *Polymeric-chain of the Pluronic F-*127® **[60]**.

Indeed, this kind of copolymer exhibits an inverse thermal mechanical behavior in aqueous dissolutions, meaning that it undergoes a gelling process when the temperature of the system increases. This phenomenon can be explained by the difference in the critical dissolution temperature between the PEO and the PPO. Therefore, the gelling temperature and mechanical strength of the gel is a function of the composition and ratio of PPO over PEO.

In this Master's thesis, the Pluronic F-127® is used to create a hydrogel with distilled water. The behavior of the obtained solution, depending on the concentration of copolymer used, will exhibit a liquid behavior below the sol-gel transition temperature. Passing by this temperature, the shear/viscosity module ratio will increase by several orders of magnitude in a narrow range of temperature. This point must be taken into consideration as during the investigation the hydrogel will be used along with ceramic powder in order to print an electrolyte part. Therefore, the concentration in water will possess a critical value beyond which the porosity created during the sintering process would be catastrophic and cause the failure of the material.

As it will be used 25wt% of pluronic for 75wt% of distilled water to manufactured the hydrogel, which is more or less equivalent to 30w/v%, the gelation point of the hydrogel will be close to 14°C, as it can be seen in **Fig.4.2**. Therefore, the hydrogel will have a liquid state once put in a fridge, and recover its gelling state at ambient temperature for printing.

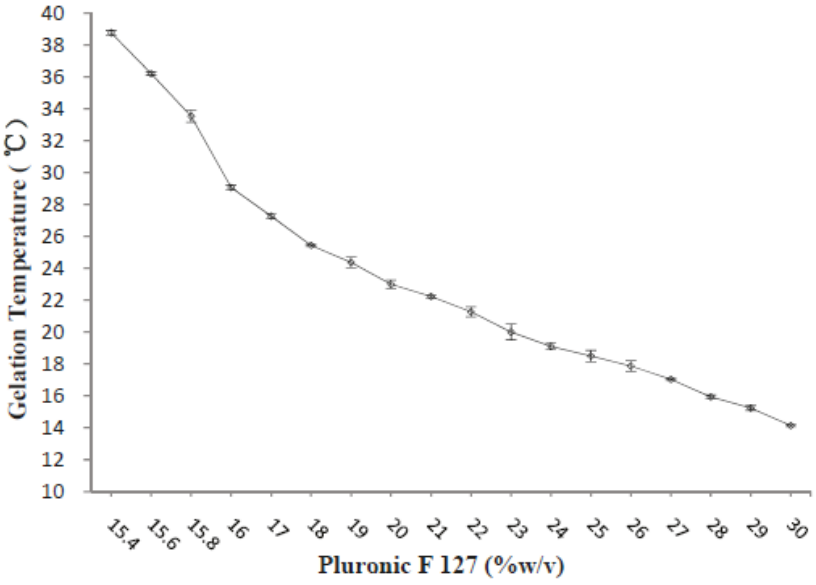

Fig.4.2 *Gelation temperature and thermoreversible behavior of Pluronic F 127® gel* **[61]**.

The datasheet of this material can be found in ***Annex A.1***.

4.1.2. Zirconia base material, 8Y-TZP

In order to manufacture the electrolyte of the SOFC, the ceramic charge used is a powder of zirconia stabilized with 8 mol% of yttria. Due to the amount of stabilizers added, this material can be considered as fully stabilized zirconia **[53]**. The different properties and crystallography of this ceramic can be found on the ***section 1.3.1***.

Considering the amount of additive in the composition, it can be seen in **Fig.4.3** the phases in presence inside the material, represented by the red line, regarding the preparation temperature.

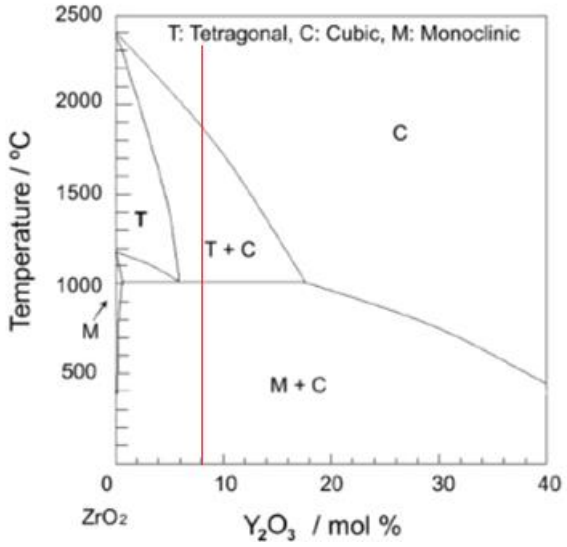

Fig.4.3 *Part of the binary phase diagram of zirconia and yttria* **[62]**.

The material used during this project was provided by TOSOH, and does not contain any binder and will therefore be considered as pure 8 mol.% yttria stabilized zirconia.

4.2. Ceramic pastes

In order to print the ceramic material, it is necessary to use the hydrogel made of pluronic F-127® and distilled water so as to create a ceramic paste with the appropriate viscosity to be processed by additive manufacturing.

4.2.1. Manufacturing of the hydrogel

The creation of the hydrogel consists in mixing the Pluronic F-127® with distilled water via the help of a SpeedMixer, presented if **Fig.4.4 (a)**. The proportion used in this investigation will be of 25 wt.% of copolymer and 75 wt.% of distilled water. This ratio corresponds to a gelation temperature of approximately 14°C (see **Fig.4.2**) and has been chosen in order to easily obtain a gel state at room temperature and a liquid state in the fridge (temperature lower than 5°C). In order to ease the mixing of the gel, the following steps of preparation for 100g of hydrogel were realized:

- Weight and mix (with a SpeedMixer DAC 150.1 FVZ-K) during 5min at 3500rpm 25g of Pluronic F-127® with 25g of distilled water at ambient temperature,
- "Break" the mixture obtained with a spatula in order to maximize the surface contact of the gel with the rest of distilled water,

- Weight, add and mix during 5min at 3500rpm 50g of distilled water with the first mixture obtained (it can be necessary to add more than 50g of H_20 because the mixture is heated during the first step of mixing and water can evaporate),
- Store the final hydrogel at a constant temperature inferior to the gel/sol transition temperature during 24h (in a fridge at 4°C) in order to eliminate the bubbles generated during the mixing process.

Once those steps realized, it is possible to manufacture the ceramic paste.

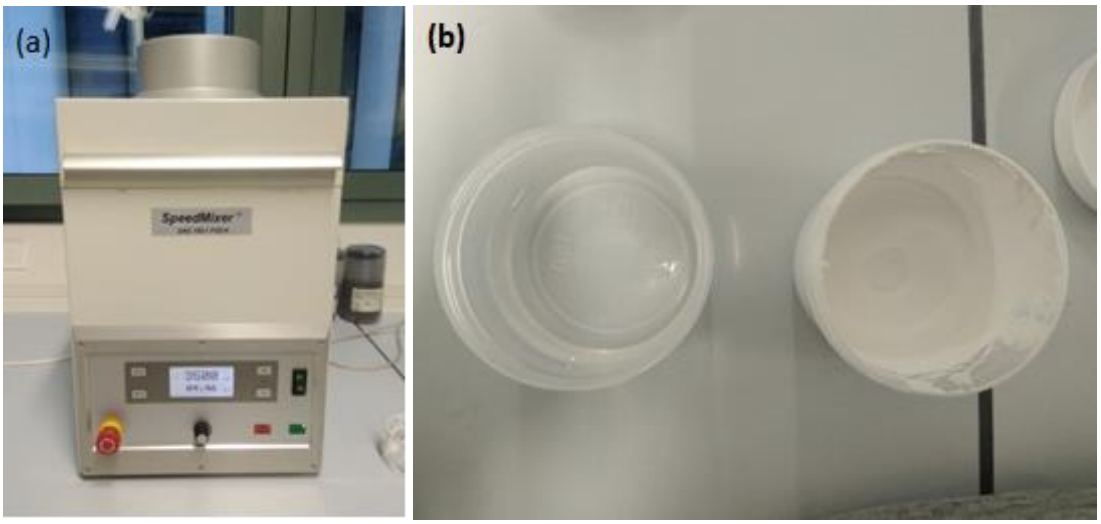

Fig.4.4 ***(a)*** *SpeedMixer DAC 150.1 FVZ-K,* ***(b)*** *the hydrogel (left) next to the ceramic paste (right).*

4.2.2. Preparation and determination of the optimal composition for the ceramic paste

The making of ceramic pastes is realized following the next steps:

- Weight and mix during 1min at 3500rpm the total amount of ceramic powder with the hydrogel depending on the proportions required, and
- let the obtained paste rests during 2h.

Once those steps achieved, it is possible to print the desired samples.

In order to determinate the adequate composition of the ceramic paste (ratio between the ceramic powder and the hydrogel), it is necessary to evaluate the printing windows of this material, which also depends on the temperature, especially because of the copolymer's properties. Therefore, different proportions of ceramic powder of 8Y-TZP, from 20 wt. % to 75 wt. % and afterwards sintered in order to be able to evaluate the final microstructure and mechanical property for the printed specimen. In order to evaluate the influence of the temperature on the ceramic paste printability, the different pastes were, stored in plastic syringe, where the ceramic paste is maintained in a controlled atmosphere water environment at constant temperature of 30, 35, 40, 45 and 50°C during 30 min

before being printed in order to be able that the ceramic paste employed during the printing process keep the same temperature.

4.3. Additive manufacturing technique

Robocasting technique will be used during this investigation as an AM process to print the different geometries for the 8Y-TZP electrolyte parts. The model of the machine is a RepRap BCN 3D+ printer with dual paste head, supplied by the "Fundació CIM at the Technical University of Polytechnic-BarcelonaTech". Aside from the preparation of the ceramic paste, in order to print the different samples, the use of different softwares was required in order to obtain a 3D-model of the part and the code readable by the 3D-printer.

4.3.1. Parts of the machine

In order to print in 3D, the machine was made in a way that enables it to move according the 3-axis of direction (X, Y, Z). The head of the system ensures the movements in the *X*- and *Z*- axis, while the print bed ensures the *Y*- direction.

The different parts of the system are detailed as follow, numbered as presented in **Fig.4.5**:

1. **Printing bed:** This part consists of a 180mmx140mm rectangular glass plate where the sample is printed. In order to minimize the adherence of the sample with the bed, a cellulose filter paper can be used.
2. **Printing syringe:** This removable part made of plastic represents the part where the ceramic paste is loaded and pushed by the piston. It is equipped with a syringe tip, a small part which determines the diameter of the extruded material.
3. **Gear system:** Attached to the printer frame, this part is composed of eight gears that transmit the force to the piston.
4. **Piston:** Part coupled to the gear system by a toothed face and to the syringe by a male-female system. Its main role is to convert the rotational movement created by the gears and motor into the uniaxial force in order to extrude the ceramic paste.
5. **Control knob:** Interface which allows the control of the printer functions. It contains a SD slot in which the gcodes files are stored.
6. **Frame of the printing machine:** Structure made of metallic and plastic materials, which sustains the other parts.
7. **Sample:** Ceramic's sample being printed.

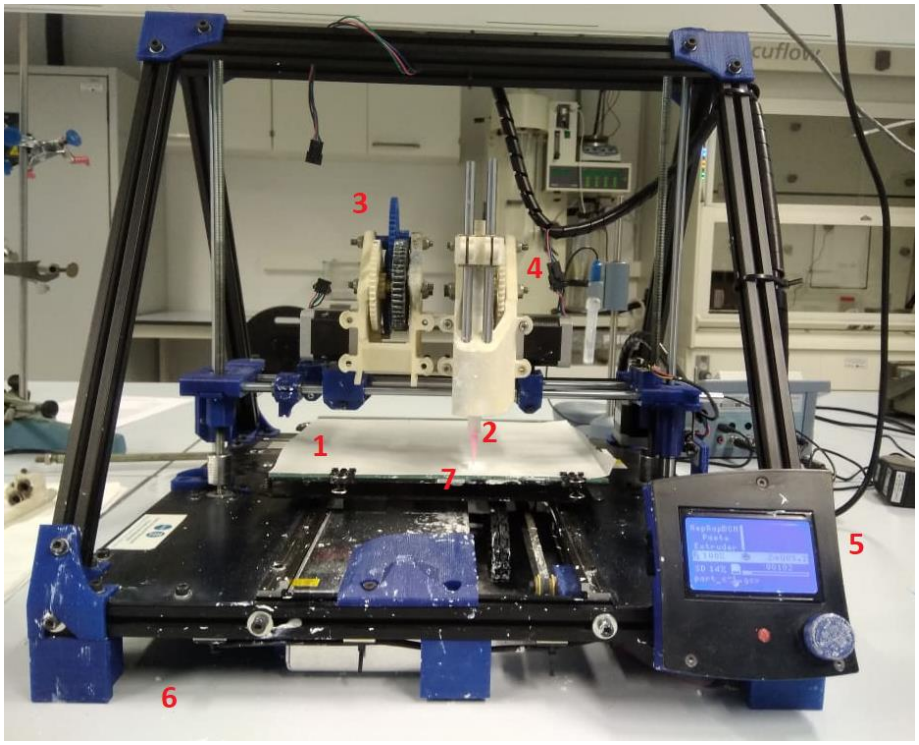

Fig.4.5 *3D robocasting printer BCN3D with numbering.*

4.3.2. Modeling

The 3D-modeling of the part is realized on a Computer Assisted Design (CAD) software. Different softwares are able to ensure this function such as CATIA or SolidWorks. During this first step, the geometry is determined, and in this investigation three different geometries are printed: cylindrical, tubular (both shown in **Fig.4.6**) and hexagonal.

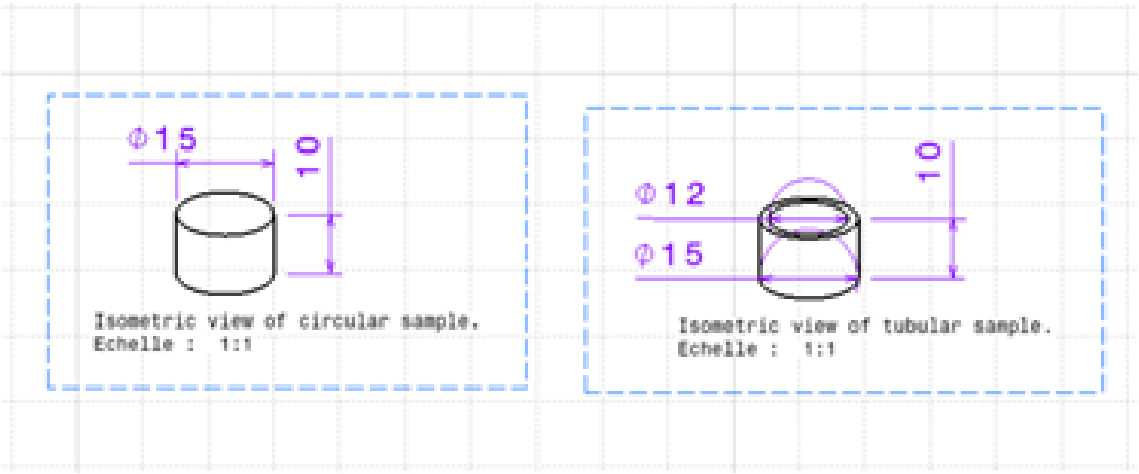

Fig.4.6 *Design of the two different geometries used to print the sample.*

4.3.3. Set-up

Once the part is designed, it can be saved as a .stl file, format which can be used by the next software, Slic3r. This second software allows the user to generate a gcode from a 3D-file object (.stl). To ensure this function, the software generates each layer which need to be printed depending on the conditions entered by the user, such as the kind of printer, material or geometry. This code takes into consideration: the position of the part on the bed, the kind of infill used for each layer, the various velocities of infill for the different printing moves, for moves without printing, the infill percent and the velocity of heating and cooling among others. It also needs to take into consideration the diameter of the tip used as well as the size of the bed of the machine.

The most important characteristics can be found in **Table 4.1**:

Table 4.1. *Main parameters used to print the different samples.*

SOFC geometry	**Infill**	**Pattern**	**Speed for print moves**						**Layer height**	**Noozle diameter**
			Perimeters	*Small perimeters*	*Infill*	*Solid infill*	*bridges*	*Gap fill*		
Circular	100%	Rectilinear	10 mm/s	5 mm/s	10 mm/s	10 mm/s	10 mm/s	10 mm/s	0.58 mm	0.58 mm
Tubular	100%	Rectilinear	10 mm/s	5 mm/s	10 mm/s	10 mm/s	10 mm/s	10 mm/s	0.58 mm	0.58 mm

Concerning the printing conditions, they are identical during all phases except during the determination of the printing window, and are the following ones:

- Air temperature: 19 to 22°C
- Paste temperature: 30°C
- Humidity: 55 to 70%
- Pressure: 1atm

Before each printing, in order to ensure the best homogeneity of the paste and obtain the required viscosity, the paste was mixed during 20 seconds at 3500rpm with the SpeedMixer DAC 150.1 FVZ-K (see **Fig.4.4 (a)**).

4.4. Sintering process

Once the green body or printed specimen is done, a thermal treatment named sintering process is applied in order to increase the density of the ceramic material and get rid of the hydrogel

initially present in the ceramic paste. Once carried out, this process of sintering allows to obtain the final geometry, microstructure and mechanical properties. In this investigation, it was realized in a Nabethern furnace, shown in **Fig.4.7**, with the thermal treatment presented in **Fig.4.8**.

Fig.4.7 *Photography of the Nabethern furnace.*

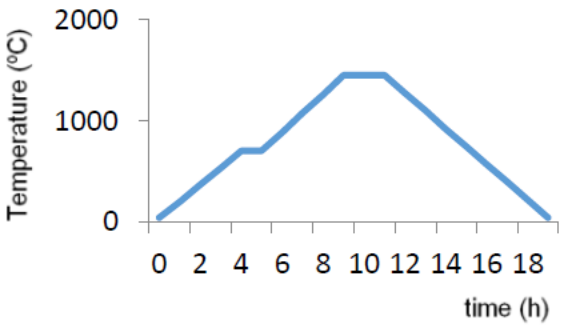

Fig.4.8 *Schematic representation of the thermal treatment for the sintering process employed to densify the printed ceramic specimens.*

This thermal treatment consisted in heating up to 700°C at a first heating speed of 2.9 °C.min^{-1}. Then maintaining a temperature of 700°C during 1h. After this first step, the temperature was increased up to 1450°C with a heating speed of 3.125°C.min^{-1}, and maintained constant during 2h. The cooling speed was then of -2.9°C.min^{-1} until reaching ambient temperature.

To understand what happened from the structural point of view of the zirconia, it is important to understand that the sintering process consists in compacting the material without melting it. This process involves the diffusion mechanism of the atoms which is enhanced at high temperature.

Therefore, the atoms diffuse across the particles boundaries and fuse them together, which allow the obtention of a unique solid piece.

It is also important to take in consideration that the treatment temperature will have an influence on the grain size, and thus, on the mechanical properties of the final piece. As it can be seen in this study **[63]**, where zirconia was sintered at different temperatures, the grain size increases with the temperature used (see **Fig.4.9**).

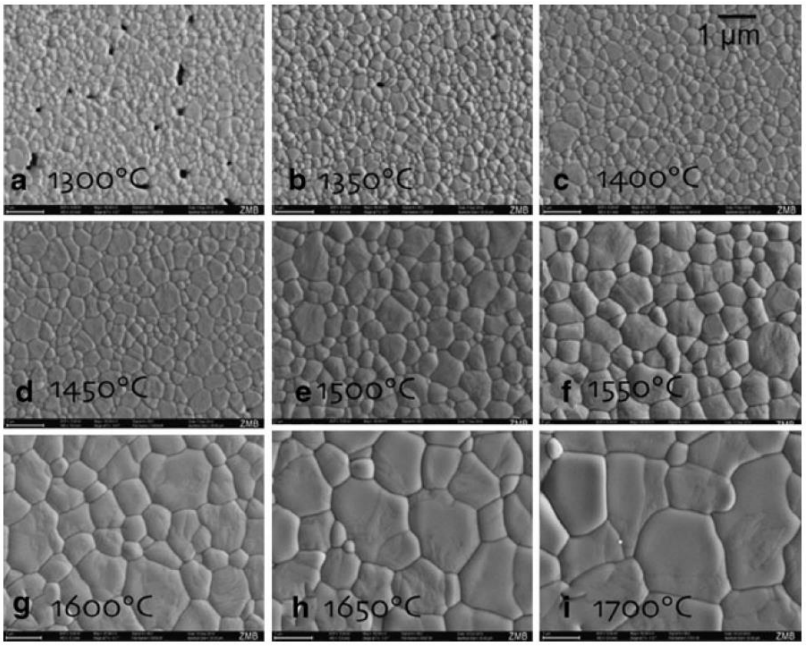

Fig.4.9 *Zirconia grain size after different sintering temperature* **[63]**.

Was also measured the flexural strength of the different samples regarding their sintering temperature, and show the results present in **Fig.4.10**. As it can be seen, the mean flexure strength increases with the sintering temperature up to a certain point around 1500°C, where it begins to decrease drastically. This is due to the presence of porosity or space between the grains at low sintering temperatures, because the atom diffusion was not great enough to fuses all the grains together, while at high sintering temperature, the high size of the grains reduces the mechanical properties. As an example, to explain how a greater grain size reduce the mechanical properties, it can be said that the grain boundaries reduce crack propagation due to their high energy, and because there will be a higher quantity of grain boundaries for small grain in the material, it will be more resistant to crack propagation than a material with higher grain size.

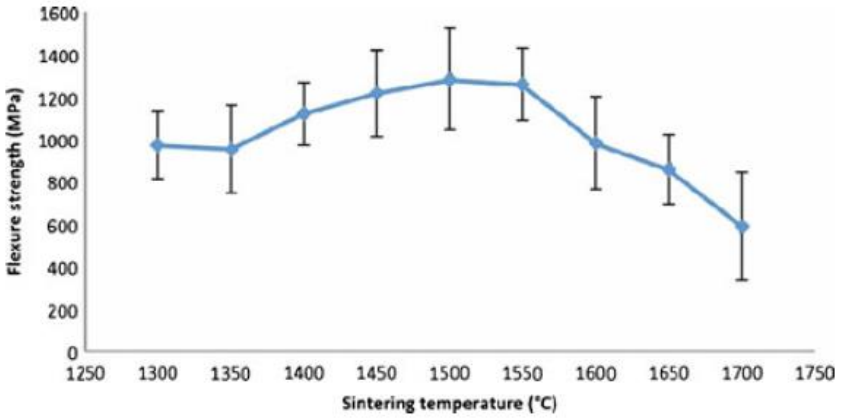

Fig.4.10 *Mean flexural strength of zirconia after different sintering temperatures* **[63]**.

4.5. Polishing process

Prior to the microstructural analysis and the evaluation of the mechanical properties, it is required to obtain a plano-parallel surface with a superficial roughness which magnitude's order is inferior or equal to the micrometer scale. Indeed, characterization tests such as nano-indentation or microscopic observations are extremely sensible to those variations of surface's roughness. Therefore, in order to obtain more precise values, a polishing stage is needed on the diverse samples obtained, by CIP and AM technique.

Because of the size of the samples, which order of magnitude was one centimeter, it was necessary to embedded the printed specimens in order to be able to manipulate the specimens and subsequently polish them. Two different materials have been used in this Master's thesis in order to embed the different specimens:

I) Bakelite, which was used for the sample obtained by Cold Isostatic Pressure (CIP). Bakelite is the fabrication and trade name of a phenoplast material named polyoxybenzylmethyleneglycolanhydride. It was the first plastic ever made from synthetic components **[64]**. The specimens were embedded at 180°C and a constant force of 15kN during 5 min. After this treatment the bakelite was cold down until room temperature by using tape water. In the case of this Master's thesis, the samples obtained with CIP were too fragile to be encapsulated directly in Bakelite (see **Fig.4.11 (a)**), for this reason, plates of Bakelite were processed, onto which the ceramic samples were glued with cyanoacrylate (see **Fig.4.11 (b)**). Once the polishing process realized, acetone was used to remove the superglue and detached the sample from the Bakelite.

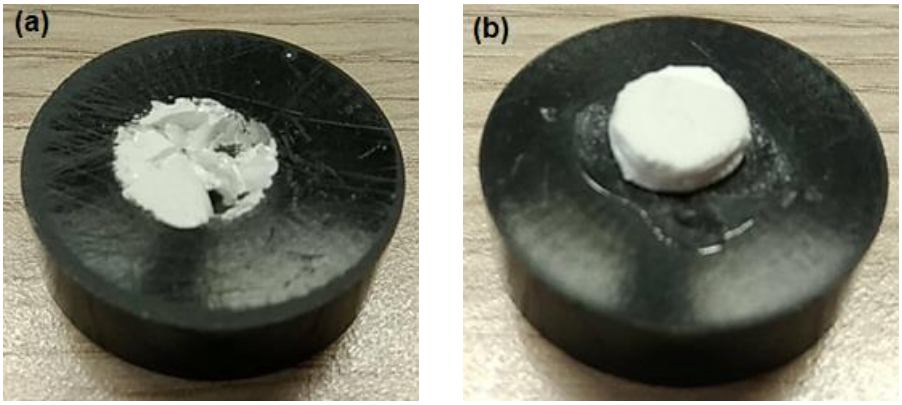

Fig.4.11 *Photography of the sample encapsulated in Bakelite* ***(a)*** *and glued on Bakelite* ***(b)***.

II) Resin, which was used to encapsulated the samples obtained through the 3D-printing process. The resign used for the 3D-printed samples was composed of synolite, which is a resign of unsaturated polyester based on ortoftalic acid of low viscosity as well as preaccelerated **[65]**, and of methyl ethyl ketone peroxide (MEKP), presented in **Fig.4.12 [66].** This last component is used as a catalyst in the reaction in order to start the polymerization reaction of the unsaturated polyester resin.

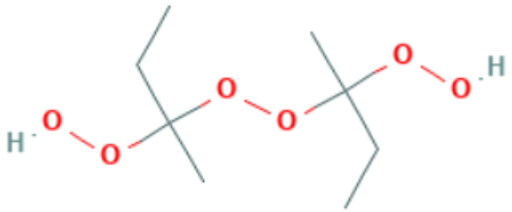

Fig.4.12 *Schematic representation of the MEKP* **[66]**.

Once the sample placed in a silicon mold, with the face to analyze downwards, both of the components are poured with a ratio 30/1 (synolite/MEKP). Then, the sample must be left curing during 48 hours in order for the crosslinking to form and obtain a solid material around the sample.

Subsequently, the specimens were polished by using the polishing process protocol (see **Table.4.2**). All the different polishing steps were conducted by using a conventional polishing machine from Struers (LAboPol-5), shown in **Fig.4.13** under a rotational velocity held constant and equals to 150rpm.

Table.4.2 *Polishing process protocol.*

Disk used	Grinding paper (1200)	Cloth MD-Dac	Cloth MD-Dac	Cloth MD-Dac	Cloth MD-Nap
Suspension	Water	Diamond suspension (30 µm)	Diamond suspension (6 µm)	Diamond suspension (3 µm)	Colloidal silica suspension
Time (min)	5	5	10	15	20
Order	1	2	3	4	5

Fig.4.13 *Picture of the polishing machine Struers (LAboPol-5).*

4.6. Microstructure

The different methods employed along this Master's thesis to evaluate the microstructure of the different specimens are detailed and explained along this section.

4.6.1. Density, *ρ*

The determination of the sample's density is one of the techniques that does not require a prior operation of polishing, and was therefore performed directly after the sintering process. The Archimedes method allows obtaining, considering the Archimedes principle, the bulk density of the sample by using the **eq.4.1** and thus, estimate the amount of open porosity in each of them. It is worthy necessary to mention the importance of the parameter, which will directly affect the mechanical response of the desired specimen.

The Archimedes principle states that: "the upward buoyant force that is exerted on a body immersed in a fluid, whether fully or partially submerged, is equal to the weight of the fluid that the body displaces and acts in the upward direction at the center of mass of the displaced fluid." Archimedes of Syracuse **[67]**.

Deriving from this physical law, by measuring the mass of an object in water (or fluid with a well-known density) and its mass in the air, it can be determined the thrust force exerted. Within this context, the density can be measured by using the following equation:

$$\rho_{sample} = \frac{m_{air}}{m_{air} - m_{water}} \times (\rho_{water} - \rho_{air}) + \rho_{water} \qquad \textbf{(eq.4.1)}$$

Where m_{air} and m_{water} represent respectively the weight of the sample in air and in distilled water. ρ_{water} and ρ_{air} are expressed in g.cm^{-3} **[68]** and depend on the temperature and the relative humidity of the environment (see ***Annexes C.1*** and ***C.2***).

The measurements were realized with an Archimedes machine Mettler Toledo XS-204, shown in **Fig.4.14**.

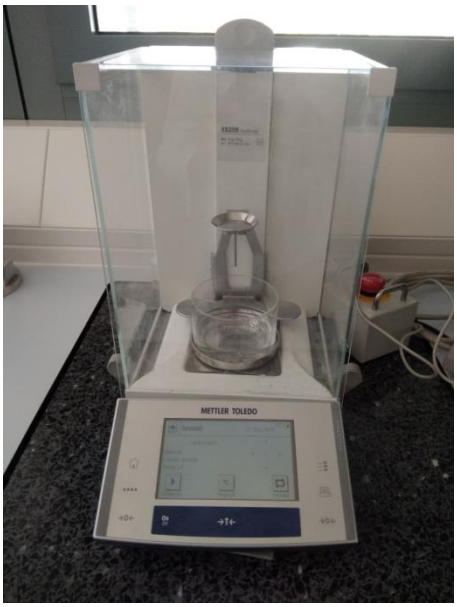

Fig.4.14 *Analytical balance Mettler Toledo XS-204 employed to determine the density of the printed specimens by using the Archimedes method.*

4.6.2. Dimensional parameters

The dimensional parameters, used in order to determine the shrinkage of the different materials, were measured with a micrometer.

4.6.3. Optical and laser scanning confocal microscope

The functioning of an optical microscope (OM) is based on the use of visible light and a system of lenses to magnify images of small objects **[69]**. Along this Master's thesis, the device used is an Olympus BX53M microscope presented in **Fig.4.15**, which relies on LED instead of halogen light **[70].**

The aim of this microscope use was **i)** to measure the diagonal sizes of the Vickers indentation as well as **ii)** the cracks created in order to obtain the hardness and the fracture toughness of the different samples, respectively.

On the other hand, the laser scanning confocal microscopy (LSCM), allows to increase the optical resolution and contrast of the obtained image. The method consists in using point illumination as well as a spatial pinhole to block out-of-focus light in image formation. Therefore, only light produced by fluorescence very close to the focal plane can be detected, which allows the obtention of higher resolution than with a wide-range microscope **[71]**. LSCM was used to study the surface porosity and defects of the different printed samples. The apparel used during this Master's thesis was an OLYMPUS Lext OLS 3100.

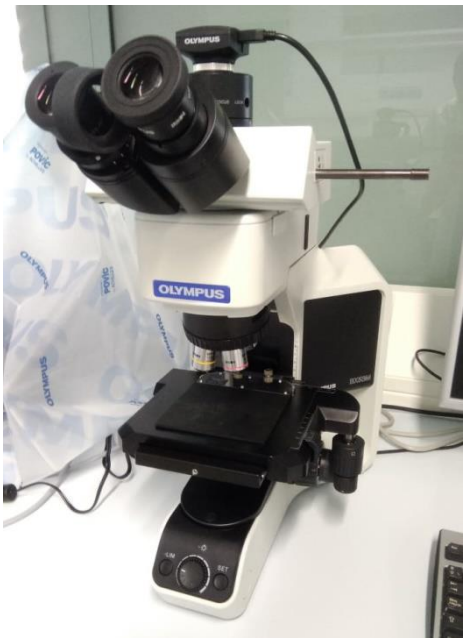

Fig.4.15 *Optical microscope Olympus BX53M.*

4.6.4. X-ray diffraction

X-ray diffraction (XRD) is a non-destructive analytical technique and is used to reveal information about the crystallography, chemical composition or physical properties of a material. It is

considered an elastic scattering technique (due to the amplitude of the scattering) and is especially used for crystalline materials such as the major part of ceramics, metals, composite materials among others.

Crystalline materials present an established crystallographic pattern and consist of a regular atom and ion arrangement with interatomic spacing of a magnitude's order close to 1 Å. The ordered structures are called crystal lattice and present identifiable geometric shapes.

The functioning of the XRD is based on observing the scattered intensity of an X-ray beam hitting the sample's surface as a function of incident and scattered angle, polarization and wavelength or energy produced. In order to produce X-rays, an X-ray tube is often used. It consists of a vacuum tube that contains a cathode and an anode. The cathode generates a stream of electrons into the vacuum, while the anode, made of tungsten in order to evacuate the heat produced, collects the electrons. About 1% of the collision's energy is emitted as X-rays, while the other 99% are emitted as heat. Therefore, an additional refrigerant system is needed **[72]**.

The measure of the elastic scattering is based on the Bragg's law, see **Eq.4.2 [72]**.

$$2 \times d \times \sin(\theta) = n \times \lambda \qquad \textbf{(Eq.4.2)}$$

Where d is the space between two successive planes, ϑ the incident angle of the X-ray beam, λ the wavelength of the beam, as it is shown in **Fig.4.16**

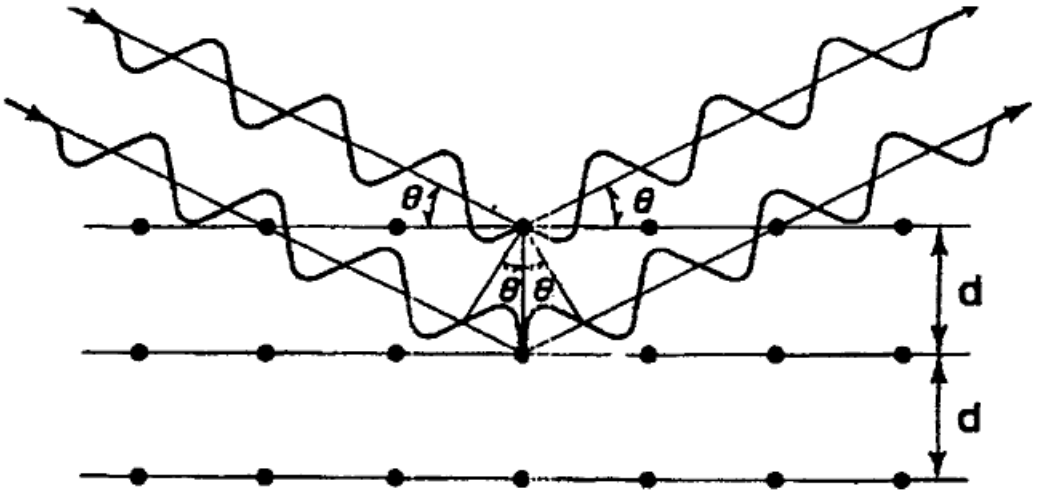

Fig.4.16 *Schematic representation of the interaction between the atomic planes of the material and the X-ray beam* **[72]**.

In this investigation's work, an XRD equipped with a PIXcel3D detector was used, see **Fig.4.17**.

Fig.4.17 *XRD equipment.*

4.6.5. Field Emission Scanning Electron Microscope

Field Emission Scanning Electron Microscope (FESEM) (see **Fig.4.18**) is a technique based on the Scanning Electron Microscope (SEM), with a slight change on the emitter type used (thermionic emitters). A SEM produces images of a sample by scanning the surface with a focused electron beam. An electron beam is directed to the sample and interact with the atoms on the surface. This phenomenon produces different signals that contain information about the surface topography and sample composition. This technique requires the application of vacuum in order to operate. A SEM can achieve a resolution superior to 1 nm.

Different modes for FESEM exist, relying on the different resulting interactions than can be represented as shown in **Fig.4.19**. Some of said modes are detailed in the following paragraphs:

- **Detection of secondary electrons:** it is the most common SEM mode. It consists in detecting the secondary electrons emitted by the atoms throughout their excitation by the electron beam. The quantity of those entities depends on the specimen topography.
- **Detection of backscattered electrons:** those electrons come directly from the electron beam and are reflected by the atoms of the sample. Heavy elements such as lead backscatter electrons more strongly than lighter ones. Therefore, the bigger an element, the brighter it will appear in the observation's image. This detection technique allows to obtain contrast between the different phases and chemical compositions of a sample's surface. It can also be used to determine the crystallographic structure of the specimen, thanks to the diffraction of the electron backscatter.

- **X-ray microanalysis:** some SEM devices with the required equipment are able to detect the characteristic X-rays that are produced by the interaction of electrons with the sample. This analysis may be used to map the distribution and estimate the composition of the different elements in the sample **[73]**.

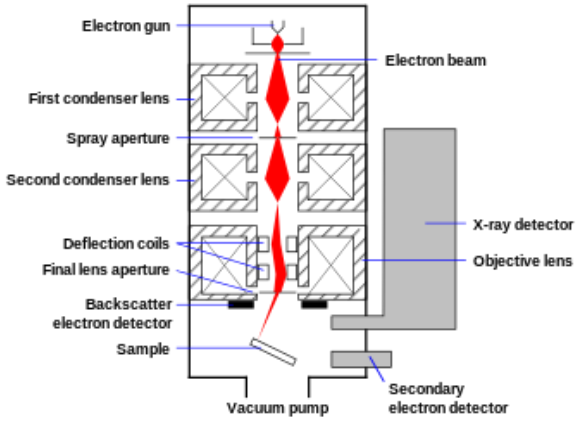

Fig.4.18 *Schematic representation of a FESEM* **[74]**.

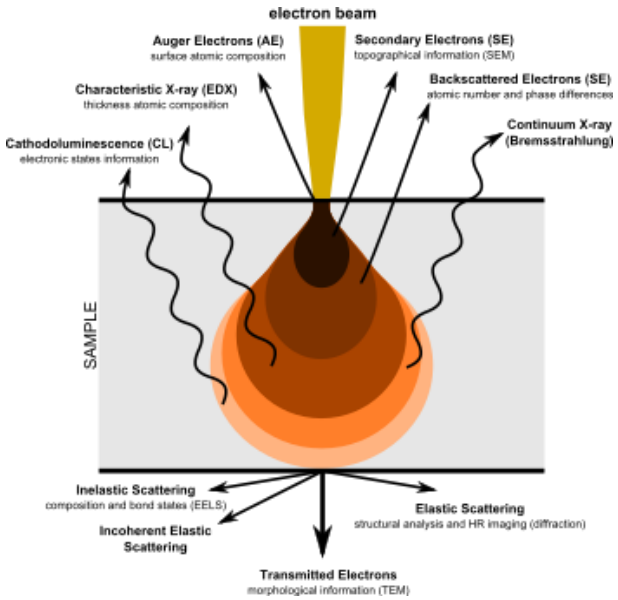

Fig.4.19 *Schematic representation of the signals emitted from different parts of the interaction material volume* **[74]**.

4.7. Mechanical properties

4.7.1. Vickers hardness test

This test is the most conventional methodology to measure the composite hardness of the material. It is one of the easier hardness tests since the formulas to measure the hardness as well as the fracture toughness are independent of the geometrical properties of the indenter. The method consists in observing the ability of the material to resist plastic deformation created by the pyramidal indenter.

The indenter is a diamond with the form of a square-based pyramid and is represented in the **Fig.4.20.**

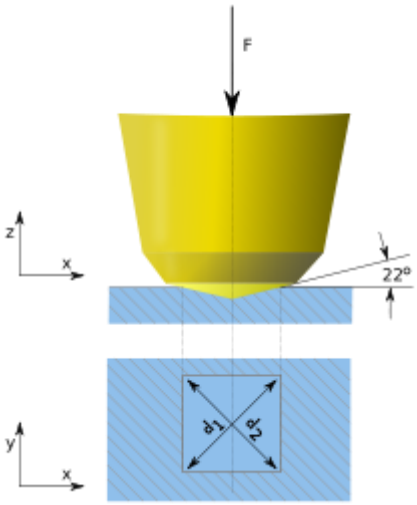

Fig.4.20 *Schematic representation of the Vickers indenter* **[75]**.

The hardness of the material corresponds of the ratio $\frac{F}{A}$, where *F* is the force applied by the machine (in kgf or N with 1 kgf = 9.80665 N) and *A* is the area of the indentation (in mm²). Therefore, the Vickers pyramid number *HV* can be calculated with the **Eq.4.3**. This property represents the resistance to localized plastic deformation induced by either mechanical indentation or abrasion.

$$HV = 0.1891 * \frac{F}{d^2} \qquad \textbf{(Eq.4.3)}$$

Where *F* is the applied force (N) and *d* the mean of the diagonal size (mm) (**Fig.20**). Therefore, *HV* is directly expressed in MPa.

Vickers hardness number are reported according to the following form: **xxxHVyy/zz** where **xxx** is the hardness number, **HV** gives the hardness scale (Vickers), **yy** indicates the load used in kgf, and **zz** is the loading times (used only if it differs from 10s to 15s). **[75]**

Once the hardness of the material measured, can be obtain the indentation fracture toughness (K_{IC}) of the material with the **Eq.4.4 [76]**. This property represents the capacity of the material to withstand facture.

$$K_{IC} = 0.018 \times \left(\frac{E}{HV}\right)^{0.5} \times \frac{P}{c^{1.5}} \qquad \textbf{(Eq.4.4)}$$

Where *E* is the Young's modulus in GPa, *HV* is the Vickers hardness in GPa, *P* is the applied force in N, *c* is the size of the crack in mm (see **Fig.4.21**) and K_{IC} the fracture toughness in $MPa\sqrt{m}$.

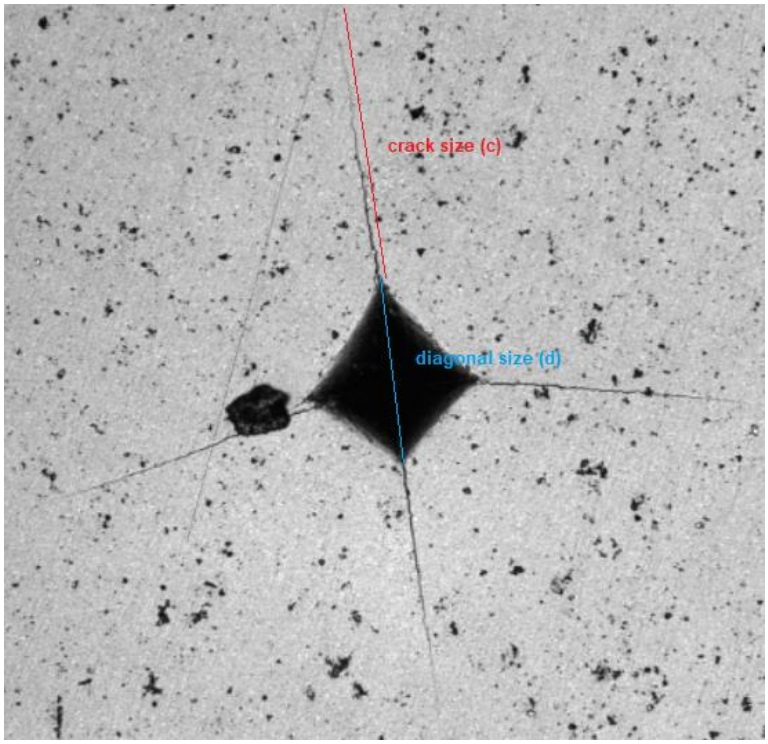

Fig.4.21 *Residual imprint micrograph obtained by CLSM performed at 10 kgf.*

In order to measure both parameters, a wide range microscope was used. So as to perform the test, it must be taken into consideration that the plastic properties of the material undergo local modification during the indentation. Therefore, each indentation must be spaced from the precedent ones. For each studied sample, five imprints at different loads (10, 5, 0.5 and 0.1kgf) where done by using the EMCO-TEST Durascan equipment (see **Fig.4.22**)

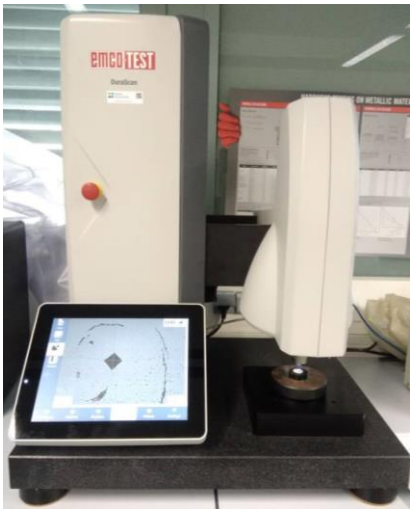

Fig.4.22 *Photography of the Vickers hardness machine EMCO-TEST Durascan.*

4.7.2. Nanoindentation technique

Nanoindentation techniques consists in depth-sensing indentation (DSI) techniques used in order to obtain mechanical properties from a very small volume of material. In DSI, the load and displacement of the indenter are continuously recorded as it is pressed into and removed from the sample. It is one of the most powerful means of measuring mechanical properties at the nanoscale. Nanoindenters can be schematize as in **Fig.4.23**.

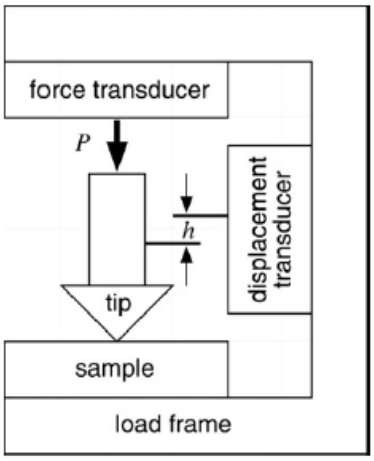

Fig.4.23 *Schematic representation of the nanoindenter where P represent the load and h the displacement* **[77]**.

The main goal of the nanoindentation technique is to obtain the mechanical properties of a material, such as the elastic modulus (E) or the hardness (H) as well as the *P-h* curves. In order to measure the different mechanical properties, the Berkovich indentation will be used in this Master's

thesis. The Berkovich indentation allows to obtain the values of E which represents the stiffness of a solid material, as well as H which is a measure of the resistance to localized plastic deformation induced by the test. It consists in introducing a tip in the surface of the material with a specific force and measuring the depth of the residual imprint. The tip used consists on a three-sided pyramid, where the angle between the centerline and the three faces equals 65.3° α, as it is shown in **Fig.4.24**.

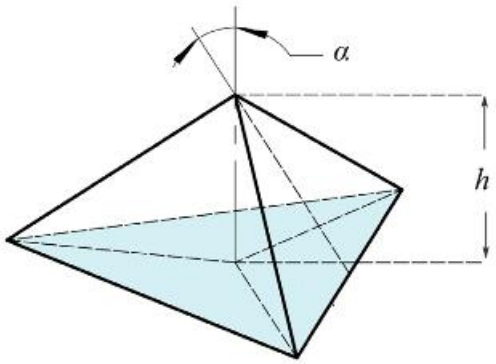

Fig.24 *Representation of the Berkovich indenter* **[78]**.

Both the values of E and H will be measured at the submicrometric length scale thanks to the Olivier and Pharr method (**Eq.4.5** and **Eq.4.6**) **[79]**. It consists in measuring the depth h as a function of the applied force P during the loading-unloading cycle.

$$H = \frac{P}{A} \qquad \textbf{(Eq.4.5)}$$

$$E = \frac{1}{2\times\beta} \times S \times \sqrt{\frac{\pi}{A}} \qquad \textbf{(Eq.4.6)}$$

where *P* is the maximum indentation force (N), *A* the projected contact area (mm²), *E* the elastic modulus (GPa), *S* the measured stiffness defined as dP/dh and *β* a shape constant of 1.034 for a Berkovich indenter **[79]**.

Because the load applied and the displacement of the indenter in the sample are constantly measured, it is possible to plot the *P-h* curve, or penetration depth curve, of the indentation in order to observe mechanical parameter such as the elastic and plastic deformations or the unloading stiffness (see **Fig.4.25**).

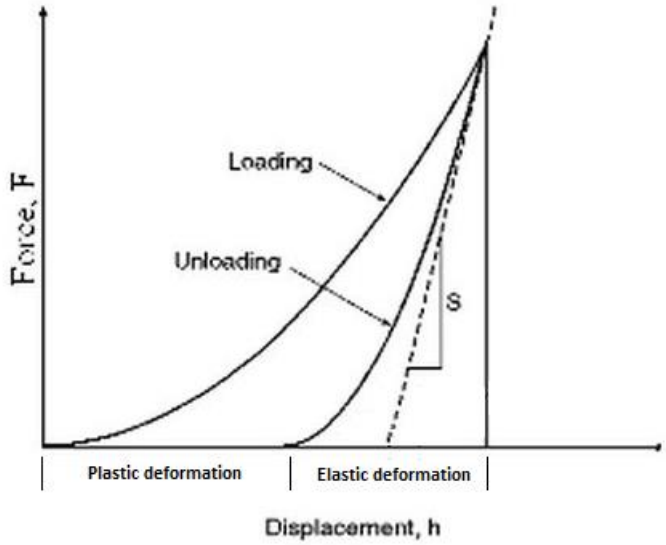

Fig.4.25 *Penetration depth curve, where S represents the unloading stiffness* **[80]**.

It must be taken into consideration that, while performing a nanoindentation on a sample surface, the plastic deformation induced will modify the material properties in a zone of a size close to 10 times the maximum penetration depth, while the elastic zone will be near 20 times the maximum displacement into surface. Taking this point in consideration, each nanoindentation realized must be spaced with the other in order avoid any overlapping effect.

A homogeneous array of 16 imprints (4 by 4) was performed by using the Berkovich indenter. This array was performed at 2000 nm of maximum displacement into surface (or until reaching the maximum applied load 650 mN) by using a nanoindenter XP (MTS) equipped with a continuous stiffness measurement module, the later allowing a dynamic determination of the mechanical properties during the indentation process. A constant distance around 50 µm was held between each imprint in order to avoid any overlapping effect. Along the indentation process, the indentation strain rate was held at 0.05 s^{-1}.

5. Results and discussions

In this section will be exposed the results obtained during this entire Master's thesis. They will be analyzed in order to conclude on the various parameters to use for the process and the effects on the materials.

5.1. Maximization of the mechanical properties

In order to achieve a sample with the highest density possible as well as with enhanced mechanical properties in term of hardness, fracture toughness and elastic modulus, a wide amount of ceramic pastes and printing temperatures have been studied so as to define the optimum condition. Afterwards, diverse sizes of the injection head's diameter have been tested due to the friction between the ceramic pastes and the printing nozzle which is a key parameter to take into consideration. Then, a test consisting in studying the humidity of the sample and the result on the mechanical properties was carried out, as well as a study of the sample's geometry evolution before sinterization. Finally, shrinkage of the sample has been measured for diverse printing conditions in order to understand the behavior of the material during the sintering process.

5.1.1. Paste composition and printing temperatures

Different compositions for the ceramic pastes (from 25 wt.% to 75 wt.%) have been used to print samples at different temperatures (from room temperature "RT" to 50°C). Their densities were then obtained and analyzed in order to define the optimum printing parameters to maximize the properties of the final material. The results of the densities obtained are represented in the **Fig.5.1** and show the following tendencies:

- The density of the final material increases up to a certain point close to the maximum ceramic charge concentration printable (70 wt.% for 30°C), and then decreases.
- For higher temperatures, the maximum amount of ceramic charge that can be used to print increases, but the lower limit in ceramic concentration also increases. As a matter of fact, for higher concentrations, the paste gets too viscous and cannot be extruded, while for lower concentrations, the structure of the part obtained can hold the initial geometry and changes due to gravity.

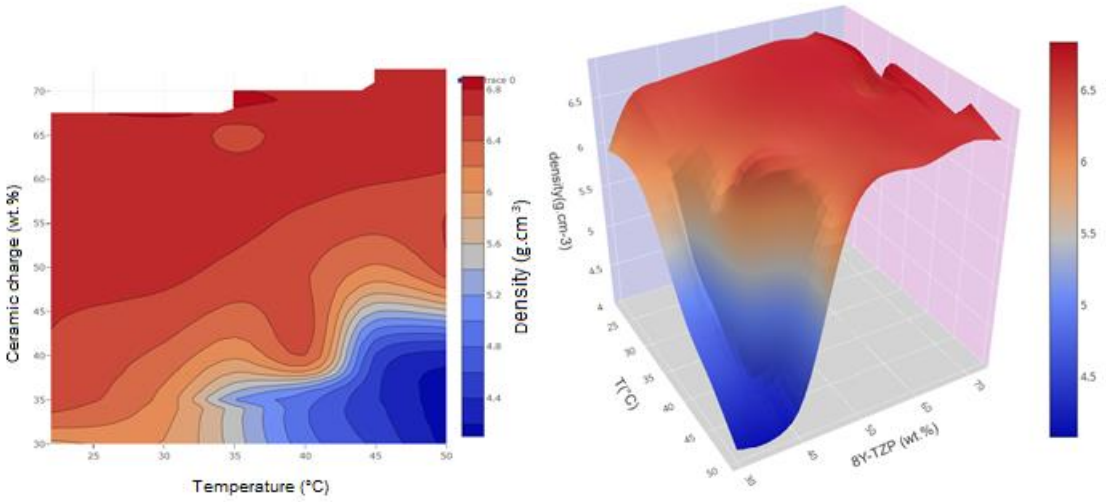

Fig.5.1 *Representation of the density in function of the paste composition and the printing temperature (graphic created with python, code available in* ***Annexes B.1*** and ***B.2****).*

The optimum properties obtained have been found for a ceramic charge of 67.5wt% and a printing temperature of 30°C. Therefore, these conditions will be used for the rest of this study. The mathematical method used to interconnect the results in the **Fig.5.1** was a bilinear interpolation method.

The maximum value of density found is 6.817 $g.cm^{-3}$ and was obtained for a composition of 67.5 wt.% of ceramic charge and a temperature of 30°C. Therefore, these conditions will be used for the rest of this investigation.

Compared to the theorical density of the *t*- and *c*-phases of zirconia, respectively 6.10 and 6.07 $g.cm^{-3}$ **[55]**, the values obtained are too high to be compared with them. This could be due to an error of calibration of the apparel used. For this reason, it will not be possible to calculate the exact relative density of the samples obtained. In order to do that, it would have been possible to use a helium pycnometer and calculate more precisely the density of the samples. Nevertheless, a density of 6.79 ± 0.06 $g.cm^{-3}$ was found for the samples created with CIP method. Therefore, it can be assumed that the robocasting method gives the ability to obtain parts with a relative density close to 100%, since the value of the CIP sample density, process allowing the obtention of a fully dense material, were measured with the same device and are close to the values obtained for the printed samples.

5.1.2. Injection head diameter

In order to perform the first step of maximization (see ***section 5.1.1***), a plastic tip with a diameter of 580 µm was used. Then, once the optimum composition and temperature found, different

injection heads were tested in order to print different samples for which the density was evaluated, as presented in **Fig.5.2**. The value of the injection head diameters tested were of 1540, 1360, 840, 610, 510, 410, 330 and 250 µm.

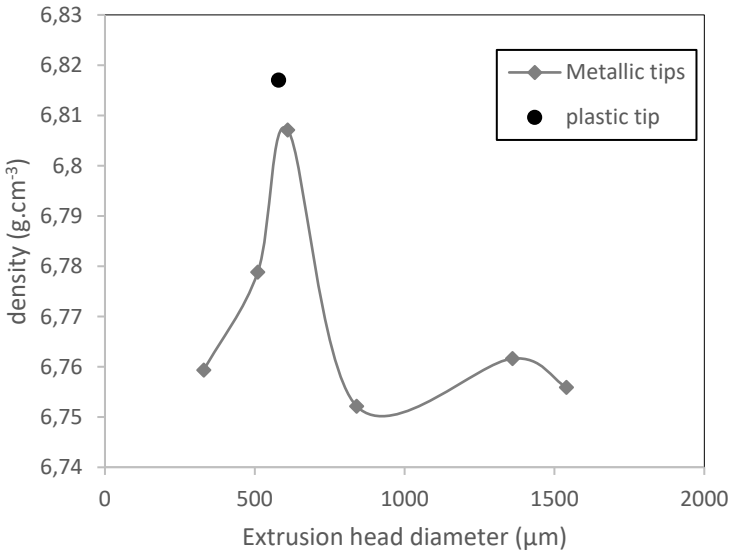

Fig.5.2 *Graphical representation of the density obtained in function of the extrusion head diameter.*

Fig.5.3 *Photography of the different metallic injection tips.*

Those results indicate that, firstly, the plastic tip (smoothflow tapered tip) shows better results than the metallic ones (precision stainless steel tip) shown in **Fig.5.3**. This was expected because the smoothflow tapered tip are designed to be used with particle-filled materials or any medium with high viscosity fluid, which is the case of the ceramic paste manufactured during this study (see ***Annex C.3***). The second observation that can be made is that, the optimum extrusion head diameter seems to be close to 600 µm, thus the best density obtained with the precision stainless steel tips was printed with

a diameter of 610 µm. In order to understand why this range of value for the diameter offers better results, it is necessary to look at the powder properties furnished by TOSOH.

Regarding the certificate of analysis of the ceramic powder used (see ***Annex A.2***), it can be seen that the crystalline size of the powder is of 230 Å. Nevertheless, it has to be taken in consideration that due to electrostatic charge, the particles of powder form agglomerates which therefore possess bigger sizes. In order to evaluate said size, an analysis was performed with a Mastersizer3000 on the powder of 8Y-TZP (by Ludmila Hodasova within the CIEFMA group). The medium results of this analysis are shown on **Fig.5.4**.

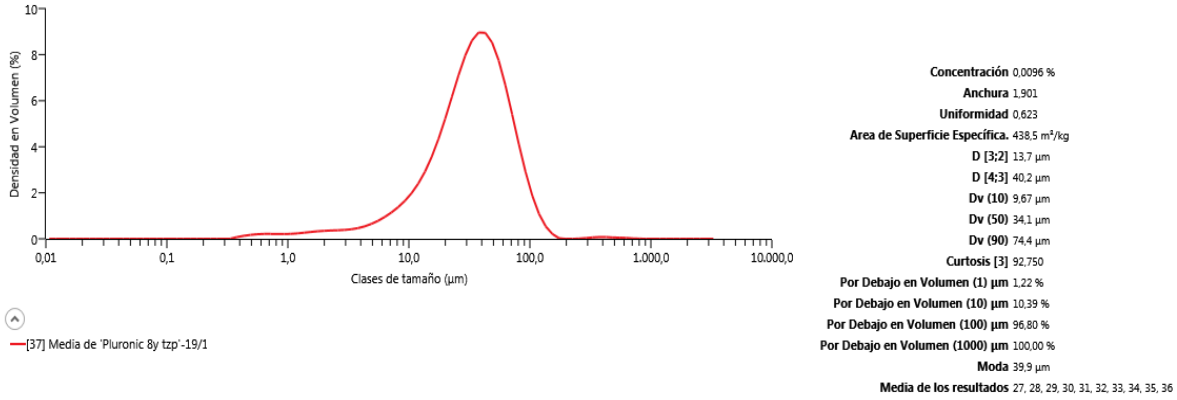

Fig.5.4 *Graphical representation of the medium volume repartition of the agglomerates and particles sizes.*

As it can be observed in **Fig.5.4**, the agglomerates present sizes that can go up to 200 µm, it explains why it was not possible to print with diameter of 250 µm or inferior as the paste cannot be extruded at all. It is then logical to assume that the maximum value of density will be reach for the thinnest diameter, which allows achieving thin layers and a better completion. It can also be considered that if diameter values of 330 µm and 510 µm give results lower than 610 µm, it is also due to the high content in ceramic powder of the paste used to print (67.5 wt.%) and the fact that the agglomerates can hinder the flow of material, inducing defects, and as a consequence a high amount of internal porosities which reduce the final density.

In conclusion, the tip that will be used for the rest of this investigation will be the smoothflow tapered tip with a diameter of 580 µm, which is the same as the one used to determine the optimum composition and temperature. In order to reach this conclusion, it has been considered that the evolution of the density obtained with the smoothflow tapered tips behaved the same way that the precision stainless steel tips and depended only on the size of the tip diameter.

In order to enable the use of a smaller diameter, it could be possible to separate the agglomerates and reduce the particle size with techniques such as ultrasounds. Indeed, it is feasible to reduce the size of the particles and to cause a delamination of the material thanks to sonification. It would be then possible to obtain particles of nanometric scale, and therefore to print with an extrusion head of smaller diameter. Furthermore, another important parameter during the deagglomerating process is the solvent and as a consequence the Zeta-potential of the materials used. The zeta-potential represents the potential difference between the dispersion medium and the stationary layer of fluid attached to a particle. A low zeta-potential will cause a flocculation of the colloids because the attractive force between particles will exceed the electrostatic repulsion around the particles. It would be then necessary to investigate this parameter for the materials used to manufacture the ceramic paste.

5.1.3. Influence of the relative humidity on the density

In order to reduce the quantity of porosity in the final sample and therefore increase the density, it is necessary to reduce the quantity of water inside the sample prior the sintering process. For this reason, a study of the evolution of the water evaporation in the sample has been performed via the use of a hygrometer in two different conditions. The first test was carried out in a dry atmosphere (with Relative Humidity (RH) inferior to 60%), while the second test was realized in presence of water and therefore in an environment with high RH (superior to 80%) (see **Fig.5.5**). Afterwards, a third test was then realized in order to obtain the total amount of water contained in the sample, by measuring the mass loss in a very dry atmosphere (RH inferior to 20%), shown in **Fig.5.5**.

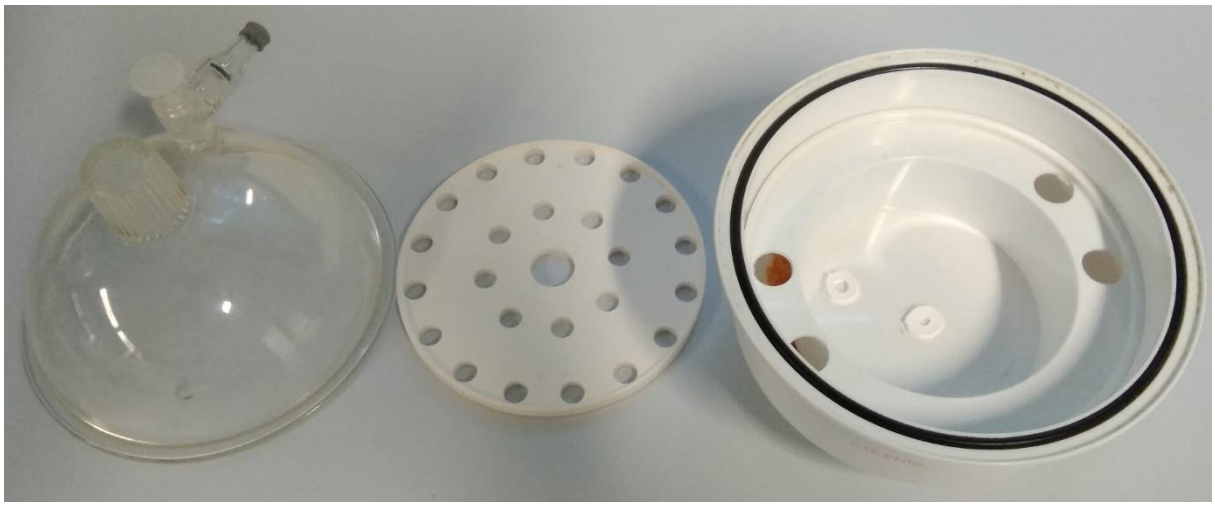

Fig.5.5 *Set up of the equipment used to realize the test on relative humidity.*

In **Figs. 5.6** and **5.7** the evolution of the relative humidity and relative mass loss during time are represented. In these graphs, density obtained for some samples as a function of their exposure time in the environment before performing the sintering process are annotated.

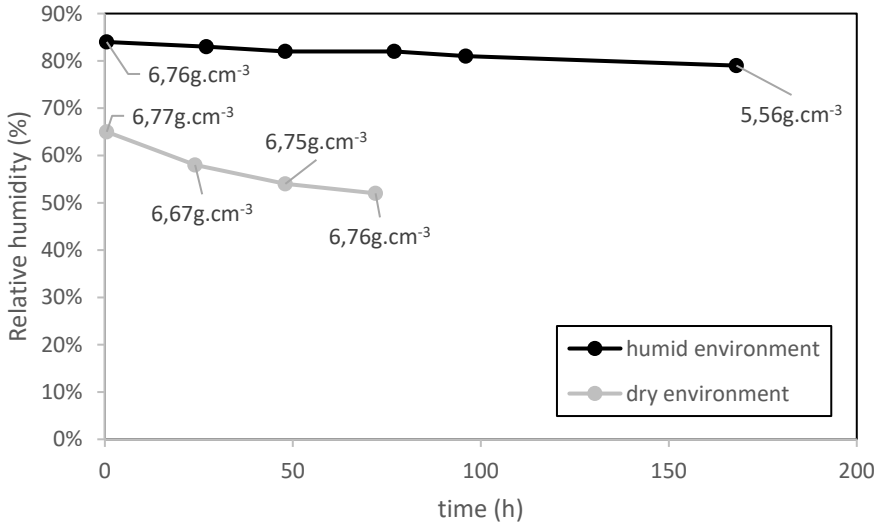

Fig.5.6 *Graphical representation of the relative humidity evolution vs. time.*

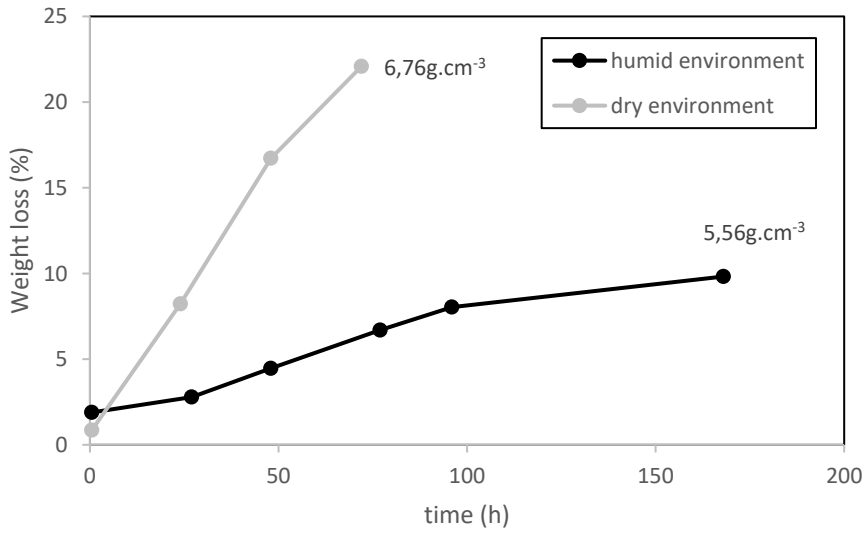

Fig.5.7 *Graphical representation of the weight loss vs. time.*

The results presented above are mixed for the density obtained in the dry environment (RH inferior to 60%). As a matter of fact, a clear evolution of the density cannot be observed during the time of the study which was certainly too short. Moreover, other parameters have to be taken into

consideration that can affect the density such as the temperature of printing that can vary of several degrees, or the presence of inhomogeneities in the paste.

Nevertheless, the test realized in humid environment (RH superior to 80%) shows a clear decrease of the density for a long time of exposure, from a density of 6.76 $g.cm^{-3}$ at a 0 time (just after printing) to 5.56 $g.cm^{-3}$ after 172h. However, the weight of the sample decreases with time, which proves the drop of the water content in the sample. Therefore, this reduction of the density is not related to an increase of water content in the material before sintering, but to a modification of the part structure which flows due to the high humidity. This aspect will be treated in the next section.

The last test was performed in order to assess the total amount of water inside the sample, in a way to ascertain the rest time of 5 days determined by Laura Cabezas in a previous study. Four samples with a tubular geometry were then placed in a dry atmosphere with a relative humidity inferior to 20%. The weights of these samples were measured after printing and at time intervals of 24h until the obtention of the final weights of the dry samples. Because the evaporation of the water in the samples depends on various parameters such as the ambient temperature, the surface contact with the air and therefore the internal diameter used to print the sample, the thickness of the sample or the amount of material printed, it was not possible to determine an exact value for the maximum quantity of water evaporable. The average value obtained on the four sample was 52 ± 17 %, which presents a too high deviation to enable a clear prevision of a precise time to wait before performing the sintering process. Nevertheless, it could be possible to fix a minimum percentage of evaporation required before sintering in order to ensure a proper maximization of the density. This value would be of 35% of the total amount of water contained in the sample.

For these four samples, the density obtained was of 6.80 $\pm$ 0.05 $g.cm^{-3}$, which completes proving that a time of post drying before the sintering treatment is required to obtain the maximum density.

Therefore, during a time of five days, the sample will be placed in a dry environment with a RH inferior to 60% in order to evacuate the water inside the sample and minimize the porosity. It could also be possible to place the samples in an atmosphere with RH inferior to 20% during a time of one day. Nevertheless, this last option could cause cracks on the material due to the realization of evaporation process too abruptly.

5.1.4. Influence of the geometry and the printing pattern

As it has been explained previously, two different geometries were printed, cylindric and tubular. Concerning the cylindric geometry, only one dimension was printed, with a diameter of 15mm, while for the tubular geometry, various dimensions were tested, depending on the internal diameter.

Indeed, while the external diameter stays the same as in the cylindrical geometry, seven different internal diameters were tested, from 5mm to 12mm. For internal diameter superior to 8mm, due to the internal stresses caused by the shrinkage of the material during the sintering treatment, the printed parts broke. Because the goal is to obtain the higher contact area between the electrodes and the electrolyte, it is interesting to use the higher internal diameter possible. Moreover, the higher the internal diameter, the lower is the amount of material used to manufactured the part.

It has been observed that the density is not influenced significantly by the geometry chosen. Indeed, the mean value obtained for the tubular geometry is of 6.80 ± 0.05 $g.cm^{-3}$ while the one obtained for the cylindric geometry is of 6.81 ± 0.03 $g.cm^{-3}$. A second step in this direction would have been to look if the variation of the inner diameter of the tubular geometry affects the density of the samples, but the low quantity of samples successfully printed does not allow the obtention of results. However, it can be assumed that the change of intern diameter will not affect the density of the material since the printing pattern stays the same.

The pattern used to print is another aspect that has to be taken in consideration in order to obtained the sample with the closest final aspect to the initial CAD model. For both the cylindric and the tubular geometries were tested two printing patterns, rectilinear and concentric. It can be seen in **Fig.5.8** the final patterns choose for this Master's thesis. Indeed, it has been seen that:

- For the cylindric geometry, the rectilinear pattern gave better results than the concentric ones from the point of view of the aspect, with the condition of realizing at least 2 perimeters around the structure in order to avoid detachment of the extruded ceramic paste on the border.
- Concerning the tubular geometry, the concentric pattern fitted much more with the geometry printed and allowed to avoid the detachment of the extruded ceramic paste on both borders (intern and extern) of the structure.

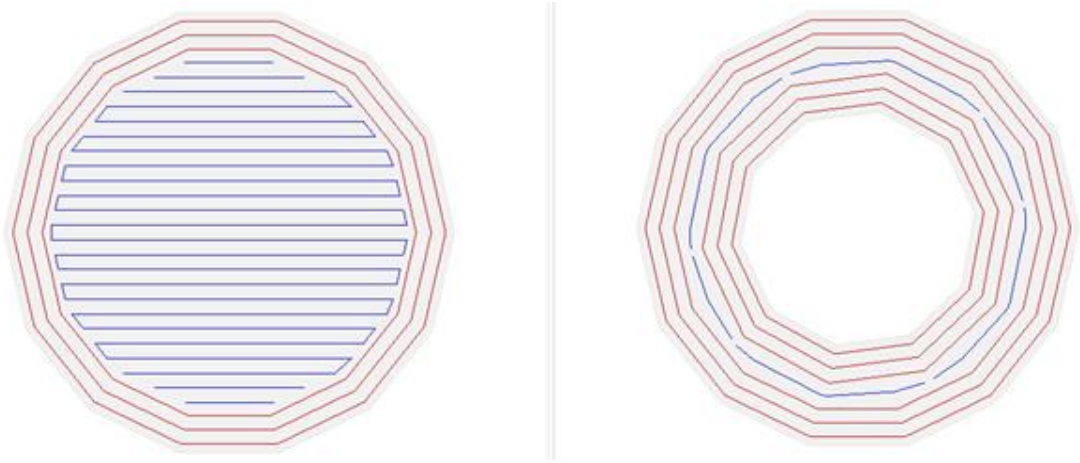

Fig.5.8 *Pattern used to print the cylindric (left hand side) and tubular (right hand side) samples.*

5.1.5. Influence of the water content on the paste flow and the change in the geometry

Once a sample printed, it is possible to observe a flowing of the paste, and thus a modification of the initial geometry. The collapse of the structure is due to the composition of the paste that contain hydrogel made of 75 wt.% of water and 25 wt.% of pluronic. In order to analyze this phenomenon, diverse time-laps were realized on samples with the use of a VEHO discovery VMSQ-004 Deluxe and the software SkyStudio Pro.

Fig.5.9 *Schematic representation of the sample deformation during time*

As schematized on **Fig.5.9**, the structure can change significantly between the printing and the sintering treatment. So as to anticipate the total deformation on the sample, a motion tracking was realized with the software Adobe After Effect. This method allows the creation of a "video object" that will follow a given point during the time of the video and allow the acquisition of its path. It is preferable to follow a perceptible point from a point of view of the pixel values RGB, therefore were used two colorants, blue and red, in order to mark the printed sample.

Motion tracking was performed on three different points on the sample, one with each colorant and a third on the corner of the sample while the time-lap was conducted by taking a photo every 30s during a time of 5663s (see **Fig.5.10**). Once the results obtained, and knowing the time between each displacement point (see **Fig.5.11**), the distance between them was measured with the

software imageJ and finally it was possible to obtain average values of the flowing speeds of the material at different times. These values were plotted in **Fig.5.12** and each curve approximated with a power law of the type of **Eq.5.1**.

$$y = a \times x^{-b} \quad \textbf{(Eq.5.1)}$$

Where *a* and *b* are positive real numbers, *y* the flowing speed in $mm.s^{-1}$ and *x* the time in s.

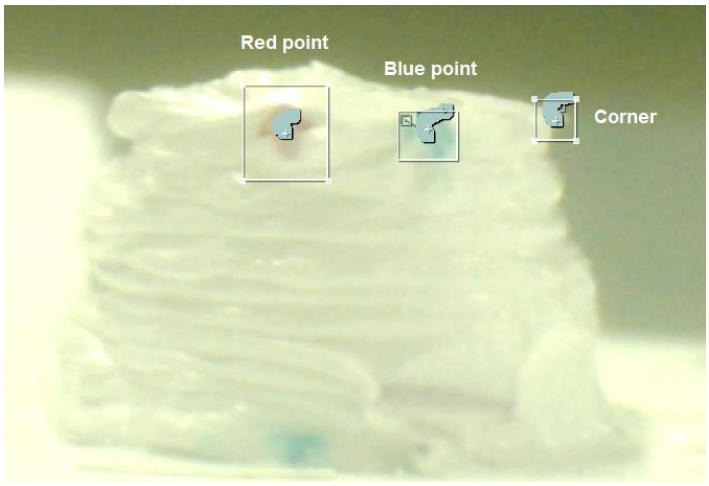

Fig.5.10 *Screenshot of the time-laps at the end of the motion tracking process.*

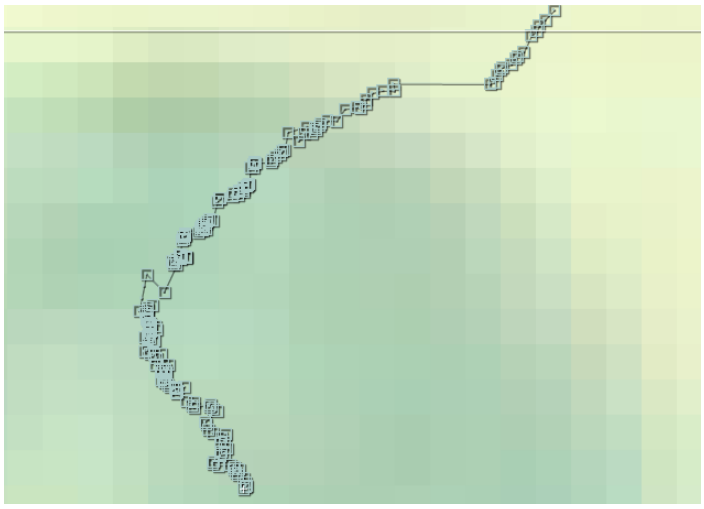

Fig.5.11 *Screenshot of the time-laps at the end of the motion tracking process with a zoom on the blue point.*

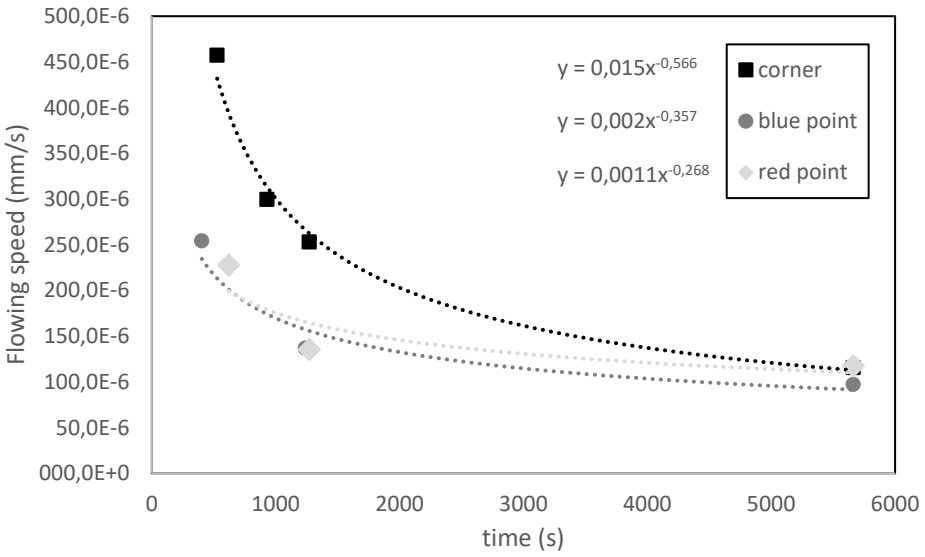

Fig.5.12 *Graphical representation of the flow rate evolution during time for the three points evaluated.*

The results of these tests show a clear tendency of the flowing velocity to decrease rapidly with time before stabilizing for all three points, thus it could be reasonable to approximate these evolutions with a power mathematic law. It can also be noted that the deformation rate of the corner is twice the one of the other points. This last aspect is due to the imperfection of the sample on this point where the material was more inclined to deform than on the other points. For this reason, only the evolution on the red and blue points should be considered to calculated an average value of the coefficients *a* and *b* (see **Eq.5.1**), which would have respectively a value of 0.0014 ± 0.0006 and 0.31 ± 0.06.

This test shows that, due to the imperfections of the printed sample, the deformation and deformation speed can vary regarding the zone observed. It also proves that the major part of the deformation is observed shortly after the printing process as well as during the process itself. A solution to this problem could be to create at the same time, with a second extrusion head or with a dropper, a support structure around the material of the printed part in order to sustain its geometry. A suitable material for this application could be the Pluronic F-127® because of its gelation property. Therefore, printing at ambient temperature and with a paste at higher temperature, the polymer will pass the gelation point and block the flow of the ceramic past. This material would be removed during the process of sintering.

5.2. Shrinkage

Once the sample printed, after a five-days period, the sintering treatment is performed in order to obtain the final dense object. During this thermal treatment, the water evaporates while the pluronic is decomposed into gaseous products. Once high temperatures are reached (1450°C), atoms of zirconia diffuse across the boundaries of the particles and bind them together. At the end of the process, the material forms a solid and dense part. Due to this densification, the overall structure undergoes a reduction of volume also called shrinkage. This variation in the volume of the piece has been measured for different compositions and both geometries. The importance of knowing the behavior of the material during the sintering treatment is critical to obtain a specific final geometry, and thus prepare the adequate model for the green part.

Concerning the cylindrical geometry, the initial dimensions used were a diameter of 1.5 cm for a height of 1 cm. The dimensions of the sintering part as well as the shrinkage values were measured for different compositions of ceramic charge at 30°C as well as for different temperatures for a ceramic charge of 67.5 wt.% in order to observe the influence of both temperature and composition. Were also compared the values obtained for the samples exposed to the humid environment (RH superior to 80%) to those exposed to a dryer environment (RH inferior to 60%).

The results obtain show a clear correlation between the composition of the paste used to print and the volume reduction. Indeed, for a higher composition in hydrogel, the shrinkage increases, which is due to the quantity of products that evaporate or decomposed under the action of the temperature. The evolution of the shrinkage can be found in the **Fig.5.13**.

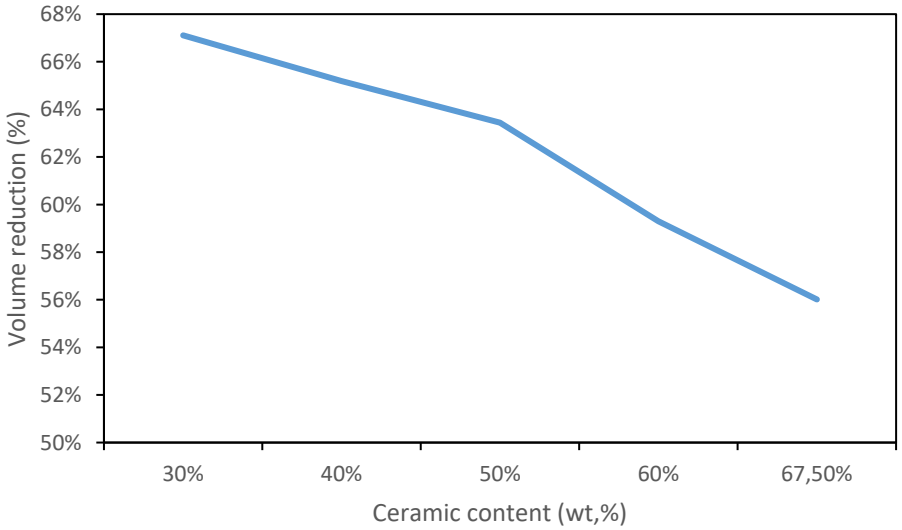

Fig.5.13 *Graphical representation of the volume reduction depending on the powder charge used during the paste preparation (for a printing temperature of 30°C).*

The tendency that can be observed for the different printing temperatures gives a less clear pattern of evolution (see **Fig.5.14**). Even though there seems to be a decrease in the percentage of volume reduction for higher printing temperature, this decrease is less visible than the one observed with the variation of ceramic content.

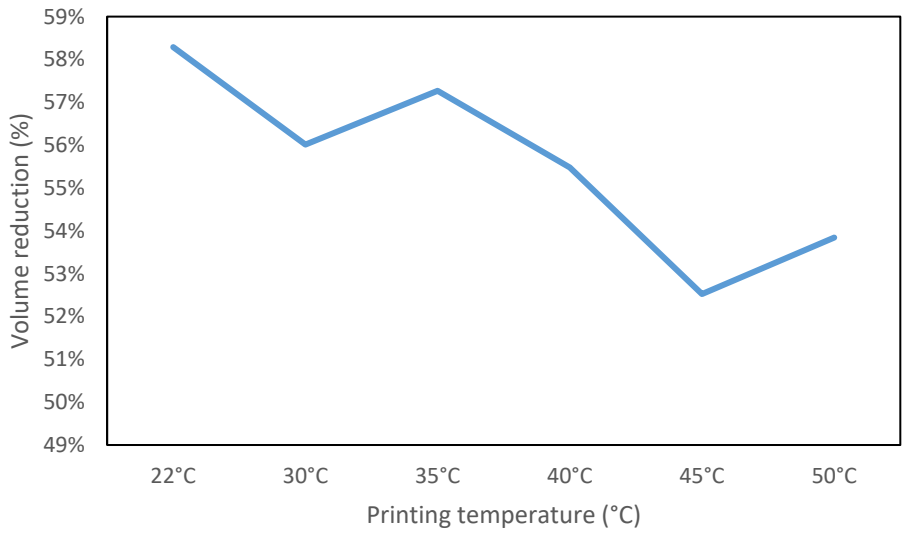

Fig.5.14 *Graphical representation of the volume reduction depending on the printing temperature used (for a composition in ceramic powder of 67.5 wt.%).*

The last comparison was made between the sample exposed to a dry environment (RH inferior to 60%) and the one exposed to a humid atmosphere (RH superior to 80%). It has to be taken into consideration that the sample exposed to a high RH flowed more, and therefore the initial diameter of the cylindrical samples were higher than 15mm. These lasts were measured close to 17mm. The results are shown in the **Fig.5.15** and clearly exhibit an augmentation of the shrinkage for the sample exposed to the high RH atmosphere. This was expected due to the higher content of water in it.

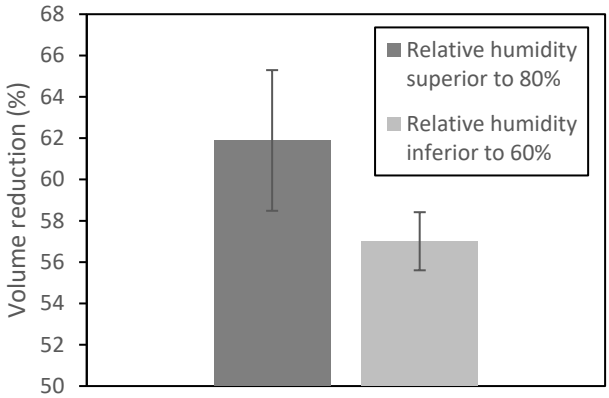

Fig.5.15 *Graphical representation of the volume reduction difference between samples exposed to high relative humidity and sample exposed to a dry atmosphere.*

Those results show that the shrinkage of the part during the sintering treatment is inherently linked to the quantity of water it contained, and therefore, to the quantity of hydrogel used during the making of the ceramic paste. They also show that for higher printing temperatures, the volume contraction decreases, certainly due to the higher amount of water evaporated before the sintering process, during the printing and the rest time of the part.

5.3. XRD spectrums

X-Ray diffraction (XRD) was realized on the powder used during the whole investigation as well as on a sample realized with CIP and one realized with 3D-printing in order to see if the processes could affect the phase in presence in the material. There spectrums are shown in the **Fig.5.16**. Are also identified the different pics of refraction of the cubic phase with the directions of their planes of reflection annotated (h,k,l).

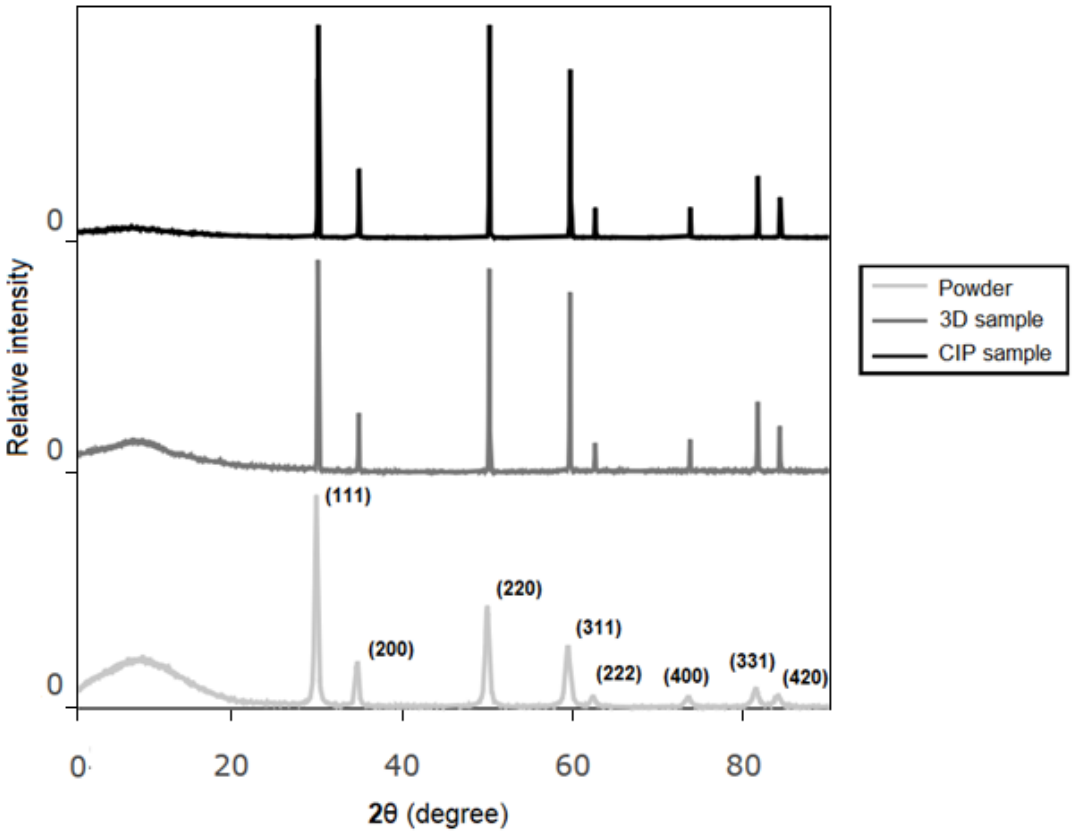

Fig.5.16 *Graphical representation of the diffraction spectrum relative of the 8Y-TZP powder, the sample manufactured with CIP and the sample created with robocasting method.* **[81, 82, 83]**

It can be seen that each pic presents on the powder spectrum is also presents for both of the samples, which means that none of the phases initially present were removed during the sintering treatment and that the composition of phases had not significantly changed. The differences in the dispersion between the spectrum of powder and the others is due to a difference between the surface rugosity of the sample surfaces. Indeed, the powder, due to its state couldn't be polished, and therefore possessed a topography with an order of 100 µm (particle and agglomerate sizes) while the other samples were polished up to 3 µm. The irregularities in the sample topography are responsible for the divergence of the incidence angles and therefore the larger dispersion of the pics for the powder spectrum.

Concerning the different pics, it can be noted that only the cubic phase is present, as it is possible to observe the characteristic pics of this phase only (see **Fig.5.16**). The pics corresponding to the monoclinic and tetragonal phases cannot be observed on these spectrums **[81, 84, 85, 86]**. Therefore, the results show that the main phase in presence in the material is the cubic phase, which is normal considering the quantity of yttria added to stabilized the metastable phases.

5.4. External porosity

In order to evaluate the external porosity of the material, samples manufactured with CIP (sample CIP) and 3D-printing for both geometries, cylindric (sample C) and tubular (sample T) were analyzed with FESEM. For each sample were realized 5 pictures in order to obtain the average density of porosity at nanometric and micrometric scales. The measurements were realized with the software imageJ. The results obtained for all geometries can be found in **table.5.1**.

Table.5.1 *Results of the image analysis on the three samples CIP, C and T.*

Samples	Nano scale		Micro scale		Density ($g.cm^{-3}$)
	Average size (μm^2)	*% area covered*	*Average size (μm^2)*	*% area covered*	
CIP	0.044±0.019	0.79±0.84	4.03±16.63	0.054±0.072	6.79
C	0.16±0.10	4.81±1.68	32.13±11.78	7.75±2.64	6.80
T	0.12±0.14	2.84±1.97	27.98±156.27	1.61±1.86	6.74

It can first be observed that the amount of porosity, characterized by the percentage of area occupied by the pores, is higher for the sample C and T than for sample CIP. It can also be seen that the average size for both the nano and the micro-scales pores are higher on the surface of C and of T samples than on the CIP sample.

These two points can be explained by the initial composition of the material before the sintering process. Indeed, in order to manufactured the sample CIP, was only used ceramic powder, whereas the sample C and T were printed and therefore composed of 67,5wt% of ceramic powder as well as 32,5wt% of hydrogel. The presence of this hydrogel composed of 75wt% of distilled water and 25wt% of pluronic F-127® is responsible for the apparition of the pores in the material, because during the sintering process, water will evaporate while pluronic F-127® will be decomposed in smaller molecules and will then adopted a gaseous state too. These gases will create channels in the ceramic material still malleable in order to escape the structure. Those channels, are visible under the appearance of pores on the surface of the material (see **Fig.5.17**).

Moreover, due to relative humidity and other contact with the 8Y-TZP powder, the material will inevitably contain water or other undesirables' impurities. Therefore, the presence of pores on the final part will be inevitable even using the CIP manufacturing process, but can be reduced using a clean workspace and a drying system in order to avoid the contamination of the powder during the creation of the green part.

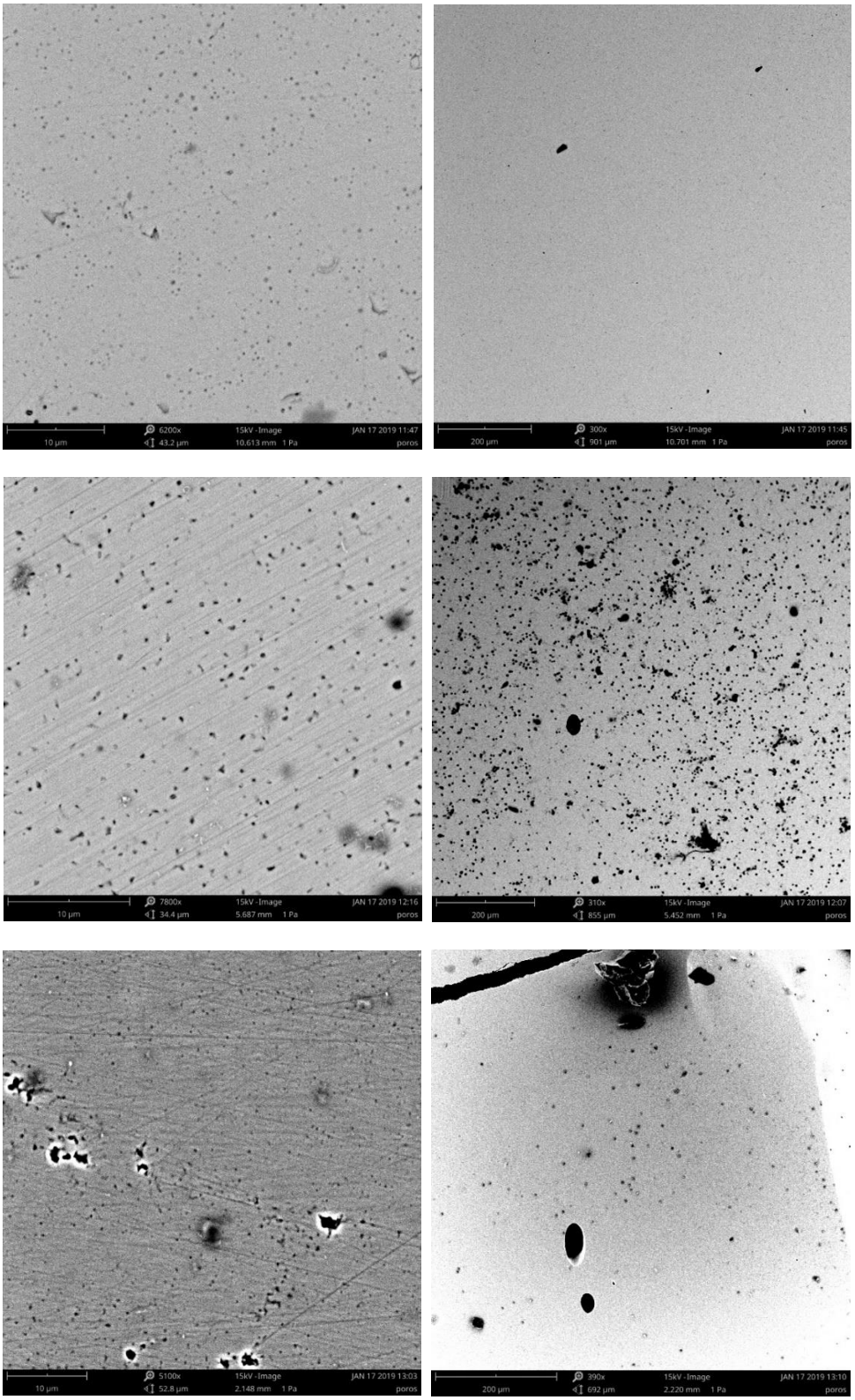

Fig.5.17 *Photography realized with FESEM (with a scale of 10 µm on the left and 200 µm on the right) on the sample CIP, C and T (from top to bottom).*

The FESEM pictures were also used to identify the different defects present in the surfaces of the samples. Indeed, it can be seen the presence of cracks in the surface of both printed samples (see **Fig.5.18**). It can also be observed space of the scale order of 100 µm (see **Fig.5.18**). Those defects can be considered as printing defects. Indeed, the apparition of cracks on the sample surface can be due to the presence of water in the material and its evaporation during the rest time prior sintering. During the water evaporation, the ceramic paste will undergo contractions which will sometimes generate cracks. It can also be noted that, due to the brittleness of the sintered material, the polishing process will also be responsible for the apparition of cracks on the samples surfaces as well as the propagation of the existing ones. Concerning the gaps in the structure, those can be produced by irregularities during the AM process. The inhomogeneities inside the ceramic paste, due to various agglomerate sizes or unfinished mixing of the diverse components, can modified the extrusion velocity and therefore caused inequality of the layer sizes. It can also be noted that the robocasting machine used presented some defects and therefore induced changes in the final geometries obtained (due to inequalities of the calibration for the movement in the *X*- and *Y*-axis as well as some irregularities in the *Z*-axis movements). These imperfections due to the printing process could be responsible for the presence of gap in the structure and could be corrected with the use of a powder with smaller particle size (see ***section 5.1.2***) in order to obtain a paste with less inhomogeneities and with the realization of a better calibration of the machine.

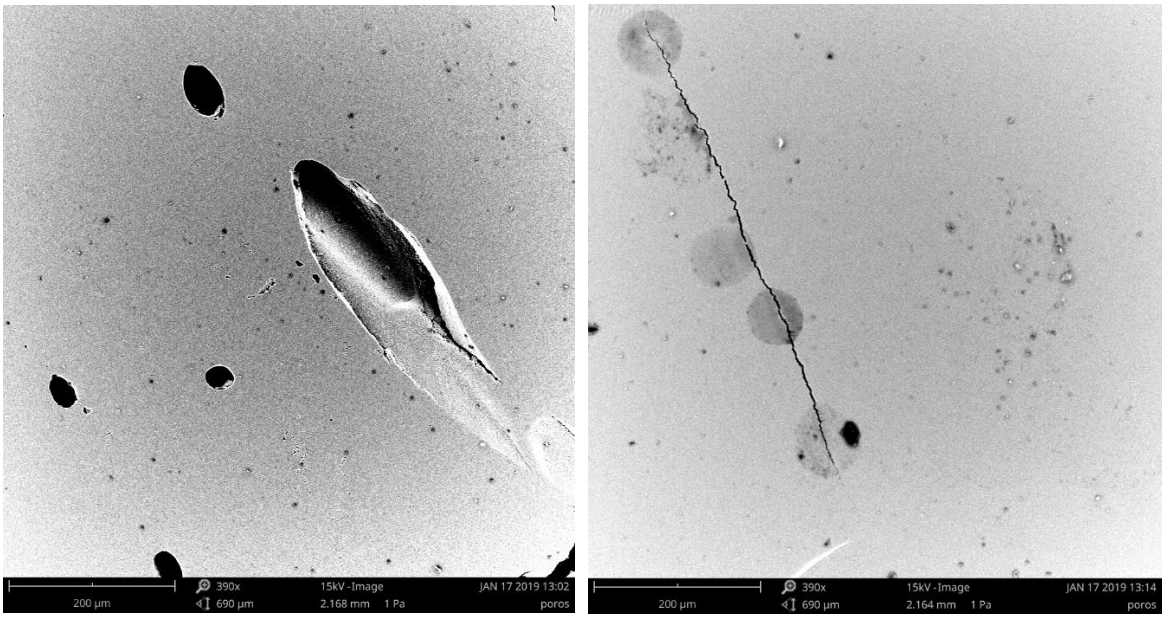

Fig.5.18 *Photography realized with FESEM of the sample T (scale 200 µm) showing a gap in the structure (left) and a crack (right).*

It can be realized a last conclusion of these results by comparing the densities with the values obtained for the percentage of area covered by external porosity. Indeed, the densities of the three samples are close while the percentages of area covered are higher for the printed

samples than for the sample manufactured with CIP (see **Table.5.1**). This absence of correlation shows that the porosity of the samples is not interconnected, and therefore, does not influence the value of density obtained with the Archimedes' method (see ***section.4.6.1***). Nevertheless, it is possible to assumed that it exists a quantity of internal porosity higher for the printed samples which is not taken in consideration during the measurements realized in this Master's thesis. Therefore, the real values of density of the printed material should be lower than the one obtained in the ***section.5***.

5.5. Grain size

In order to analyzed the structure of the material, was realized a thermal attack on the sintered material in order to enhance the grain growth of the phases in presence and therefore make them visible. This thermal attack consisted in a thermal treatment of 6h (see **Fig.5.19**) where the material was heated at 1200°C during two hours.

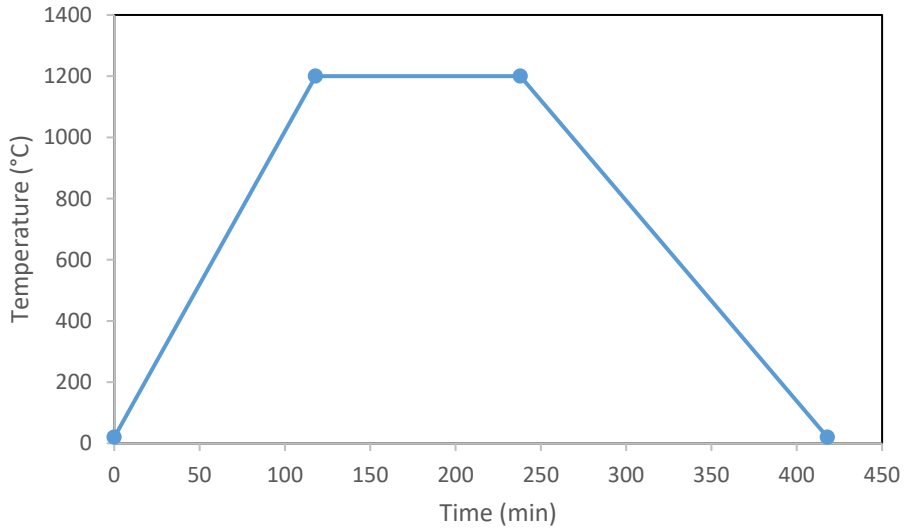

Fig.5.19 *Graphic representation of the thermal attack treatment realized during this investigation.*

Once this treatment realized, the sample surface was analyzed with FESEM (see **Fig.5.20**) and were measured the average area of the grain with the software imageJ. The repartition of the grain sizes realized with two pictures on 130 grains can be observed in the histogram **Fig.5.21**.

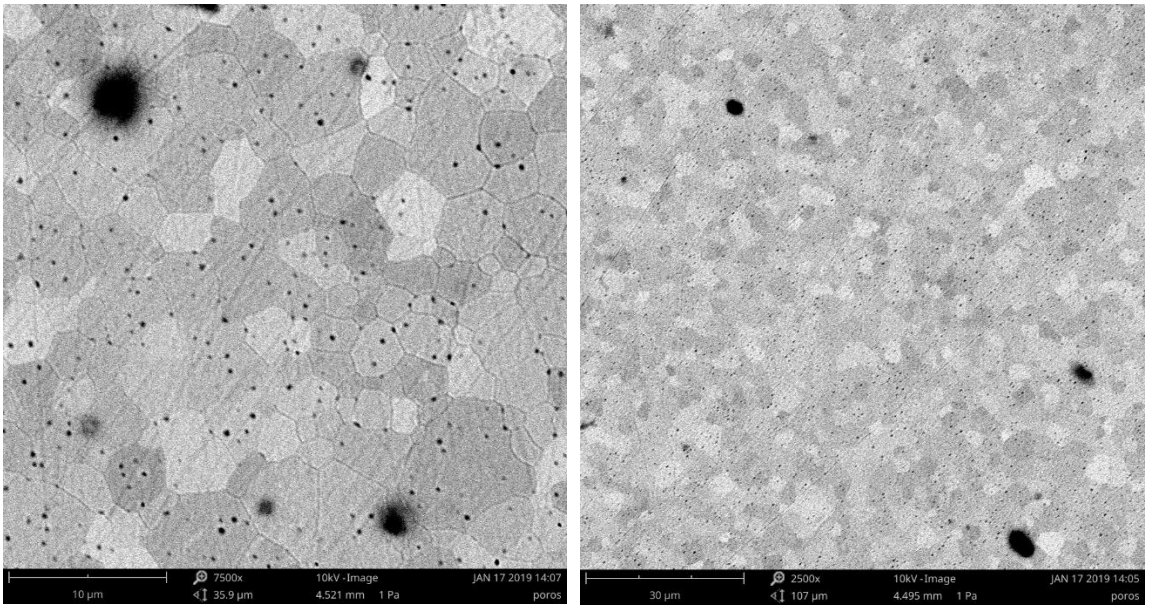

Fig.5.20 *Photography realized with FESEM of the sample after thermal attack treatment (scale of 10 µm and 30 µm).*

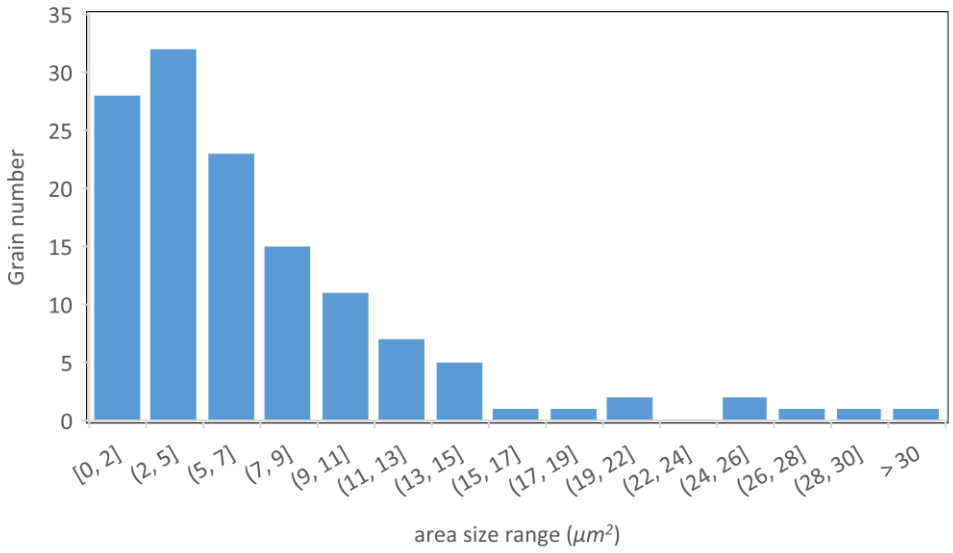

Fig.5.21 *Graphic representation of the quantity of grain size according to their area size for 130 grain analyzed.*

It can be measured that the average area of the grain is of 3.07 µm^2 while the maximum and minimum size observed are respectively of 49.42 µm^2 and 0.28 µm^2.

Comparing the results obtained with the literature available in internet, it can be seen, for example in Ref. **[86]** that the average grain size obtained for 8YSZ for a sintering treatment of 1580°C is of 5133 ± 204 nm. In comparison with the average result obtain in this Master's thesis, considering

that the grain form can be approximated as circular, the average size of the grain would be of 1997 nm. It can then be observed that the grain size obtained for a sintering temperature of 1450°C is inferior to the one obtained for a sintering temperature of 1580°C.

5.6. Vickers hardness and fracture toughness

In order to characterize the mechanical properties of the different samples obtained, Vickers hardness tests were realized on the sample obtained with CIP (sample CIP, which results will be used as a reference for the other samples) and for both geometries printed, cylindrical (samples C1 and C2) and tubular (samples T5, with an intern diameter of 5 mm, and T8, with an intern diameter of 8 mm). Then, the hardness (*H*) of these samples was obtained as well as their fracture toughness (K_{IC}) by observing the indentations realized with an optical microscope and using the software imageJ (see the methods in **section 4.7.1**). The diverse indentations were realized with four different forces: 0.1, 0.5, 5 and 10 kgf on each sample. The results obtained are shown in the **Tables 5.2** and **5.3**. For each test 5 indentations were realized in order to ensure the reliability of the results. The value of elastic modulus taken to calculate the fracture toughness was 210 GPa **[87]**.

It can first be noted that it was not possible to realize an adequate Vickers indentation with an indentation load of 10 kgf for both tubular samples or with an indentation load of 5 kgf for the tubular sample with an intern diameter of 8mm. As it can be seen in **Fig.5.22**, the geometry and the too high applied load caused the structure to break. This phenomenon can be related to the thinness of the structure, which cause a too high propagation of the cracks created and defects already present.

As it could be expected from the closest values of density found for the samples manufactured with CIP and the ones manufactured with robocasting method for the optimum condition (see **section 5.1.1**), the value of hardness found are close. Nevertheless, it can be observed that the values obtained with an applied load of 10 and 5 kgf present the tendency inverse than the ones obtained with an applied load of 0.5 and 0.1 kgf. Indeed, on average, the value of hardness of the printed samples compared to the sample manufactured with CIP are inferior of 0.9 GPa for an applied load of 10 kgf and 5 kgf, while they are superior of 0.4 and 1.1 GPa for an applied load of 0.5 and 0.1 kgf respectively. Those results could indicate a higher hardness of the printed samples than the one manufactured with CIP at a low scale, but at a bigger scale, the defects present in the structure of the printed samples reduce the hardness value obtained.

Moreover, it can be observed that the standard variations of the printed samples hardness values are higher than the ones from the CIP sample. This can be related to the irregularities of the structure material due to the spaces between the layers and therefore, to the obtention of different hardness of the material regarding the zone tested.

Considering the results in literature, it can be found that for content in yttria between 1 and 3 mol% used to stabilize zirconia with high density, the hardness varies from 9 to 13.6 Gpa **[87]**. Zirconia with high density stabilized with 5.5 mol.% of ceria and content between 1.5 to 4 mol.% of yttria show a hardness comprise between 8.9 to 11.5 Gpa **[88]**. In the Ref. **[56]**, various values of hardness can be found, from 8.4 to 9.4 GPa depending on the temperature of sintering (respectively from 1400°C to 1700°C). It can be said that the values obtained in this Master's thesis are high respecting to the expected value for 8 mol.% yttria stabilized zirconia.

Table.5.2 *Value of the samples hardness (GPa) regarding the process and the geometry chosen to manufactured them.*

	Indentation force (kgf)				
	sample	*HV10*	*HV5*	*HV0.5*	*HV0.1*
Hardness (GPa)	*CIP*	11.76 ± 0.38	11.81 ± 0.21	11.75 ± 0.24	12.04 ± 0.36
	C1	10.4 ± 1.3	11.25 ± 0.24	10.46 ± 0.41	12.0 ± 1.1
	C2	11.39 ± 0.10	11.40 ± 0.27	11.95 ± 0.36	12.75 ± 0.36
	T5	/	10.01 ± 1.25	12.47 ± 0.49	14.57 ± 1.18
	T8	/	/	13.59 ± 0.79	13.38 ± 0.98

Regarding the fracture toughness of the materials obtained, the results obtained can be found in the **Table.5.3**. Will not be considered the results obtained with the Vickers indentation realized with 0.1 kgf, because of their to high standard deviations. Moreover, the cracks formed with an indentation force of 0.1 kgf were too small to be observed properly. It was not possible either to obtain adequate values for some other applied loads due to the crack formed during the indentation (see **Fig.5.23**). Therefore, the values that will not be considered appear in red in **Table.5.3**.

The results of K_{IC} obtained show that the sample obtained with robocasting possess a fracture toughness equal or higher than the sample manufactured with CIP. It is difficult to conclude on anything because of the form of the created cracks and the difficulty to obtain reliable results. Nevertheless, it is possible to observe a similar tendency than for the hardness results. For an indentation load of 10 kgf, the values of K_{IC} are similar for all the samples studied, while for lower indentation load, the values obtained for the samples manufactured with robocasting technique seem to be higher than the ones obtained for the sample manufactured with CIP. This phenomenon could also be due to a higher mechanical resistance of the printed material at low scale than the one

manufacture with CIP, but because more defects are present in the structure, the values of K_{IC} are lower at larger scale.

In order to compare the values obtained with the literature, two studies have been selected. In the first article **[86]**, is evaluated with the Single-Edge V-Notched Beam (SEVNB) method the fracture toughness of 8Y-TZP sintered at 1580°C. The sintering temperature being higher, the grain size, of 5133 ± 204 nm, will also be higher than the one of the materials in this study. Therefore, it is logical that the fracture toughness value, of 1.6 ± 0.05 Mpa.$m^{-0.5}$ found in this first article are lower than the ones obtain in the present study. In the second article **[89]**, fracture toughness of yttria-stabilized cubic zirconia (8Y-CSZ) doped with 0.15, 0.7, 2 and 5 wt.% of pure silica is evaluated by Vickers indentation HV10. The sample were sintered at a temperature of 1400°C with a step at 1200°C. It is demonstrated in this investigation that the fracture toughness of the sample increase from 1.71 Mpa.$m^{-0.5}$ to 1.77 Mpa.$m^{-0.5}$ while the silicate content increases. Is also said that the theorical value for the fracture toughness of undoped 8Y-CSZ is comprised between 1.3-2.2 Mpa.$m^{-0.5}$. Therefore, the value of fracture toughness obtained in this Master's thesis are higher than the one that could be expected, especially those obtained for indentation loads inferior to 10 kgf.

Table.5.3 *Value of the samples fracture toughness (MPa.$m^{-0.5}$) regarding the process used to manufactured them.*

K_{IC} (*MPa.$m^{-0.5}$*)	**Indentation force (kgf)**				
	sample	*HV10*	*HV5*	*HV0.5*	*HV0.1*
	CIP	2.4 ± 0.55	2.37 ± 0.2	4.13 ± 0.18	10.9 ± 5
	C1	2.42 ± 1.75	2.9 ± 0.24	4.09 ± 0.63	9.5 ± 8.6
	C2	2.37 ± 0.73	4.36 ± 0.62	9.47 ± 3.16	/
	T5	/	2.53 ± 4.45	6.47 ± 0.91	14.77 ± 7.8
	T8	/	/	11.72 ± 3.71	19.13 ± 16.36

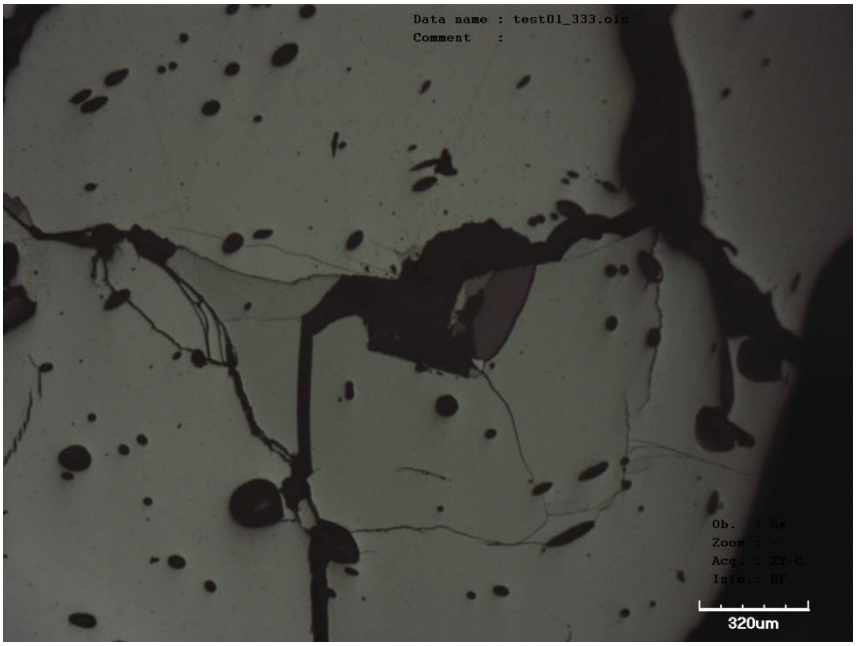

Fig.5.22 *Photography made with confocal microscope of an indentation Vickers realized with a force of 10 kgf on the tubular sample with intern diameter equal to 8 mm.*

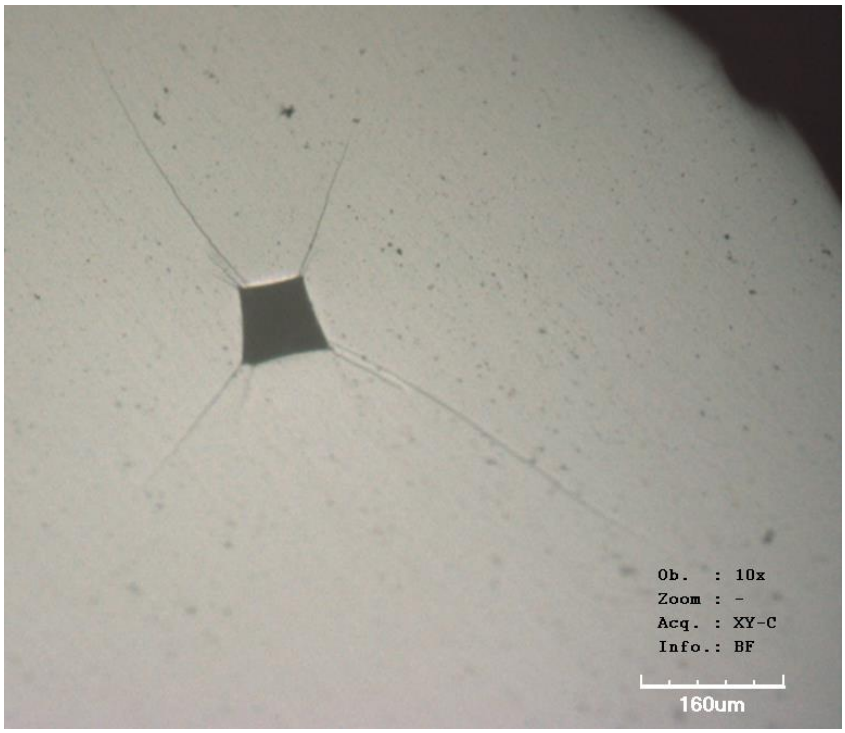

Fig.5.23 *Photography made with confocal microscope of an indentation Vickers realized with a force of 5 kgf on the tubular sample with intern diameter equal to 5 mm.*

5.7. Berkovitch indentation

Berkovich indentation were realized on four different samples. All of them were prepared with 67,5 wt.% of ceramic charge and printed at 30°C. The rest time of 5 days before sintering was realized in dry atmosphere (RH inferior to 60%) for the sample D1, D2 and D3 while it was realized in humid environment (RH superior to 80%) for the sample H. The value of hardness obtained are plot in **Fig.5.24**.

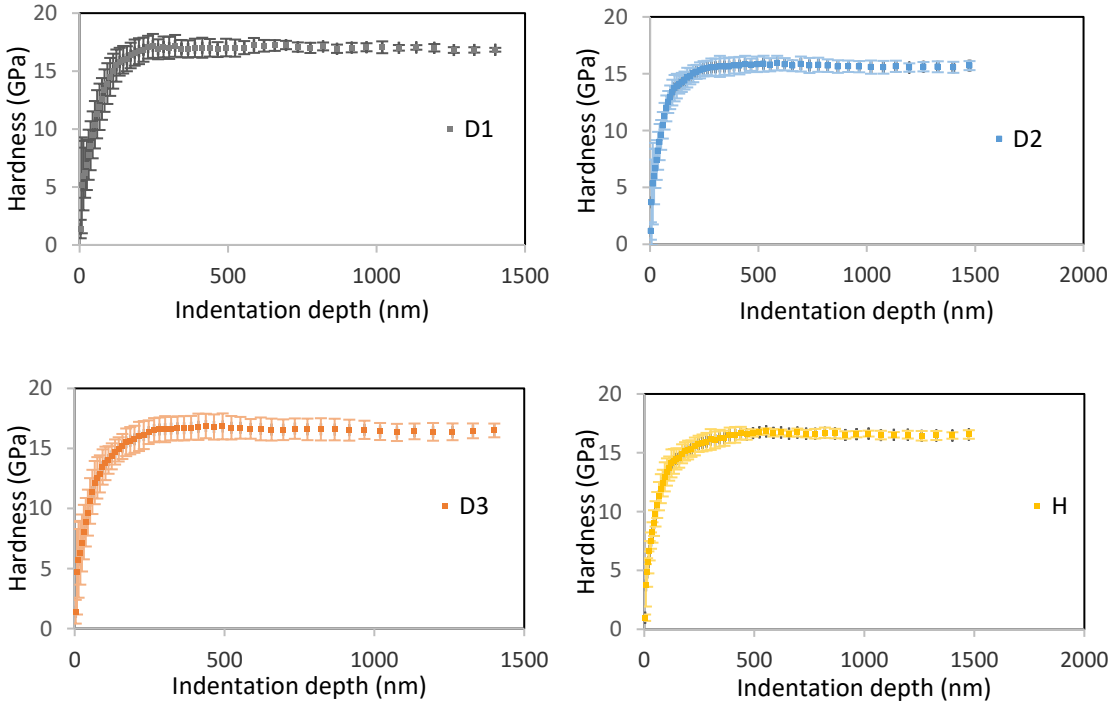

Fig.5.24 *Graphical representation of the Hardness (GPa) vs. the indentation depth (nm) for the four samples D1, D2, D3 and H.*

In the curves present in **Fig.5.24**, it can be appreciated two regions:

- The first one, zone where the mechanical parameters do not remain constants regarding the penetration depth. It is due to the scale effects, such as rugosity, superficial defects or tip defects, which affect the value of the mechanical parameter measurements.
- In the second zone, the mechanical parameter values are constants. It can then be assumed that those values are not affected by scale effects and are proper to the material.

The mean values of both hardness and elastic modulus obtained for the four samples can be seen in **table.5.4.** Due to a problem of calibration, it was not possible to obtain a constant value of the elastic modulus vs. the penetration depth, for this reason the values presented in **table.5.4** are the ones obtained for a penetration depth of 500 nm, depth value corresponding to the beginning of the second zone.

Table.5.4 *Mechanical parameters obtained for the four samples tested.*

Sample	D1	D2	D3	H
Hardness (GPa)	17.0 ± 0.4	15.7 ± 0.6	16.6 ± 0.9	16.5 ± 0.4
Elastic modulus (GPa)	272	252	265	276

The values of E range from 252 to 276 GPa for all the specimens analyzed, while the values of H range from 15.7 to 17.0 GPa. It cannot be observed a significant tendency of the mechanical parameters concerning the sample exposed to a higher RH comparing to the others. Those values correspond to the mechanical parameters of the material at nano-scale, and therefore the hardness values found are higher than the ones found with Vickers indentations.

In the **Fig.5.25** can be observed the loading part of the penetration depth curve for the sample D1. Because the data were not measured during the unloading part, it is not possible to calculate parameters from this curve. Nevertheless, it is possible to see that during the measurements (same curve tendency obtained for the three other samples) no events such as crack nucleation or dislocation movements took place. Indeed, if it had been the case, it could have been possible to observe a mismatch of the curve.

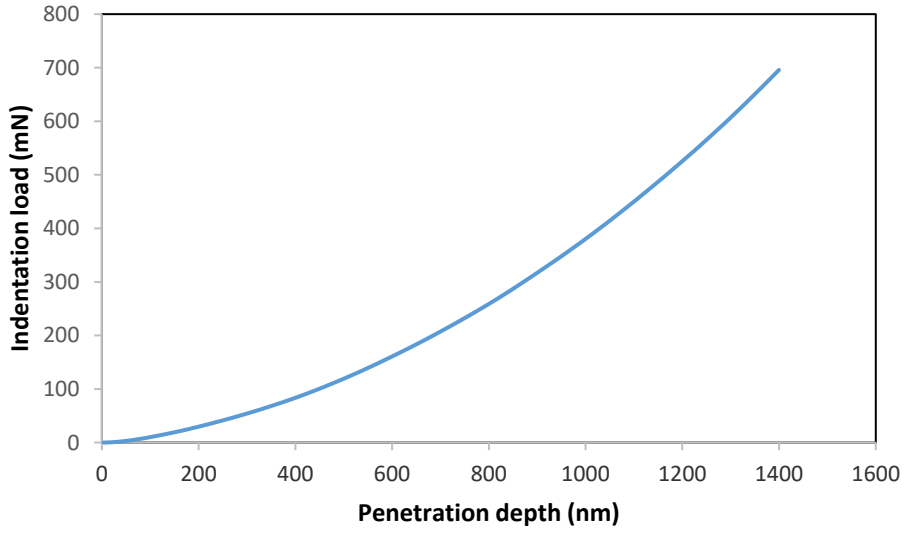

Fig.5.25 *Loading part of the penetration depth curve of the sample D1.*

6. Environmental impact analysis

During this Master's thesis, the environmental impact caused is related to the use of material for the sample preparation (Pluronic F-127®, 8Y-TZP powder and distilled water) and for the sample characterization (bakelite, sinolyte resin, MEKP, diamond and colloidal silica suspensions, grinding papers) as well as the energy consumed during the diverse processes such as T.T. or the use of machine to characterize the samples.

It can be said that the materials used during this Master's thesis do not have an elevated impact on the environment, since no acid, base or other aggressive substances were used.

During the sample preparation, in order to reduce the environmental impact, the materials were used in a way to avoid waste or leftover products during the sample manufacturing. Therefore, ceramic pastes were always prepared in small quantity (20g) and the materials reused as much as possible. In the same optic, the printing ustensils such as seringes, pistons, injection tips or paste containers were reused as much as possible and then recycled.

The processes that had the higher impacts were:

- the sintering treatments, were a high quantity of energy was consumed. A solution realized in order to reduce this impact was to put the maximum quantity of samples possible to sinther or to share the furnace with a collegue in the need to use the same thermal treatment.
- The polishing process also had a great environmental impact since it requires the use of a continuous flow of water for some steps of the process. Moreover, the grind paper used for the first steps of the process were also thrown away once used.

In comparaison, the impact caused by the electricity consumed for the characterization tests such as the use of the diverse microscopes, the Vickers and Berkovich indentations was much lower in term of energy consumption.

Thanks to the organization within the CIEFMA laboratory, it was easily possible to recylcle each of the materials used in order to reduce the final environmental impact.

Conclusions

With the work realized during this Master's thesis, it is possible to draw the following conclusions:

1) Regarding the printing parameters and paste composition:

- With the aim of obtaining a fully dense electrolyte with the use of 8Y-TZP powder and the hydrogel composed of 25 wt.% of Pluronic F-127® and 75 wt.% of distilled water, it was determined that the optimal composition of the printable paste was 67.5 wt.% of ceramic powder and 32.5 wt.% of hydrogel.
- With the same objective and regarding the particle and agglomerate size, it was proven that the nozzle showing the best results was a smoothless tapered tip with an injection diameter of 580 μm.
- The different tests realized on the humidity evolution inside the material have allowed the verification of the necessity for the printed samples to be placed in an atmosphere with a relative humidity inferior to 60% during a time of 5 days before proceeding to the sintering process. Otherwise, the porosity of the material will be higher due to a higher content in water inside the material when realizing the sintering process.
- The shrinkage that take place during the sintering process for the composition studied is of 57 ± 1.4 % in volume. Therefore, this phenomenon needs to be taken in consideration during the creation of the CAD model in order to obtain the desired final dimensions.
- It was demonstrated that the geometry does not affect significantly the value of the material density.
- It was not possible to print a sample with a tubular geometry with an intern diameter superior to 8 mm with the conditions used in this Master's thesis.

2) Regarding the microstructure of the material:

- The realization of FESEM observations on the diverse samples' superficies allowed to see a higher content of external porosity on the samples manufactured with robocasting than the reference manufactured with CIP. It was also possible to observe a higher number of defects on the printed sample which can be considered as inherent to the robocasting process. With the realization of a thermal attack at a temperature of 1200°C, it was possible to observe the grains of the material, and therefore, to calculate the average value of the grain area, equal to 3.07 μm^2.

- The realization of XRD on the different samples and the ceramic powder used to manufactured the paste demonstrated that both of the manufacturing process does not affect the phases composition of the material.

3) Regarding the mechanical properties of the material:

- The realization of Vickers indentation allowed the obtention of the fracture toughness and the hardness of the material for both geometries printed and for the reference sample. It was found for both mechanical parameters that the printed samples present higher values than the reference sample for indentation loads equal to 0.5 and 0.1 kgf, while for and indentation load of 10 kgf, the reference present higher mechanical parameter values. This could be due to the fact that the printed samples present a higher hardness and fracture toughness than the reference, but that the presence of defects in the material reduce these parameters at a larger scale. The results obtained during this Master's thesis are superior to those of the literature found in the internet, which can question the reliability of the results found.
- The Berkovich indentations realized on the printed samples allowed the obtention of the elastic modulus and the hardness parameters of the material at a nano-scale. It was possible to calculate the average values for both parameters, which are of 263 ± 10 GPa for the elastic modulus and 16.4 ± 0.7 $MPa.m^{-0.5}$.

The final conclusion of this Master's thesis is that it is possible to print yttria stabilized zirconia with the same density by additive manufacturing method than with conventional technique such as cold isostatic pressing. Nevertheless, the presence of defects and irregularities in the printed material as well as a higher content in external porosity can reduce the mechanical properties of the final part at larger scale. This last point has to be taken in consideration and could be an interesting aspect for further investigation within the CIEFMA group.

7. Budget and financial analysis

Table.7.1 *Costs of the consumables employed during this Master's thesis.*

Consumables

Product	Quantity	Cost/unit	Total cost [€]
Parafilm	0.03Kg	2€/Kg	0.06
Pluronic F-127®	0.10Kg	190€/Kg	19
8Y-TZP	0.62Kg	125€/Kg	77.5
Distilled water	2Kg	0.7€/Kg	1.4
Grinding paper P1200	6	0.8€/unit	4.8
Cloth MD-Dac	3	53€/unit	159
Cloth MD-Nap	1	75€/unit	75
Diamond suspension 30µm	0.1L	90€/L	9
Diamond suspension 6µm	0.2L	83€/L	16.6
Diamond suspension 3µm	0.3L	75€/L	22.5
Colloidal silica suspension	0.05L	150€/L	7.5
Acetone	0.1L	8€/L	0.8
Bakelyte flake	0.6Kg	100€/kg	60
UP resin	0.1L	11.16€/L	1.116
Paper	1Kg	5€/Kg	5
		Subtotal (€):	**459.816**

Table.7.2 *Costs of the equipment employed during this Master's thesis.*

Equipments

Equipment	Quantity	Cost/unit	Total cost (€)
Balance	10h	10.1€/h	101
SpeedMixer	3h	5€/h	15
3D-Printer	120h	12.4€/h	1488
Nabathern Furnace	196h	12.4€/h	2430.4
Polisher LaboPol-5	20h	12.4€/h	248
Confocal microscope	9h	13.45€/h	121.05
Nanoindenter	5h	60€/h	300
Vickers indenter	4h	12.4€/h	49.6
FESEM	4h	150€/h	600
XRD	3	22.44€/measure	67.32
		Subtotal (€):	**5420.37**

Table.7.3 *Costs of the support engineering needed during this Master's thesis.*

Costs of support engineering

Concept	Quantity (h)	Cost/unit (€/h)	Total cost (€)
Support technician	10	40	400
Supervisor	15	50	750
		Subtotal (€):	**1150**

Table.7.4 *Costs of engineering of this Master's thesis.*

Costs of engineering by the designer

Concept	Quantity (h)	Cost/unit (€/h)	Total cost (€)
Sample preparation	200	24.8	4960
Sample characterization	40	24.8	992
Search for information	150	24.8	3720
Analysis results	90	24.8	2232
Memory development	250	24.8	6200
		Subtotal (€):	**18104**

Table.7.5 *Total Master's thesis cost.*

Total cost of the project

Concept	Cost (€)
Consumables	459.816
Sample characterization	5420.37
Support engineering	1150
Engineering	18104
Total:	**25134.19**
IVA (21 %):	**5278.18**
Total + IVA:	**30412.37**

Bibliography

[1] Ree.es. (2019). [online] Available at: https://www.ree.es/sites/default/files/11_PUBLICACIONES/Documentos/InformesSistemaElectrico/2017/inf_sis_elec_ree_2017.pdf [Accessed 25 Jan. 2019].

[2] Eia.gov. (2018). *Short-Term Energy Outlook - U.S. Energy Information Administration (EIA)*. [online] Available at: https://www.eia.gov/outlooks/steo/marketreview/petproducts.php [Accessed 25 Nov. 2018].

[3] Bp.com. (2019). [online] Available at: https://www.bp.com/content/dam/bp/en/corporate/pdf/energy-economics/statistical-review/bp-stats-review-2018-full-report.pdf [Accessed 25 Jan. 2019].

[4] Merriam-webster.com. (2018). *Definition of FUEL CELL*. [online] Available at: https://www.merriam-webster.com/dictionary/fuel%20cell [Accessed 26 Sep. 2018].

[5] Les Imprimantes 3D .fr. (2018). *Scanner 3D | Les Imprimantes 3D .fr*. [online] Available at: https://www.lesimprimantes3d.fr/categorie/scanner-3d/ [Accessed 25 Nov. 2018].

[6] Printers, C., Us, C. and Printers, 3. (2018). *40 Affordable 3D Printers Under $500 USD - September 2018 - Buy 3D Printer*. [online] 3D Printing. Available at: https://3dprinting.com/3dprinters/40-affordable-3d-printers-on-sale-under-500-buy-now/ [Accessed 26 Sep. 2018].

[7] Ngo, T., Kashani, A., Imbalzano, G., Nguyen, K. and Hui, D. (2018). Additive manufacturing (3D printing): A review of materials, methods, applications and challenges. *Composites Part B: Engineering*, 143, pp.172-196.

[8] Staff, A. (2018). *Pros and Cons of Additive Manufacturing | Composites Manufacturing Magazine*. [online] Composites Manufacturing Magazine. Available at: http://compositesmanufacturingmagazine.com/2014/10/pros-cons-additive-manufacturing/ [Accessed 26 Sep. 2018].

[9] Prakash, K., Nancharaih, T. and Rao, V. (2018). *Additive Manufacturing Techniques in Manufacturing -An Overview*, pp.3873-3882.

[10] Imprimalia 3D. (2019). *Entrevista a Charles Hull, inventor de la impresión 3D - Impresoras 3D*. [online] Available at: http://imprimalia3d.com/noticias/2014/02/17/001322/entrevista-charles-hull-inventor-impresi-n-3d [Accessed 25 Jan. 2019].

[11] Nichols, M. (2018). *7 Additive Manufacturing Categories You Need to Know | Schooled By Science*. [online] Schooled By Science. Available at: https://schooledbyscience.com/7-additive-manufacturing-categories/ [Accessed 26 Sep. 2018].

[12] Penggagas. (2019). *Menelisik Misteri Dibalik 3D Printer (Stereolithography dan Photopolymer)*. [online] Available at: http://www.penggagas.com/menelisik-misteri-dibalik-3d-printer-stereolithography-dan-photopolymer/ [Accessed 22 Jan. 2019].

[13] Jerez-Mesa, R., Travieso-Rodriguez, J., Corbella, X., Busqué, R. and Gomez-Gras, G. (2016). Finite element analysis of the thermal behavior of a RepRap 3D printer liquefier. *Mechatronics*, 36, pp.119-126.

[14] Lu, R., Chandrasekaran, S., Du Frane, W., Landingham, R., Worsley, M. and Kuntz, J. (2018). Complex shaped boron carbides from negative additive manufacturing. *Materials & Design*, 148, pp.8-16.

[15] Sandia.gov. (2019). *Robocasting: New way to fabricate ceramics*. [online] Available at: https://www.sandia.gov/media/robocast.htm [Accessed 23 Jan. 2019].

[16] Panda, B., Paul, S., Hui, L., Tay, Y. and Tan, M. (2017). Additive manufacturing of geopolymer for sustainable built environment. *Journal of Cleaner Production*, 167, pp.281-288.

[17] Wohlers, T. and Caffrey, T. (2018). *Additive Manufacturing: The State of the Industry*. [online] Available at: https://www.sme.org/uploadedFiles/Publications/ME_Magazine/2016/May/May%202016%20f1%20Wholers.pdf [Accessed 24 Nov. 2018].

[18] Rees, M. (2018). *Une proposition de loi sur l'impression 3D et l'ordre public*. [online] Nextinpact.com. Available at: https://www.nextinpact.com/news/101921-une-proposition-loi-sur-l-impression-3d-et-l-ordre-public.htm [Accessed 4 Oct. 2018].

[19] Aniwaa. (2018). *Des pistolets imprimés en 3D au Ghost Gunner - armes et impressions 3D*. [online] Available at: https://www.aniwaa.fr/armes-a-feu-et-impression-3d/ [Accessed 4 Oct. 2018].

[20] Technology's Legal Edge. (2018). *Top 3 legal issues of 3D Printing! | Technology's Legal Edge*. [online] Available at: https://www.technologyslegaledge.com/2015/09/top-3-legal-issues-of-3d-printing/ [Accessed 4 Oct. 2018].

[21] Kouichi, T. (2008). Electrochemistry of fuel cell. *Energy Carriers and Concersion Systems, Encyclopedia of Life Support Systems (EOLSS)*, vol II, pp.107-111.

[22] Energy.gov. (2018). *Types of Fuel Cells | Department of Energy*. [online] Available at: https://www.energy.gov/eere/fuelcells/types-fuel-cells [Accessed 26 Sep. 2018].

[23] Energy.gov. (2018). *Comparison of Fuel Cell Technologies | Department of Energy*. [online] Available at: https://www.energy.gov/eere/fuelcells/comparison-fuel-cell-technologies [Accessed 26 Sep. 2018].

[24] Fleig, J. (2003). Solid Oxide Fuel Cell Cathodes: Polarization Mechanisms and Modeling of the Electrochemical Performance. *Annual Review of Materials Research*, 33(1), pp.361-382.

[25] WANG, J., LIU, M. and LIN, M. (2006). Oxygen reduction reactions in the SOFC cathode of Ag/CeO2. *Solid State Ionics*, 177(9-10), pp.939-947.

[26] Sandia Energy. (2019). *Maritime Hydrogen Fuel Cell Generator Project*. [online] Available at: https://energy.sandia.gov/transportation-energy/hydrogen/market-transformation/maritime-fuel-cells/maritime-hydrogen-fuel-cell-project/ [Accessed 25 Jan. 2019].

[27] Alstom. (2018). *World premiere: Alstom's hydrogen trains enter passenger service in Lower Saxony*. [online] Available at: https://www.alstom.com/press-releases-news/2018/9/world-premiere-alstoms-hydrogen-trains-enter-passenger-service-lower [Accessed 24 Nov. 2018].

[28] Energy.gov. (2018). *Early Market Applications for Fuel Cell Technologies | Department of Energy*. [online] Available at: https://www.energy.gov/eere/fuelcells/early-market-applications-fuel-cell-technologies [Accessed 24 Nov. 2018].

[29] Fuelcelltoday.com. (2018). *FCT - Fuel Cell Applications - Portable*. [online] Available at: http://www.fuelcelltoday.com/applications/portable [Accessed 24 Nov. 2018].

[30] Spiegel, D. (2018). *Introduction to Fuel Cell Applications*. [online] Fuelcellstore.com. Available at: https://www.fuelcellstore.com/blog-section/intro-fuel-cell-applications [Accessed 24 Nov. 2018].

[31] DeviantArt. (2019). *Auxiliary Power Unit*. [online] Available at: https://www.deviantart.com/jakopaqtorius/art/Auxiliary-Power-Unit-473502314 [Accessed 22 Jan. 2019].

[32] Rainone, M. (2019). *Alstom Coradia iLint è il primo treno a idrogeno per trasporto passeggeri*. [online] Gadgetblog.it. Available at: http://www.gadgetblog.it/post/184180/alstom-coradia-ilint-e-il-primo-treno-a-idrogeno-per-trasporto-passeggeri [Accessed 22 Jan. 2019].

[33] Haile, S. (2003). Fuel cell materials and components☆☆☆The Golden Jubilee Issue—Selected topics in Materials Science and Engineering: Past, Present and Future, edited by S. Suresh. *Acta Materialia*, 51(19), pp.5981-6000.

[34] Ellen Ivers-Tiffée, André Weber, Dirk Herbstritt (2001). Materials and technologies for SOFC-components. *Journal of the European Society*, 21, pp.1805-1811.

[35] Esposito, V., Gadea, C., Hjelm, J., Marani, D., Hu, Q., Agersted, K., Ramousse, S. and Jensen, S. (2018). *Fabrication of thin yttria-stabilized-zirconia dense electrolyte layers by inkjet printing for high performing solid oxide fuel cells*.

[36] Ideal-cell.eu. (2019). [online] Available at: http://www.ideal-cell.eu/files/AISOFCsTCs/AISOFC_TC_5_Piccardo_Amendola.pdf [Accessed 25 Jan. 2019].

[37] Energy.gov. (2018). *Fuel Cell Systems | Department of Energy*. [online] Available at: https://www.energy.gov/eere/fuelcells/fuel-cell-systems [Accessed 25 Nov. 2018].

[38] Elringklinger.de. (2019). *Complete fuel cell stacks | ElringKlinger AG*. [online] Available at: https://www.elringklinger.de/en/press/press-photos/complete-fuel-cell-stacks-economical-environmentally-friendly-energy-supply-are-developed-and [Accessed 22 Jan. 2019].

[39] Omicsonline.org. (2019). *Sunghwan Lee | Energy Materials 2017 | OMICS International*. [online] Available at: https://www.omicsonline.org/abstract/intermediate-temperature-synthesis-and-sofc-anode-application-of-cerium-silicatebased-oxy-apatites/ [Accessed 25 Jan. 2019].

[40] Wells, A. (1984). *Structural inorganic chemistry*. Oxford: Clarendon Pr, pp.885-895.

[41] Glisenti, A. (2018). *Electrolytes: Stabilized bismuthsesquioxide*. [online] Chimica.unipd.it. Available at: http://www.chimica.unipd.it/antonella.glisenti/privata/documentazione/insegnamenti/Fuel%20Cells/Bi2O3.pdf [Accessed 24 Nov. 2018].

[42] Wenk, H. and Bulakh, A. (2003). *Minerals*. Cambridge: Cambridge University Press.

[43] Kittel, *Introduction to Solid State Physics*, 8th edition, pp. 194–196.

[44] Urushibara, A., Moritomo, Y., Arima, T., Asamitsu, A., Kido, G. and Tokura, Y. (1995). Insulator-metal transition and giant magnetoresistance inLa1−xSrxMnO3. *Physical Review B*, 51(20), pp.14103-14109.

[45] BEBELIS, S., NEOPHYTIDES, S., KOTSIONOPOULOS, N., TRIANTAFYLLOPOULOS, N., COLOMER, M. and JURADO, J. (2006). Methane oxidation on composite ruthenium electrodes in YSZ cells. *Solid State Ionics*, 177(19-25), pp.2087-2091.

[46] David, E., Alman and Paul, D. J. (2004). Low coefficient of thermal expansion (CTE) nickel base superallows for interconnect applications in intermediate temperature solid oxide fuel cells (SOFC). *TMS (The Minerals, Metals & Materials Society),* pp117-122

[47] Pinterest. (2019). *Bravais Crystal Lattices: Rhombohedral or Trigonal Bravais Crystal Lattice.The rhombohedral (or trigonal) crystal is described by… | c.h.e.m.i.s.t.r.y. | Pinterest | Equality, Photo credit and Crystals*. [online] Available at: https://www.pinterest.co.uk/pin/348466089901052713/ [Accessed 22 Jan. 2019].

[48] Commons.wikimedia.org. (2019). *File:Face-centered cubic.svg - Wikimedia Commons*. [online] Available at: https://commons.wikimedia.org/wiki/File:Face-centered_cubic.svg [Accessed 22 Jan. 2019].

[49] Geologycafe.com. (2019). *Geology Cafe.com*. [online] Available at: http://www.geologycafe.com/class/chapter3.html [Accessed 22 Jan. 2019].

[50] Pixshark.com. (2019). *Perovskite Structure Abo3 | www.pixshark.com - Images Galleries With A Bite!*. [online] Available at: https://pixshark.com/perovskite-structure-abo3.htm [Accessed 22 Jan. 2019].

[51] MINH, N. (2004). Solid oxide fuel cell technology?features and applications. *Solid State Ionics*, 174(1-4), pp.271-277.

[52] MINH, N. (2004). Solid oxide fuel cell technology-features and applications. *Solid State Ionics*, 174(1-4), pp.271-277.

[53] Cláudia Ângela Maziero Volpato, Federica Bondioli, Luis Gustavo D.́ Altoé Garbelotto and Márcio Celso Fredel (2011). *Application of Zirconia in Dentistry: Biological, Mechanical and Optical Considerations*. INTECH Open Access Publisher.

[54] Mahmoud, M. (2018). *Zirconia overview*. [online] Slideshare.net. Available at: https://www.slideshare.net/MohamedMahmoud443/zirconia-overview [Accessed 27 Sep. 2018].

[55] Anon, (2019). [online] Available at: https://www.researchgate.net/post/What_are_Densities_of_Monoclinic_Tetragonal_and_Cubic_Zirconia?fbclid=IwAR0_UbGd9DylMYbJT-ZxA1dER-bFD92ugu25qU0sBKjLqCIs8B2Q6Wrbzj0 [Accessed 23 Jan. 2019].

[56] Cousland, G., Cui, X., Smith, A., Stampfl, A. and Stampfl, C. (2018). Mechanical properties of zirconia, doped and undoped yttria-stabilized cubic zirconia from first-principles. *Journal of Physics and Chemistry of Solids*, 122, pp.51-71.

[57] Ceramics, P. (2018). *Zirconia – Properties and Applications by Precision Ceramics*. [online] AZoM.com. Available at: https://www.azom.com/article.aspx?ArticleID=11082 [Accessed 26 Sep. 2018].

[58] Barthlab.com. (2019). *Bruxzir Crowns - Zirconia Crowns- Cercon Zirconium Crowns at Barth Dental Lab* |. [online] Available at: http://www.barthlab.com/dental-lab-products/bruxzir-zirconia-crowns/ [Accessed 22 Jan. 2019].

[59] Bladestech.com. (2019). *what's ceramic cutting blades?where's zirconia ZrO2 slitting knives manufacturer?how to buy ceramic ZrO2 razor inserts, zirconium oxide(ZrO2) blades?*. [online] Available at: https://bladestech.com/32ceramic-ZrO2-cutting-blades.htm [Accessed 22 Jan. 2019].

[60] Hamid Akash, M., Rehman, K. and Chen, S. (2015). Natural and Synthetic Polymers as Drug Carriers for Delivery of Therapeutic Proteins. *Polymer Reviews*, 55(3), pp.371-406.

[61] Geng, H., Song, H., Qi, J. and Cui, D. (2011). Sustained release of VEGF from PLGA nanoparticles embedded thermo-sensitive hydrogel in full-thickness porcine bladder acellular matrix. *Nanoscale Research Letters*, 6(1), p.312.

[62] Osorio, J., Lopera-Valle, A., Toro, A. and Hernández-Ortiz, J. (2018). *Phase transformations in air plasma-sprayed yttria-stabilized zirconia thermal barrier coatings*.

[63] Stawarczyk, B., Özcan, M., Hallmann, L., Ender, A., Mehl, A. and Hämmerlet, C. (2012). The effect of zirconia sintering temperature on flexural strength, grain size, and contrast ratio. *Clinical Oral Investigations*, 17(1), pp.269-274.

[64] Cook, P. and Slessor, C. (1998). *An illustrated guide to bakelite collectables*. London: Quantum pp.2-10.

[65] Mbfg.co.uk. (2018). [online] Available at: http://www.mbfg.co.uk/user/datasheets/synolite_0328_msds.pdf [Accessed 25 Dec. 2018].

[66] Pubchem.ncbi.nlm.nih.gov. (2019). *2-Butanone peroxide*. [online] Available at: https://pubchem.ncbi.nlm.nih.gov/compound/Methyl_ethyl_ketone_peroxide#section=Top [Accessed 25 Jan. 2019].

[67] Encyclopedia Britannica. (2019). *Archimedes' principle | Description & Facts*. [online] Available at: https://www.britannica.com/science/Archimedes-principle [Accessed 25 Jan. 2019].

[68] Thermexcel.com. (2019). *Masse volumique de l'air, densit*, *kg/m3, air, temperature, humidite relative, massique*. [online] Available at: https://www.thermexcel.com/french/tables/massair.htm [Accessed 13 Jan. 2019].

[69] Olympus-ims.com. (2019). *Optical Microscopes | Olympus IMS*. [online] Available at: https://www.olympus-ims.com/en/microscope/terms/feature10/ [Accessed 25 Jan. 2019].

[70] Olympus-ims.com. (2018). *BX53M - Upright Metallurgical Microscopes*. [online] Available at: https://www.olympus-ims.com/en/microscope/bx53m/#!cms[tab]=%2Fmicroscope%2Fbx53m%2Ffeatures [Accessed 26 Sep. 2018].

[71] Olympus-lifescience.com. (2019). *Confocal Microscopy - Introduction*. [online] Available at: https://www.olympus-lifescience.com/en/microscope-resource/primer/techniques/confocal/confocalintro/ [Accessed 25 Jan. 2019].

[72] Chatterjee, A. (2001). X-Ray Diffraction. *Handbook of Analytical Techniques in Concrete Science and Technology*, pp.275-332.

[73] Techniques. (2019). *Scanning Electron Microscopy (SEM)*. [online] Available at: https://serc.carleton.edu/research_education/geochemsheets/techniques/SEM.html [Accessed 25 Jan. 2019].

[74] En.wikipedia.org. (2018). *Scanning electron microscope*. [online] Available at: https://en.wikipedia.org/wiki/Scanning_electron_microscope [Accessed 26 Sep. 2018].

[75] En.wikipedia.org. (2018). *Vickers hardness test*. [online] Available at: https://en.wikipedia.org/wiki/Vickers_hardness_test [Accessed 30 Nov. 2018].

[76] D. Quinn, G. (2006). *National institute of standards and technology* [online] Ws680.nist.gov. Available at: https://ws680.nist.gov/publication/get_pdf.cfm?pub_id=854209 [Accessed 30 Nov. 2018].

[77] Baker, S. and Liu, J. (2016). Nanoindentation Techniques. *Reference Module in Materials Science and Materials Engineering*.

[78] Zong, W., Wu, D. and He, C. (2017). Radius and angle determination of diamond Berkovich indenter. *Measurement*, 104, pp.243-252.

[79] Tsai, C., Jian, S. and Juang, J. (2008). Berkovich nanoindentation and deformation mechanisms in GaN thin films. *Applied Surface Science*, 254(7), pp.1997-2002.

[80] Npl.co.uk. (2019). *Instrumented Indentation : Hardness methods and sensitivity coefficients : Mass & Force : Science + Technology : National Physical Laboratory*. [online] Available at: http://www.npl.co.uk/science-technology/mass-and-force/hardness/instrumented-indentation [Accessed 23 Jan. 2019].

[81] Nakano, K., Yoshizaki, H., Saitoh, Y., Ishikawa, N. and Iwase, A. (2019). *XRD study of yttria stabilized zirconia irradiated with 7.3MeV Fe, 10MeV I, 16MeV Au, 200MeV Xe and 2.2GeV Au ions*.

[82] Maridurai, T., Balaji, D. and Sagadevan, S. (2016). Synthesis and Characterization of Yttrium Stabilized Zirconia Nanoparticles. *Materials Research*, 19(4), pp.812-816.

[83] Abden, M. J., Islam, M. K. and Afroze, J. D. (2014). Microstructure and Mechanical Properties of 3YSZ Ceramics Reinforced with Al2O3 Particles, *International Journal of Materials Engineering*, 4(4): 129-135.

[84] Roy, C. and David, G. (1970). X-ray diffraction analyses of zirconia films on zirconium and zircaloy-2. *Journal of Nuclear Materials*, 37(1), pp.71-81.

[85] Srinivasan, R., De Angelis, R., Ice, G. and Davis, B. (1991). Identification of tetragonal and cubic structures of zirconia using synchrotron x-radiation source. *Journal of Materials Research*, 6(06), pp.1287-1292.

[86] Liu, H., Zhao, W., Ji, Y., Cui, J., Chu, Y. and Rao, P. (2019). *Determination of fracture toughness of zirconia ceramics with different yttria concentrations by SEVNB method*.

[87] Vasylkiv, O., Sakka, Y. and Skorokhod, V. (2003). Hardness and Fracture Toughness of Alumina-Doped Tetragonal Zirconia with Different Yttria Contents. *MATERIALS TRANSACTIONS*, 44(10), pp.2235-2238.

[88] Lin, J. and Duh, J. (2003). Fracture toughness and hardness of ceria- and yttria-doped tetragonal zirconia ceramics. *Materials Chemistry and Physics*, 78(1), pp.253-261.

[89] Hiraga, K., Morita, K., Kim, B. and Sakka, Y. (2005). Fracture Toughness of Yttria-Stabilized Cubic Zirconia (8Y-CSZ) Doped with Pure Silica. *Journal of the Japan Institute of Metals*, 69(10), pp.928-932.

Appendix

Annex A: Data sheets

Annex A.1 *Pluronic F-127®.*

SIGMA-ALDRICH®

sigma-aldrich.com

3050 Spruce Street, Saint Louis, MO 63103, USA
Website: www.sigmaaldrich.com
Email USA: techserv@sial.com
Outside USA: eurtechserv@sial.com

Product Specification

Product Name:
Pluronic® F-127 – powder, BioReagent, suitable for cell culture

Product Number: **P2443**
CAS Number: 9003-11-6
MDL: MFCD00082049

TEST	Specification
Appearance (Color)	White
Appearance (Form)	Powder
Solubility (Color)	Colorless
Solubility (Turbidity) 50 mg/mL, H2O, at less than 10 deg C	Clear
pH (2.5% solution)	6.0 - 7.0
Moisture Content	≤ 0.75 %
Cell Culture Test	Pass
Recommended Retest Period 2 Years	----------
Note Pluronic is a registered trademark of BASF SE.	----------

Specification: PRD.1.ZQ5.10000051983

Annex A.2 *Certificate of analysis of 8Y-TZP.*

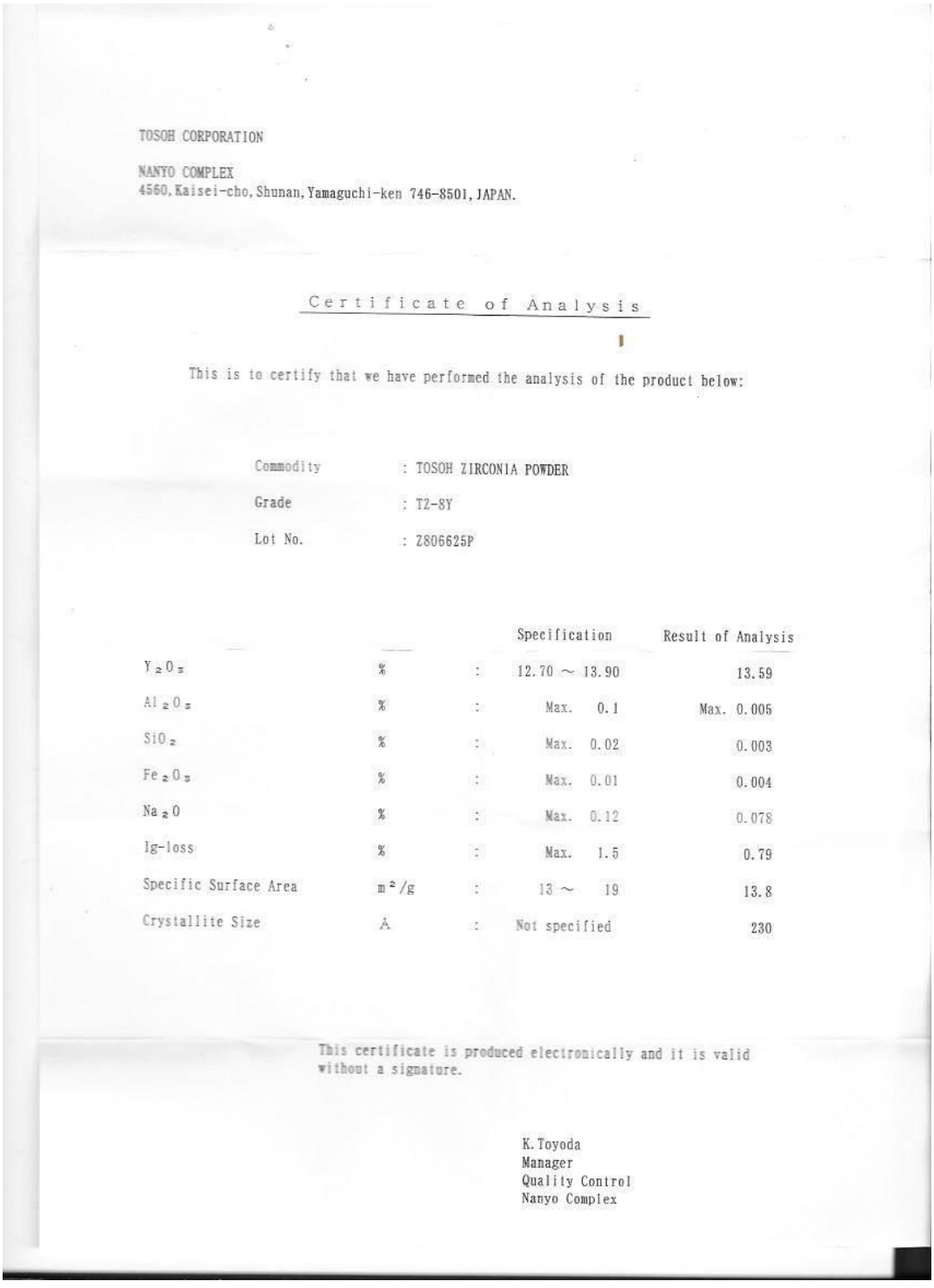

TOSOH CORPORATION

NANYO COMPLEX
4560, Kaisei-cho, Shunan, Yamaguchi-ken 746-8501, JAPAN.

Certificate of Analysis

This is to certify that we have performed the analysis of the product below:

Commodity : TOSOH ZIRCONIA POWDER
Grade : TZ-8Y
Lot No. : Z806625P

			Specification	Result of Analysis
Y_2O_3	%	:	12.70 ~ 13.90	13.59
Al_2O_3	%	:	Max. 0.1	Max. 0.005
SiO_2	%	:	Max. 0.02	0.003
Fe_2O_3	%	:	Max. 0.01	0.004
Na_2O	%	:	Max. 0.12	0.078
Ig-loss	%	:	Max. 1.5	0.79
Specific Surface Area	m^2/g	:	13 ~ 19	13.8
Crystallite Size	Å	:	Not specified	230

This certificate is produced electronically and it is valid without a signature.

K. Toyoda
Manager
Quality Control
Nanyo Complex

Annex B: Code python

Annex B.1 *Python code for the heatmap layout.*

```
# -*- coding: cp1252 -*-
import plotly.plotly as py
import plotly.graph_objs as go
# pauloxc54
# UTyM9HBwOlCih1mvhY4A
import pandas as pd
#import numpy as np
import xlrd
import numpy as np
import plotly


plotly.tools.set_credentials_file(username='          ', api_key='                          ')

z = np.zeros((47,32)) #matrix 10 to 60 degrees for 0 to 100 wt% of 8Y-TZP
#print(z)
wb = xlrd.open_workbook('fichier.xls') #ou fichier
sh = wb.sheet_by_name(u'Sheet1')
i=0
xp = z[0,1:31] #check
yp = z[1:46,0]
for rownum in range(sh.nrows):
    z[0:46,i]=sh.row_values(rownum) #value start at 22°C and end at 40°C
    #print(z[21:42,i+19])
    i+=1
    print(i)

for i in range(32):
    for j in range(47):
        if z[j,i]==0:
            z[j,i]=None

data = [
    go.Contour(
        z=z[1:46,1:30],
        x=xp,
        y=yp,
        showlegend=True,
    )]

layout = go.Layout(
    title = 'graphique ',
    scene = dict(
        xaxis=dict(
            title='T(°C)',
            titlefont=dict(
                family='Arial, sans-serif',
                size=18,
                #color='lightgrey',
                ),
        ),
        yaxis=dict(
            title='wt% 8Y-TZP',
            titlefont=dict(
                family='Arial, sans-serif',
                size=18,
                #color='lightgrey',
                ),
        ),
    ))
fig = go.Figure(data=data, layout=layout)
plotly.offline.plot(fig)
```

Annex B.2 *Python code for the 3D-grafic layout*

```
# -*- coding: cp1252 -*-
import plotly.plotly as py
import plotly.graph_objs as go
# pauloxc54
# UTyM9HBwOlCih1mvhY4A
import pandas as pd
#import numpy as np
import xlrd
import numpy as np
import plotly

plotly.tools.set_credentials_file(username='          ', api_key='                    ')

z = np.zeros((47,32)) #matrix 10 to 60 degrees for 0 to 100 wt% of 8Y-TZP
#print(z)
wb = xlrd.open_workbook('fichier.xls') #ou fichier
sh = wb.sheet_by_name(u'Sheet1')
i=0
xp = z[0,1:31] #check
yp = z[1:46,0]
for rownum in range(sh.nrows):
    z[0:46,i]=sh.row_values(rownum) #value start at 22°C and end at 40°C
    #print(z[21:42,i+19])
    i+=1
    print(i)

for i in range(32):
    for j in range(47):
        if z[j,i]==0:
            z[j,i]=None
data = [
    go.Surface(
        z=z[1:46,1:30],
        x=xp,
        y=yp,
        showlegend=True,
        #opacity=0.9,
    )
]
layout = go.Layout(
    title = 'graphique 3D',
    scene = dict(
        xaxis=dict(
            title='T(°C)',
            titlefont=dict(
                family='Arial, sans-serif',
                size=18,
                #color='lightgrey',
                ),
            backgroundcolor="rgb(200, 200, 230)",#violet
            gridcolor="rgb(255, 255, 255)",
            showbackground=True,
            zerolinecolor="rgb(255, 255, 255)",
        ),
        yaxis=dict(
            title='wt% 8Y-TZP',
            titlefont=dict(
                family='Arial, sans-serif',
                size=18,
                #color='lightgrey',
                ),
            backgroundcolor="rgb(230, 200,230)",#rose pd
            gridcolor="rgb(255, 255, 255)",
            showbackground=True,
            zerolinecolor="rgb(255, 255, 255)"
        ),
        zaxis=dict(
             title='density',
             titlefont=dict(
                family='Arial, sans-serif',
                size=18,
                #color='lightgrey',
                ),
             backgroundcolor='lightgrey',
             gridcolor="rgb(255, 255, 255)",
             showbackground=True,
             zerolinecolor="rgb(255, 255, 255)",
        )
    )
)
fig = go.Figure(data=data, layout=layout)
#plotly.offline.plot(fig, filename='ribbon-plot-python.html')
py.plot(fig, filename='elevations-3d-surface')
```

Annex C: Data

Annex C.1 *Values of the water density regarding the temperature*

T en °C	p en kg/m^3	T en °C	p en kg/m^3
0	999.79	51	987.55
1	999.84	52	987.06
2	999.88	53	986.58
3	999.92	54	986.19
4	999.97	55	985.70
5	999.92	56	985.22
6	999.88	57	984.73
7	999.84	58	984.67
8	999.79	59	983.18
9	999.72	60	983.13
10	999.65	61	982.70
11	999.55	62	982.22
12	999.44	63	981.64
13	999.32	64	981.06
14	999.19	65	980.48
15	999.05	66	979.91
16	998.90	67	979.33
17	998.74	68	978.85
18	998.56	69	978.28
19	998.36	70	977.70
20	998.16	71	977.13
21	997.96	72	976.56
22	997.74	73	975.99
23	997.50	74	975.41
24	997.25	75	974.84
25	996.99	76	974.27
26	996.74	77	973.70
27	996.48	78	973.14
28	996.20	79	972.47
29	995.90	80	971.81
30	995.59	81	971.25
31	995.29	82	970.59
32	995.97	83	969.93
33	994.65	84	969.27
34	994.33	85	968.61
35	994.98	86	967.96
36	993.64	87	967.30
37	993.28	88	966.65
38	992.93	89	965.99
39	992.55	90	965.34
40	992.17	91	964.69
41	991.78	92	964.04
42	991.39	93	963.39
43	990.99	94	962.64
44	990.57	95	961.90
45	990.16	96	961.26
46	989.75	97	960.52
47	989.33	98	959.78
48	988.90	99	959.04
49	988.45	100	958.40
50	988.04	101	957.67

Annex C.2 *Values of the air density regarding the temperature and the relative humidity*

Ts	100% Hr	90% Hr	80% Hr	70% Hr	60% Hr	50% Hr	40% Hr	30% Hr	20% Hr	10% Hr	1% Hr
-10 °C	1,340	1,340	1,340	1,340	1,341	1,341	1,341	1,341	1,341	1,341	1,341
-9 °C	1,335	1,335	1,335	1,335	1,335	1,336	1,336	1,336	1,336	1,336	1,336
-8 °C	1,330	1,330	1,330	1,330	1,330	1,330	1,331	1,331	1,331	1,331	1,331
-7 °C	1,324	1,325	1,325	1,325	1,325	1,325	1,326	1,326	1,326	1,326	1,326
-6 °C	1,319	1,320	1,320	1,320	1,320	1,320	1,321	1,321	1,321	1,321	1,321
-5 °C	1,314	1,314	1,315	1,315	1,315	1,315	1,316	1,316	1,316	1,316	1,316
-4 °C	1,309	1,309	1,310	1,310	1,310	1,310	1,311	1,311	1,311	1,311	1,311
-3 °C	1,304	1,304	1,305	1,305	1,305	1,305	1,306	1,306	1,306	1,306	1,307
-2 °C	1,299	1,299	1,300	1,300	1,300	1,301	1,301	1,301	1,301	1,302	1,302
-1 °C	1,294	1,295	1,295	1,295	1,295	1,296	1,296	1,296	1,296	1,297	1,297
0 °C	1,289	1,290	1,290	1,290	1,290	1,291	1,291	1,291	1,292	1,292	1,292
1 °C	1,284	1,285	1,285	1,285	1,286	1,286	1,286	1,287	1,287	1,287	1,288
2 °C	1,279	1,280	1,280	1,281	1,281	1,281	1,282	1,282	1,282	1,283	1,283
3 °C	1,275	1,275	1,275	1,276	1,276	1,276	1,277	1,277	1,277	1,278	1,278
4 °C	1,270	1,270	1,271	1,271	1,271	1,272	1,272	1,272	1,273	1,273	1,274
5 °C	1,265	1,265	1,266	1,266	1,267	1,267	1,267	1,268	1,268	1,269	1,269
6 °C	1,260	1,261	1,261	1,261	1,262	1,262	1,263	1,263	1,264	1,264	1,264
7 °C	1,255	1,256	1,256	1,257	1,257	1,258	1,258	1,259	1,259	1,260	1,260
8 °C	1,250	1,251	1,251	1,252	1,252	1,253	1,253	1,254	1,254	1,255	1,255
9 °C	1,246	1,246	1,247	1,247	1,248	1,248	1,249	1,249	1,250	1,251	1,251
10 °C	1,241	1,241	1,242	1,243	1,243	1,244	1,244	1,245	1,245	1,246	1,247
11 °C	1,236	1,237	1,237	1,238	1,239	1,239	1,240	1,240	1,241	1,242	1,242
12 °C	1,231	1,232	1,233	1,233	1,234	1,235	1,235	1,236	1,237	1,237	1,238
13 °C	1,227	1,227	1,228	1,229	1,229	1,230	1,231	1,231	1,232	1,233	1,234
14 °C	1,222	1,223	1,223	1,224	1,225	1,226	1,226	1,227	1,228	1,229	1,229
15 °C	1,217	1,218	1,219	1,220	1,220	1,221	1,222	1,223	1,223	1,224	1,225
16 °C	1,212	1,213	1,214	1,215	1,216	1,217	1,217	1,218	1,219	1,220	1,221
17 °C	1,208	1,209	1,210	1,210	1,211	1,212	1,213	1,214	1,215	1,216	1,217
18 °C	1,203	1,204	1,205	1,206	1,207	1,208	1,209	1,210	1,211	1,211	1,212
19 °C	1,198	1,199	1,200	1,201	1,202	1,203	1,204	1,205	1,206	1,207	1,208
20 °C	1,194	1,195	1,196	1,197	1,198	1,199	1,200	1,201	1,202	1,203	1,204
21 °C	1,189	1,190	1,191	1,192	1,193	1,194	1,196	1,197	1,198	1,199	1,200
22 °C	1,184	1,185	1,187	1,188	1,189	1,190	1,191	1,192	1,194	1,195	1,196
23 °C	1,179	1,181	1,182	1,183	1,184	1,186	1,187	1,188	1,189	1,191	1,192
24 °C	1,175	1,176	1,177	1,179	1,180	1,181	1,183	1,184	1,185	1,187	1,188
25 °C	1,170	1,171	1,173	1,174	1,176	1,177	1,178	1,180	1,181	1,183	1,184
26 °C	1,165	1,167	1,168	1,170	1,171	1,173	1,174	1,176	1,177	1,178	1,180
27 °C	1,160	1,162	1,164	1,165	1,167	1,168	1,170	1,171	1,173	1,174	1,176

Annex C.3 *Different existing nozzles for robocasting method.*

PRECISION STAINLESS STEEL TIPS

Gauge	Color	ID mm	ID inch	OD mm	OD inch	6.35 mm (0.25")	12.7 mm (0.50")	25.4 mm (1.0")	38.1 mm (1.5")	45°/12.7 mm (0.5")	90°/12.7 mm (0.5")	45°/38.1 mm (1.5")	QTY
14	Olive	1.54	0.060	1.83	0.072	7018029	7018043	7018032	7018035	7018044	7018045	7016906	50
15	Amber	1.36	0.053	1.65	0.065	7018056	7018068	7018059	7018062	7018069	7018070	n/a	50
18	Green	0.84	0.033	1.27	0.050	7018107	7018122	7018110	7018113	7018123	7018124	7016908	50
20	Pink	0.61	0.024	0.91	0.036	7018163	7018178	7018166	7018169	7018179	7018180	n/a	50
21	Purple	0.51	0.020	0.82	0.032	7005005	7018233	7018222	7018225	7018234	7018235	7016910	50
22	Blue	0.41	0.016	0.72	0.028	7018260	7018272	7018263	7018266	7018273	7018274	n/a	50
23	Orange	0.33	0.013	0.65	0.025	7018302	7018314	7018305	7018308	7018315	7018316	n/a	50
25	Red	0.25	0.010	0.52	0.020	7018333	7018345	7018336	7018339	7018346	7018347	n/a	50
27	Clear	0.20	0.008	0.42	0.016	7018395	7005008	n/a	n/a	7018404	7018405	n/a	50
30	Lavender	0.15	0.006	0.31	0.012	7018424	7018433	n/a	n/a	7018434	7018435	n/a	50
32	Yellow	0.10	0.004	0.24	0.009	7018462	n/a	n/a	n/a	n/a	n/a	n/a	50

Burr-free, polished, passivated stainless steel dispense tips with polypropylene SafetyLok™ hubs for a secure fit to barrel reservoirs.

SMOOTHFLOW TAPERED TIPS

Gauge	Color	ID mm	ID inch	Standard	Opaque Rigid	QTY
14	Olive	1.60	0.063	7018052	7018049	50
16	Grey	1.19	0.047	7018100	7018097	50
18	Green	0.84	0.033	7018158	7018147	50
20	Pink	0.58	0.023	7005009	7005006	50
22	Blue	0.41	0.016	7018298	7005007	50
25	Red	0.25	0.010	7018391	7018370	50
27	Clear	0.20	0.008	7018417	n/a	50

Use with gel cyanoacrylates, UV-cure adhesives, sealants, and particle-filled materials or any medium to high viscosity fluid. Standard tips are molded of polyethylene with UV-light block additive. Rigid, opaque tapered tips are molded of polypropylene and the opacity delivers light-blocking functionality.

CHAMFERED TIPS

Gauge	Color	mm	ID inch	38.1 mm (1.50")	12.7 mm (0.50")	6.35 mm (0.25")	QTY
18	Green	0.84	0.033	n/a	7018129	n/a	50
20	Pink	0.61	0.024	7018188	n/a	n/a	50
22	Blue	0.41	0.016	7018281	n/a	n/a	50
23	Orange	0.33	0.013	n/a	7018321	n/a	50
25	Red	0.25	0.010	n/a	7018352	n/a	50
27	Clear	0.20	0.008	n/a	n/a	7015236	50
33	Clear	0.10	0.004	n/a	n/a	7018482	25
33	Black	0.10	0.004	n/a	n/a	7018477	25

Use for microdot application of low viscosity fluids.

PTFE-COATED TIPS

Gauge	Color	ID mm	ID inch	OD mm	OD inch	12.7 mm (0.50")	QTY
21	Purple	0.51	0.020	0.84	0.033	7018243	20
22	Blue	0.41	0.016	0.74	0.029	7018290	20
23	Orange	0.33	0.013	0.66	0.026	7018326	20
25	Red	0.25	0.010	0.53	0.021	7018359	20

Controls wicking to stop drips for optical media applications.

PTFE-LINED TIPS

Color	mm	ID inch	12.7 mm (0.50")	25.4 mm (1.0")	QTY
Grey	0.51	0.020	7018256	7005003	50
Pink	0.30	0.012	7018388	7005004	50

Resists clogging of cyanoacrylates. Use for microdot application of low viscosity fluids.

FLEXIBLE TIPS

Gauge	Color	ID mm	ID inch	12.7 mm (0.50")	38.1 mm (1.5")	QTY
15	Amber	1.36	0.053	7018085	7018080	50
18	Green	0.84	0.033	7018143	7018138	50
20	Pink	0.61	0.024	7018205	7018201	50
25	Red	0.25	0.010	7018366	7018362	50

Flexible polypropylene tubing for application into difficult-to-access areas. Easily drags along edges and around corners and prevents scratching. Tubing can be cut to length.

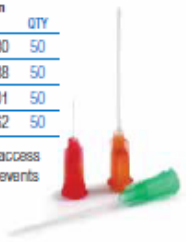

OVAL TIPS

Gauge	Color	12.7 mm (0.50")	QTY
15	Amber	7018078	50
18	Green	7024653	50
23	Orange	7024656	50

Flat ribbon deposits of thick pastes, sealants, and epoxies.